공학박사학위논문

Compact Wide-Area RTK

: A Study on Carrier Phase Based Correction Generation Algorithms for Centimeter-Level Satellite Augmentation System

센티미터 급 광역 보강항법 시스템의 반송파 위상 기반 보정정보 생성 알고리즘에 관한 연구

2020 년 2 월

서울대학교 대학원

기계항공공학부

김 동 욱

Compact Wide-Area RTK
: A Study on Carrier Phase Based Correction Generation Algorithms for Centimeter-Level Satellite Augmentation System

센티미터 급 광역 보강항법 시스템의 반송파 위상 기반 보정정보 생성 알고리즘에 관한 연구

지도교수 기 창 돈

이 논문을 공학박사 학위논문으로 제출함

2019 년 11 월

서울대학교 대학원
기계항공공학부
김 동 욱

김동욱의 공학박사 학위논문을 인준함

2019 년 12 월

위 원 장 : 김 현 진 (인)

부위원장 : 기 창 돈 (인)

위 원 : 박 종 포 (인)

위 원 : 허 문 범 (인)

위 원 : 이 상 율 (인)

Compact Wide-Area RTK
: A Study on Carrier Phase Based Correction Generation Algorithms for Centimeter-Level Satellite Augmentation System

Advisor Changdon Kee

Submitting a Ph.D. Dissertation of Engineering

November 2019

Graduate School of Seoul National University

Department of Mechanical and Aerospace Engineering

Donguk Kim

Confirming the Ph.D. Dissertation written by Donguk Kim

December 2019

Chair	**Hyoun-Jin Kim**	**(Seal)**
Vice Chair	**Changdon Kee**	**(Seal)**
Examiner	**Junpyo Park**	**(Seal)**
Examiner	**Moon-Beom Heo**	**(Seal)**
Examiner	**Sang-Ryool Lee**	**(Seal)**

ABSTRACT

Compact Wide-Area RTK
: A Study on Carrier Phase Based Correction Generation Algorithms for Centimeter-Level Satellite Augmentation System

Donguk Kim
Department of Mechanical and Aerospace Engineering
The Graduate School
Seoul National University

Recently, the demand for high-precision navigation systems for centimeter-level service has been growing rapidly for various Global Navigation Satellite System (GNSS) applications. The network Real-Time Kinematic (RTK) is one of the candidate solution to provide high-accuracy position to user in real-time. However, the network RTK requires a lot of reference stations for nationwide service. Furthermore, it requires high-speed data-link for broadcasting their scalar-type corrections.

This dissertation proposed a new concept of satellite augmentation system called “Compact Wide-Area RTK”, which provides centimeter-level positioning service on national or continental scales to overcoming the limitation of the legacy network

RTK methods. Using the wide-area network of multiple reference stations whose distance is 200~1,000 km, the proposed system generates three types of carrier-phase-based corrections: satellite orbit corrections, satellite code/phase clock (CPC) corrections, tropospheric corrections. Through the strategy of separating the scalar-type corrections of network RTK into vector forms of each error component, it is enable to expand network RTK coverage to continental scale using a similar number of reference stations as legacy meter-level Satellite-Based Augmentation System (SBAS). Furthermore, it is possible to broadcast their corrections over a wide-area using geosynchronous (GEO) satellite with extremely low-speed datalink of 250 bps likewise of legacy SBAS. To sum up, the proposed system can improve position accuracy by centimeter-level while maintaining the hardware infrastructure of the meter-level legacy SBAS.

This study mainly discussed on the overall system architecture and core algorithms for generating satellite CPC corrections and tropospheric corrections. This study proposed a new Three-Carrier Ambiguity Resolution (TCAR) algorithm using ionosphere-free combinations to correctly solve the integer ambiguity in wide-area without any ionospheric corrections. The satellite CPC corrections are calculated based on multiple stations for superior and robust performance under communication delay and outage. The proposed algorithm dramatically reduced the latency compensation errors and message amounts with compare to conventional RTK protocols. The tropospheric corrections of the compact wide-area RTK system are computed using GPS-estimated precise tropospheric delay and weather data based model together. The proposed algorithm adopts spherical harmonics function to significantly reduce the message amounts and required number of GPS reference stations than the network RTK and Precise Point Positioning-RTK (PPP-RTK),

while accurately modeling the spatial characteristic of tropospheric delay with weather data together.

In order to evaluate the user domain performance of the compact wide-area RTK system, this study conducted the feasibility test on mid-west and south USA using actual GPS measurements. As a result, the 95% horizontal position error is about 1.9 cm and the 95% vertical position error is 7.0 cm after the integer ambiguity is correctly fixed using GPS-only signals. The user ambiguity resolution takes about 2 minutes, and success-fix rate is about 100 % when stable tropospheric condition. In conclusion, the compact wide-area RTK system can provide centimeter-level positioning service to wide-area coverage with extremely low-speed data link via GEO satellite. We hope that this new system will consider as candidate solution for nationwide centimeter-level service such as satellite augmentation system of the Korea Positioning System (KPS).

Keywords: SBAS, compact RTK, network RTK, wide-area RTK, PPP-RTK, carrier-phase based correction, centimeter-level positioning

Student Number: 2013-23056

Intentionally Blank Page

TABLE OF CONTENTS

Intentionally Blank Page

LIST OF FIGURES

Intentionally Blank Page

LIST OF TABLES

ABBREVIATIONS

ADOP	Ambiguity DOP
AWS	Automatic Weather Station
bps	bits per second
CLAS	Centimeter Level Augmentation Service
COREA	COmpact RTK for Expanded Area
CORS	Continuously Operating Reference Station
CPC	Code/Phase Clock (or) Carrier-Phase Correction
CPRC	Carrier-Phase Rate Correction
DGPS	Differential GPS
DOP	Dilution of Precision
EWL	Extra-Wide-Lane
GBIF	Geometry-Based Ionospheric-Free
GEO	Geosynchronous Equatorial Orbit
GFIF	Geometry-Free Ionospheric-Free
GNSS	Global Navigation Satellite System
GPS	Global Positioning System
HPE	Horizontal Position Error
IGS	International GNSS Service
LAMBDA	Least-squares AMBiguity Decorrelation Adjustment
MAC	Master-Auxiliary Correction
METAR	MEteorological Terminal Air Report
MT	Message Type
NGS	National Geodetic Survey

NL	Narrow-Lane
NOAA	National Oceanic and Atmospheric Administration
OSR	Observation Space Representation
POD	Precise Orbit Determination
PPP	Precise Point Positioning
PRC	Pseudo-Range Correction
PRN	Pseudo-Random Noise
PRRC	Pseudo-Range Rate Correction
RMS	Root Mean Square
RTCM	Radio Technical Commission for Maritime services
RTK	Real-Time Kinematic
SBAS	Satellite-Based Augmentation System
SSR	State Space Representation
TCAR	Three-Carrier Ambiguity Resolution
TTFF	Time-To-First-Fix
VPE	Vertical Position Error
WADGPS	Wide-Area Differential GPS
WARTK	Wide-Area RTK
WL	Wide-Lane
WPF	WARTK Processing Facility
WRS	WARTK Reference Stations
WUF	WARTK Uplink Facility
ZHD	Zenith Hydrostatic Delay
ZTD	Zenith Tropospheric Delay
ZWD	Zenith Wet Delay

CHAPTER 1. INTRODUCTION

1.1 Motivation and Purpose

Recently, the demand for centimeter-level positioning has been growing rapidly for various applications such as autonomous vehicle driving, drone delivery service, collision avoidance, and smart farming using unmanned tractors. The Global Positioning System (GPS) and Global Navigation Satellite System (GNSS) allows users to calculate their location anytime, anywhere as long as they receive signals from more than four satellites [1]; however, the stand-alone GNSS cannot be used for applications requiring centimeter-level position because the accuracy is more than tens of meters. Therefore, the GNSS augmentation systems providing high-precision corrections have been studied for improving position accuracy over the past few decades. Among them, a Real-Time Kinematic (RTK) which uses carrier-phase observations is a typical technique to obtain centimeter-level position [2].

The traditional RTK is a kind of Differential GPS (DGPS) that uses the carrier-phase observations from reference stations whose distance is less than 10~20 km to the users. Once the RTK users correctly determine their integer ambiguity included in carrier-phase observations, they can calculate the centimeter-level position in real time. However, the performance has been restricted to very short-baseline distance due to the spatial correlated GNSS errors such as ionospheric delay and tropospheric delay [3]. The network RTK has been developed in order to expand RTK coverage per station. Multiple reference stations with a distance to 50~70 km are utilized to

generate accurate carrier-phase-based corrections. Traditionally, the RTK technique has been widely used for geodesy and surveying. In recent years, the network RTK has become a candidate solution for land vehicle navigation because it can quickly and accurately determine the position of dynamic users [4], [5].

Though it is very useful technique for high-accuracy positioning, there are two limitations on the network RTK system. First of all, it requires a lot of continuously operating reference stations (CORS) equipped high-cost permanent receivers to provide centimeter-level services for nationwide or continental. If the distance between reference stations is more than 70 km, the network RTK corrections represented by scalar-range forms cannot sufficiently reduce the GNSS spatial correlated errors contained in user measurements. Therefore, more than hundreds of reference stations are needed to provide centimeter-level services across the country, such as the entire South Korea [3]. Second, the network RTK requires high-speed datalink for broadcasting their scalar-type corrections. Since the corrections are generated for each satellite at each reference station, the system requires higher data bandwidth as the number of satellites and stations increases. In addition, because of its large size and non-linear nature, the conventional RTK corrections not only require large message amount, but also very vulnerable to communication failures [6], [7]. Generally, it requires a high-speed datalink of 2,000 to 4,000 bits per second (bps) to maintain centimeter-level services [5].

This thesis proposes a new concept of augmentation system called “Compact Wide-Area RTK” to overcome the limitations of legacy network RTK system. This new system can provide centimeter-level positioning services in real time on nationwide or continental scales using small number of reference stations whose

baseline distances are 200~1,000 km. Unlike the scalar-type corrections of network RTK, this new system calculates carrier-phase based corrections into vector forms for each GPS error components. These vector-type corrections consists of satellite orbit correction, satellite Code/Phase Clock (CPC) correction, and tropospheric correction. Through this strategy, it is enable to expand the network RTK coverage to nationwide scale using a few reference stations. In fact, only 5~7 reference stations are necessary for 1,000 km radius achieving centimeter-level services. In other words, the infrastructure of proposed system requires a similar number of reference stations as meter-level Satellite Based Augmentation System (SBAS) such as Wide-Area Augmentation System (WAAS) in USA or Korea Augmentation Satellite System (KASS) in South Korea. Furthermore, it is available to broadcast the compact wide-area RTK corrections over the continent through a geostationary (GEO) satellite with very low-speed datalink of 250 bps like meter-level SBAS. As a result, the user who receiver the high-precision corrections from the geostationary satellite can quickly and correctly solve their double-differenced integer ambiguity and determine centimeter-level position. The final objective of the proposed system is to provide a centimeter-level accuracy normally in less than a minute with multi-GNSS multi-frequency signals. The compact wide-area RTK system has the advantage of utilizing the infrastructure of meter-level SBAS to enable centimeter-level services. That is, the compact wide-area RTK will reduce the operational and maintenance cost of the system infrastructure dramatically.

As the first research to propose the compact wide-area RTK system, this thesis mainly focuses on the overall system architecture. Furthermore, this thesis introduces the core algorithms for generating satellite CPC corrections and tropospheric corrections using multi-frequency carrier-phase observations. The

novel method is proposed to make satellite CPC corrections that is very robust under communication failure while dramatically reducing the amount of message. This study also propose efficient algorithms for generating tropospheric corrections through modeling the spatial characteristic using weather data together.

1.2 Former Research

Many research have been conducted on centimeter-level positioning systems using carrier-phase observations. This section introduces the major research trends and describes the limitations of previous studies.

The Network RTK using multiple reference stations has been studied since late 1990's to expand the coverage of single-station based traditional RTK [8]. There are three different techniques according to the correction types: Master-Auxiliary Concept (MAC) [9], Virtual Reference Station (VRS) [10], and Flächen-Korrektur Parameter (FKP) [11]. These network RTK corrections are under discussion as the standard of Radio Technical Commission for Maritime services (RTCM) [12]. Among them, the MAC is most suitable for dynamic users, considering one-way communication link and representation errors. However, the network RTK requires high-speed data-link about 2,000~4,000 bps to broadcast their corrections and the service coverage per network is still narrow at 50~70 km [4], [5].

The Compact Network RTK that combines MAC-based network RTK and compact RTK techniques was proposed in order to reduce the data bandwidth of the network RTK [3], [6]. The Compact RTK is a technique to minimize latency errors by reducing time-varying components in GPS-RTK corrections [13], [14]. The compact RTK protocol is currently assigned in RTCM Message Type (MT) 4081 for

GPS L1/L2 signal [5]. The conventional MAC-based network RTK requires more than 1,900 bps assuming configuration with one master station and five auxiliary stations. On the other hand, the compact network RTK that uses the compact RTK protocol instead of the raw observations of RTCM MT 1004, requires only 700 bps to achieve the same accuracy [15]. However, even the compact network RTK require more data bandwidth as the number of station increase. In addition, the radius of service area is still narrow at 50~70 km.

The Wide-Area RTK (WARTK) concept based on precise real-time ionospheric modeling was proposed in Europe to dramatically increase the coverage of network RTK services [16]–[18]. In this new augmentation system with multiple stations hundreds of kilometers apart, the real-time ionospheric filter was combined with the traditional Three-Carrier Ambiguity Resolution (TCAR) [19] algorithm. Therefore, users with multi-frequency signals can calculate the centimeter-level position within the wide-area network. However, due to the estimation of tropospheric delay in user navigation filter, it takes about 5~15 minutes to converge the centimeter-level position [20]. Furthermore, this system is vulnerable to communication failures in that it broadcasts six linear combinations of raw measurements from only one reference stations to eliminate satellite clock [21]. It is difficult to actively respond to a breakdown of the applicable reference station that is broadcasting the corrections.

The Precise Point Positioning (PPP) is absolute positioning concept using un-differenced ionospheric-free combination with precise orbit and clock data from global GPS network [22]. PPP enables users around the world to compute their position with decimeter or centimeter accuracy; however, the very-long convergence times of about 30 minutes to an hour are required because the ionospheric-free

combination does not preserve integer nature of ambiguities [23]. The PPP-RTK concept was proposed to overcome the limitations of PPP. This concept enables recovery of integer property of ambiguities through additional corrections from RTK reference networks to reduce PPP convergence times. PPP-RTK system generate the precise corrections using state-space modeling by each error components. This can be termed as State Space Representation (SSR). In contrast to this, the observation corrections of traditional RTK are called Observation Space Representation (OSR) [7], [24]. The satellite orbit, clock and signal bias are estimated by the global GPS networks. The corrections for ionospheric and tropospheric delay is modeled by the local RTK networks with a distance of 10~50 km between reference stations. In order to accurate model the ionospheric and tropospheric delay, PPP-RTK requires a huge number of locally located reference stations equipped high-cost permanent receiver. For example, the Centimeter-Level Augmentation Service (CLAS) in Japanese Quasi-Zenith Satellite System (QZSS) that adopts the PPP-RTK technique collects the GNSS observation data from more than 1,200 stations located nationwide for generating the correction information [25]–[27]. Moreover, although the PPP-RTK message has not yet been standardized, it requires a large bandwidth at 2,000 bps in order to broadcast grid-based ionospheric and tropospheric corrections [28]–[30].

The concept of Compact Wide-Area RTK was first introduced by D. Kim et al. (2019) [31]–[33]. The proposed system is a new concept of system that only combines the advantages of SBAS, network RTK, and PPP-RTK through overcoming each disadvantage. We named “COREA (COmpact RTK for Expanded Area)” as the abbreviation for compact wide-area RTK system. This dissertation contains more detailed algorithms and analysis results, including the contents of the three previous conference proceedings.

1.3 Outline of the Dissertation

This thesis includes the compact wide-area RTK system architecture, main algorithms, and verification test results with real observed GPS data.

Chapter 2 is a background for GNSS augmentation system. GNSS measurements and its error sources are introduced and explained. The special error components for precise positioning as well as traditional GPS errors are described in this chapter. In addition, the advantage and disadvantage of conventional GNSS augmentation systems as well as their basic algorithms are discussed. Pseudorange-based SBAS, carrier-phase-based RTK and PPP techniques are described.

Chapter 3 introduces the concept of the compact wide-area RTK system and the overall architecture. The strategy of separating the conventional scalar-type RTK corrections into vector forms of each error component is discussed. Furthermore, the ambiguity resolution and validation algorithms for correction generation and user positioning are mainly described. The proposed system focuses on the users who can receiver dual- or triple-frequency signals. Therefore, this chapter discusses the new TCAR method based on ionospheric-free combinations of multi-frequency signals.

Chapter 4 describes the main algorithms for generating satellite CPC corrections of compact wide-area RTK system. The techniques to produce the satellite CPC corrections based on multiple stations for the robustness to communication failure is discussed. Real GPS observed data is used to analysis the performance under the latency. Required data bandwidth for message broadcasting is also described.

Chapter 5 describes the main algorithms for generating tropospheric corrections of compact wide-area RTK system. This chapter discuss how the weather data can be used to effectively model the spatial characteristics of the tropospheric delay on wide-area. The spherical harmonics function based modeling algorithm is proposed as a method to dramatically reduce message amount while maintaining high-accuracy.

Chapter 6 describes the user performance verification results. As applying the compact wide-area RTK corrections to the users, the range domain residual error, ambiguity resolution performance, and position accuracy are analyzed and summarized.

Chapter 7 presents conclusions from the results of this research and suggest for further research.

1.4 Contributions

The main contribution of this thesis is the conceptual design of the compact wide-area RTK system and the development of core algorithms and architecture. This thesis is the first study introducing the detailed algorithms of the compact wide-area RTK system, which provides centimeter-level positioning services in wide-area via GEO satellite broadcasting. Furthermore, the potential and performance of the proposed system has been verified using the actual GPS measurements. The detailed contributions are summarized below.

1. This thesis proposes a new ambiguity resolution method using multi-frequency signals for reference stations and dynamic users in wide-area. Unlike the traditional TCAR method used in WARTK system on Europe, the new geometry-based ionosphere-free linear combinations are possible to correctly fix the integer ambiguity even long-baseline distance without additional ionospheric corrections. This study is discussed in detail in Chapter 3.

2. This thesis proposes a new algorithm for generating satellite CPC corrections to eliminate satellite clock error. The conventional RTK based on double-difference can be completely eliminated with OSR corrections generated by each reference stations; however, it require a high-speed data link because OSR corrections are very vulnerable to communication failures. The proposed algorithm uses multiple stations together to generate robust, high-quality corrections in communication failure environment. In addition, the required message amounts can be greatly reduced. This method effectively overcome problems with systems such as the traditional RTK, network RTK, and WARTK in Europe that generate OSR type corrections. This study is discussed in detail in Chapter 4.

3. This thesis propose a new algorithm for generating zenith tropospheric corrections to reduce tropospheric delay error. Generally, a large number of closely distributed reference stations are required for generating the high-accuracy tropospheric corrections like the PPP-RTK. This new method can be significantly reduced the number of reference stations and even message amounts by efficiently using additional weather data while maintaining the

PPP-RTK level accuracy of corrections. This study is discussed in detail in Chapter 5.

4. This thesis contains the feasibility test results on user domain using real GPS observations. The compact wide-area RTK system achieved centimeter-level positioning accuracy for a coverage of 1,000 km in radius using only 6 reference stations. Furthermore, the compact wide-area RTK system requires only 250 bps datalink like legacy SBAS. This performance is not possible with the conventional network RTK and PPP-RTK system. This results are discussed in detail in Chapter 6.

5. In summary, the proposed system contributes significantly in that it is a new concept to overcome the limitations of SBAS, network RTK, and PPP-RTK systems. The advantage of each augmentation system are combined. This thesis is base study for the development of GEO broadcast-based satellite augmentation system for nationwide centimeter-level services. It can improve position accuracy by centimeter-level while maintaining the hardware infrastructure of the meter-level legacy SBAS.

CHAPTER 2. OVERVIEW OF GNSS AUGMENTATION SYSTEM

2.1 GNSS Measurements

The GNSS satellites have highly accurate atomic clock which are in synchronism with each other, and the GNSS users can estimate their three-dimensional position and time anytime, anywhere as long as they receive GNSS signals from more than four satellites. The GNSS utilizes the concept of one-way time of arrival ranging. Recently, many countries have been developed and operated independent satellite navigation system such as GPS for USA, Galileo for Europe, Beidou for China, GLONASS for Russia, and QZSS for Japan [1]. Among them, GPS satellites transmit their signals through L1 (1575.42 MHz) and L2 (1227.6 MHz) frequencies. Each satellite signal is encrypted by a unique binary pseudo-random noise (PRN) modulation based on a code division multiple access (CDMA). Through the GPS modernization plan, L5 (1176.54 MHz) frequency is also provided by block IIF. As of April 24, 2019, there were a total of 31 operational satellites in the GPS constellation: one block IIA, 11 block IIR, 7 block IIR-M, and 12 block IIF. GPS has plan to full operation of L5 signal in 2024 [34]. Other GNSS systems also provide or plan to provide triple-frequency signals. Accordingly, a lot of studies on high-precision navigation systems using dual- or triple-frequency signals are of interest and are being carried out continuously.

GNSS provides two types of measurements. First, code tracking loop of the GNSS receiver provides the pseudorange measurements, the apparent transit time of signals from the satellite to the receiver. It defined as the difference between signal reception time, as determined by the receiver clock, and the transmission time at the satellite. The pseudorange measurements have meter-level receiver noise. Second, phase tracking loop of the GNSS receiver provides the carrier phase measurements that is much more precise than the pseudorange measurements. The carrier phase measurement is the difference between the phases of the receiver-generated carrier signal and the carrier receiver from a satellite at the instant of the measurements. When the receiver locks the carrier phase, phase value within one wavelength can be measured precisely in millimeter-level; however, the total number of wavelengths, which has passed during signal transit time, is unknown. These phase cycle is called integer ambiguity, and the integer ambiguity should be resolved for carrier-phase based precise positioning [1]–[4].

The GNSS measurements have various errors as well as satellite and receiver clock errors. The transmitted signal from the satellite is delayed or advanced when it passes through the ionosphere and troposphere. There are also errors caused by the receiver itself or by the installed environment. The GNSS users, who want to achieve high-accuracy position, should eliminate or reduce all of error sources included in the measurements through modeling or corrections. Pseudorange and carrier-phase measurements can be modeled as follow equations. Each error sources are described in the next section.

$$\rho = d + \delta R - \left(b + \delta b + \beta_{\rho}^{Tx}\right) + I + T + \left(B + \beta_{\rho}^{Rx}\right) + \varepsilon_{\rho} \quad \textbf{(2.1)}$$

$$\phi = d + \delta R - \left(b + \delta b + \beta_{\phi}^{Tx}\right) - I + T + \left(B + \beta_{\phi}^{Rx}\right) + \lambda N + \varepsilon_{\phi} \quad \textbf{(2.2)}$$

where

ρ : pseudorange measurement (m)

ϕ : carrier phase measurement (m)

d : geometry distance between receiver and satellite (m)

δR : satellite orbit residual error of line-of-sight direction (m)

b : satellite clock offset by broadcast parameters (m)

δb : satellite clock residual error (m)

I : ionospheric delay (m)

T : tropospheric delay (m)

B : receiver clock offset (m)

β_{ρ}^{Tx} : satellite hardware bias – code delay (m)

β_{ϕ}^{Tx} : satellite hardware bias – phase delay (m)

β_{ρ}^{Rx} : receiver hardware bias – code delay (m)

β_{ϕ}^{Rx} : receiver hardware bias – phase delay (m)

λ : wavelength of carrier phase (m)

N : integer ambiguity (cycle)

ε_{ρ} : pseudorange noise and multipath (m)

ε_{ϕ} : carrier phase noise and multipath (m)

2.2 GNSS Error Sources

This section introduces the GNSS error sources that should be considered in the GNSS augmentation systems. The special error sources to be considered for the centimeter-level navigation as well as the traditional error sources are described.

2.2.1 Traditional GNSS Error Sources

1) Satellite Orbit Error

GPS control segment estimates the predicted satellite position, and broadcast the ephemeris parameters as navigation messages to users. The satellite orbit error or called ephemeris error is induced by the difference between the predicted orbit and actual satellite orbit. Typical magnitudes of satellite error is about RMS 3 m. The satellite orbit error is usually divided into three orthogonal directions: the radial (R), along-track (A), and cross-track (C), as shown in Figure 2.1. The radial component has the smallest value since the estimation of an orbit is based on range measurements. The along-track and cross-track components are known to be relatively larger. The effective error in pseudorange and carrier-phase measurements due to satellite orbit errors can be calculated by projecting the error vector onto the satellite-to-user line-of-sight vector. Fortunately, the satellite orbit error in user measurements is as small as about RMS 1 m, since it depends mostly upon the radial component of satellite orbit. The component of along-track and cross-track projected onto the line-of-sight direction are relatively small [1], [2]. The compact wide-area RTK will reduce these error by precise corrections.

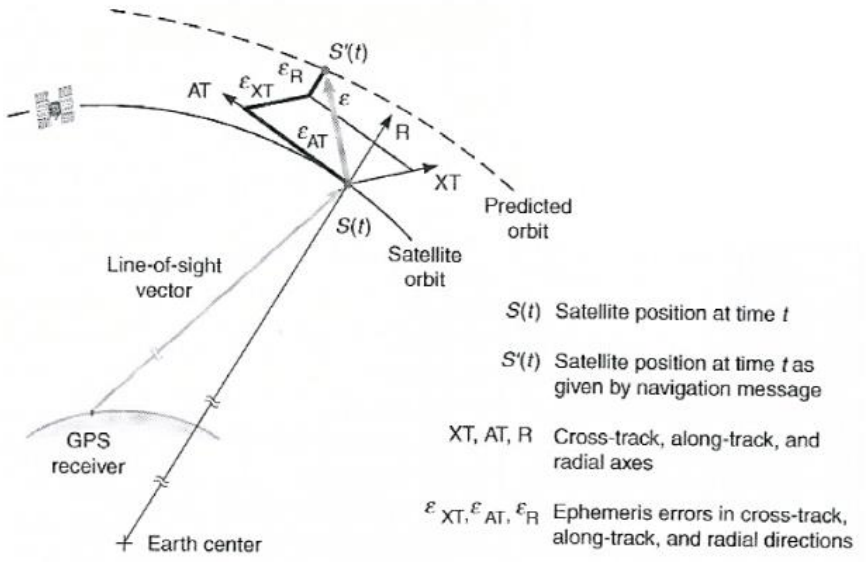

Figure 2.1 Satellite orbit error components in radial, along-track, and cross-track [2].

2) Satellite Clock Error

Each GPS satellite is equipped with high-stable atomic clocks for synchronization of system clock. Although these Cesium and Rubidium oscillator for space with 10^{-14}~10^{-13} sec/sec stability, the clock offset between satellite time and GPS time may be as large as 1 msec. Therefore, in order to compensate this satellite clock error, the correction parameters are modeled as 2nd order polynomial as following equation [1], [2].

$$b = a_{f_0} + a_{f_1}(t - t_{oc}) + a_{f_2}(t - t_{oc})^2 + \Delta t_r \qquad \textbf{(2.3)}$$

where

a_{f_0} : satellite clock bias (sec)

a_{f_1} : satellite clock drift (sec/sec)

a_{f_2} : frequency drift (sec/sec2)

t : current GPS time (sec)

t_{oc} : clock navigation data reference time (sec)

Δt_r : correction due to relativistic effects (sec)

Since these corrections estimates the satellite clock offset using a curve-fit, some residual error remains. This residual clock error δb affects in measurements typically 0.3 ~ 4 m, depending on the types of satellite and age of the navigation messages [1], [2]. The compact wide-area RTK will completely eliminate these errors with the proposed precise corrections, which are discussed in detail in Chapter 4.

3) Ionospheric Delay

The ionosphere is a region of the ionized gases, 50 km to 1,000 km above the Earth's surface. The ionization is caused by the sun's radiation, and the intensity of solar activity determine the density of free electrons in the ionosphere. These free electrons influence propagation of electromagnetic wave including the GPS signals. The speed of propagation of radio signals in the ionosphere depends upon the number of free electrons in the signal path, defined as the total electron content (TEC). The ionosphere is a dispersive medium that delays in GPS signal vary depending on the signal frequency f. The ionospheric delay terms in measurements of pseudorange and carrier-phase are equal in magnitude by opposite in sign because the phase

velocity exceed the group velocity, i.e., the phase is advanced [1], [2].

$$I = I_\rho = -I_\phi = \frac{40.3}{f^2} TEC \tag{2.4}$$

The ionospheric delay is the largest error sources in GPS signals that the zenith delay is typically about 5~15 m at mid-latitudes in mid-afternoon. The slant ionospheric delay can be observed more than 50 m in measurements. Unfortunately, the ionospheric delay is very difficult to model and estimate, only the 60% of delay can be eliminate through such as Klobuchar model. A residual error of several meters still remain in pseudorange and carrier-phase measurements. Nevertheless, since the ionospheric delay is frequency dependent, it can be virtually eliminated with a dual- or multi-frequency receiver. The ionospheric-free pseudorange measurements using L1 and L2 frequency signals can be formed as follow [1], [2].

$$\rho_{IF} = \frac{\gamma\rho_1 - \rho_2}{\gamma - 1} \tag{2.5}$$

where $\gamma = (f_1 / f_2)^2$. Although the measurement noise are significantly magnified approximately 3 times by this formula, the compact wide-area RTK will completely remove the ionospheric delay errors through the ionospheric-free linear combinations.

4) Tropospheric Delay

The troposphere is a non-dispersive medium, which is the lower part of the atmosphere up to about 10 km above the Earth's surface. Within this medium, the signal delay is induced same magnitude and sign regardless of transmission frequency. The tropospheric delay is a function of the atmospheric refractive index (slightly larger than 1), which is dependent on the local temperature, pressure and relative humidity. Uncompensated this error, the measurements have a delay about 2.5 m in zenith direction, and up to 25 m for a satellite at 5 degree elevation angle. In order to reduce the tropospheric delay error, the refractivity is often modeled as a hydrostatic (or dry) part and wet part. The hydrostatic component caused by atmospheric gases in hydrostatic equilibrium accounts for 90% of the tropospheric delay, and can be predicted very precisely. On the other hand, the wet component arose from the water vapor is more difficult to model due to uncertainties in the atmospheric distribution. The simple tropospheric delay model can be expressed as following equation. The slant delay is modeled as zenith hydrostatic delay (ZHD) and zenith wet delay (ZWD) with together each corresponding mapping function, which is a function of satellite elevation angle. The typical tropospheric model can compensate the tropospheric delay within the accuracy of 20 cm [1], [2].

$$T = ZHD \cdot m_{hyd}(El) + ZWD \cdot m_{wet}(El) \quad \textbf{(2.6)}$$

The compact wide-area RTK will reduce these errors with the proposed precise corrections, which are discussed in detail in Chapter 5.

5) Receiver Clock Offset

The receiver clock offset is caused by oscillator used in the receiver, typically a quartz crystal oscillator with a drift rate of 10^{-8}~10^{-9} sec/sec. This error is usually large in size and has non-linear characteristics of time. However, the receiver clock offset are common to all measurements in satellite, so most of the error can be eliminated in navigation solution [35]. The compact wide-area RTK will perfectly eliminate the clock offset through differences in measurements between satellites.

6) Receiver Noise and Multipath

The pseudorange and carrier phase are affected by random measurement noise. The noise induced by the antenna, amplifiers, cables, and receiver tracking loops. The measurement error due to receiver noise varies with the signal strength, which, in turn, varies with the satellite elevation angle. It can be approximated as a white Gaussian noise. Standard deviation of the typical receiver noise is approximately 1~2 m for pseudorange and 2~3 mm for carrier-phase [2], [36].

Multipath is occurred when the signals with two or more paths are received by the antenna. Typically, the antenna receives the direct signal on line-of-sight direction and its reflected signal from the buildings, metallic materials, tree, and ground, etc. The reflected signal is a delayed and usually weak than the direct signal. As a result, it changes the shape of direct signal in receiver tracking loop, and the measurements error are induced by the strength of the reflected signal and the delay between the direct and reflected signal [1], [2].

The receiver noise and multipath often modeled by the function of satellite elevation angle as following equation [3], [36], [37]. The compact wide-area RTK will apply the following standard deviation models for receiver noise and multipath of pseudorange and carrier-phase measurements designed with over-bound techniques [38]. SF means the over-bounding scale factor to ensure the uncertainty. Figure 2.2 shows the example of carrier-phase noised and multipath modeling by actual GPS data, and Table 2.1 summarizes the modeling results.

$$\sigma_{El} = SF \cdot \left\{ a_0 + a_1 \cdot \exp\left(-\frac{El}{a_2} \right) \right\} \tag{2.7}$$

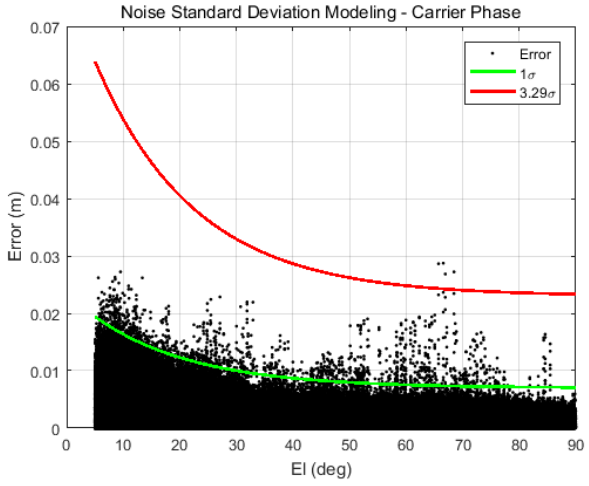

Figure 2.2 Over-bounding modeling for carrier-phase noise and multipath

Table 2.1 Results of receiver noise and multipath modeling

	a_0	a_1	a_2	SF
Pseudorange	0.1247	0.6135	27.1483	4.8
Carrier phase	0.0010	0.0025	17.6748	6.7

2.2.2 Special GNSS Error Sources

1) Signal Hardware Bias

Such signal biases, which are time delays within the GNSS satellite and receiver, are induced by difference in electrical path of signal in their hardware system. This means that the given time from the satellite clock is not equal to the signal emission time, and the given reception time by receivers is the time when the signal was demodulated by linking the internal receiver clock, as shown in Figure 2.3. The hardware biases dependent on signal frequency, signal type, receiver tracking method, and receiver type [39]–[41].

The signal code bias on pseudorange measurements and signal phase bias on carrier-phase measurements are non-negligible error sources for GNSS augmentation systems. Generally, the receiver signal biases are absorbed in receiver clock offset that is not affected to calculate absolute positioning, while the satellite signal biases should be compensated using such corrections for precise positioning. Currently, the satellite code biased are compensated using the corrections of differential code bias (DCB) that is generated from global or local network [40]. With GPS modernization, the new inter-signal correction (ISC), as shown in Figure 2.4, will be provided as ephemeris parameters for calibrating satellite code bias [42]–[44].

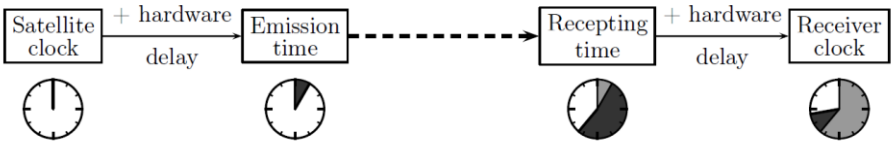

Figure 2.3 Satellite and receiver hardware delay [39]

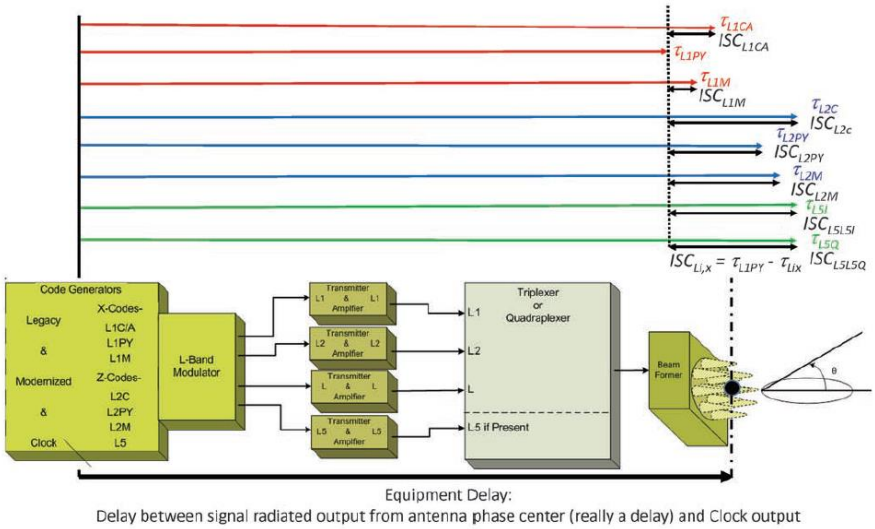

Figure 2.4 Satellite hardware delays of IS-GPS-200 model [44]

The signal phase biases are a major concern of centimeter-level positioning such as RTK and PPP. The satellite phase biases differ for each satellite and for each carrier frequency, and some of which tend to merge into the integer ambiguity. This is not a problem when using the ionospheric-free combinations for PPP because the ambiguities are no longer integers. However, this aspect becomes a serious problem when determining ambiguity as an integer, such as RTK and PPP-RTK system. The RTK system, which provides the observation of reference stations can be completely eliminated the phase bias through single-difference between stations. On the other hand, such the PPP-RTK system requires precise corrections for calibrating satellite phase biases [45]–[48]. Generally, it is difficult to generate the phase bias corrections on local GNSS network; therefore, the PPP-RTK depends on the global network like the international GNSS service (IGS). The compact wide-area RTK will generates the merged corrections for satellite clock and hardware bias using local network for calibrating these error sources.

2) Antenna Phase Center Offset and Variation

The GNSS signal is transmitted from the phase center of the satellite antenna. The difference between mass center of satellite and antenna phase center of satellite is referred as satellite antenna phase center offset (PCO). The PCO for most satellites are in the body z-coordinate direction towards the Earth and in the body x-coordinate direction which is on the plane containing the Sun, as shown in Figure 2.5. The satellite antenna PCO varies a few millimeter according to the direction of nadir angle. This deviation of the PCO is called satellite antenna phase center variation (PCV) [49]–[51].

Likewise, the GNSS signal is received at phase center on the receiver antenna. The separation between the antenna reference point (ARP) and the phase center of the receiver antenna is called the receiver antenna PCO. The receiver antenna PCO also varies a few millimeter according to changing direction of the GNSS signal, since this electrical phase center of a receiver antenna is difference from the center of physical mark. This effect is referred as receive antenna PCV, as shown in Figure 2.6, and the magnitude and direction usually depends on the satellite elevation angle. The azimuth angle affects very small on the PCV [51], [52].

The measurement error induced by PCO is a few centimeter and PCV is a few millimeter that they must be taken into account in high-precision navigation system. The compact wide-area RTK will apply the pre-estimated value of the phase center offset and variation for satellite and receivers provided by IGS through the Antenna Exchange Format (ANTEX).

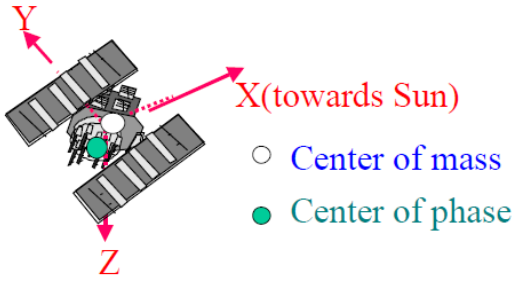

Figure 2.5 Satellite antenna phase center offsets
in satellite body fixed reference frame [50]

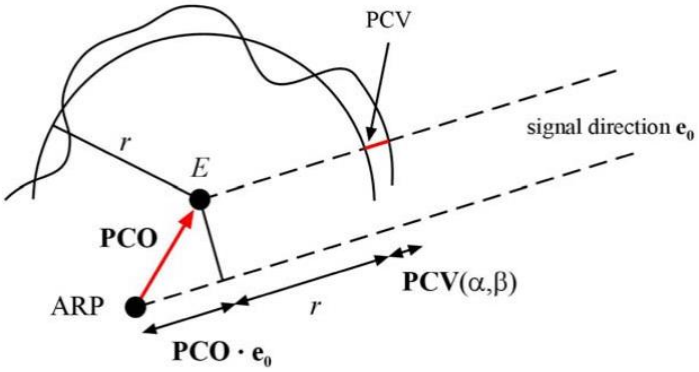

Figure 2.6 Receiver antenna phase center offset and variation [52]

3) Phase Wind Up

The carrier-phase observations are dependent on the relative orientation of the satellite and receiver antennas due to the characteristics of the GPS signal that is right-hand circularly polarized. This effect is referred as phase wind-up. Phase wind up induces up to 1 cycle error in the carrier-phase measurements, not pseudorange. This effect is negligible for relative positioning like RTK when the baseline distance is within several hundreds of kilometers, while it cannot be neglected for absolute positioning such as PPP [50], [53].

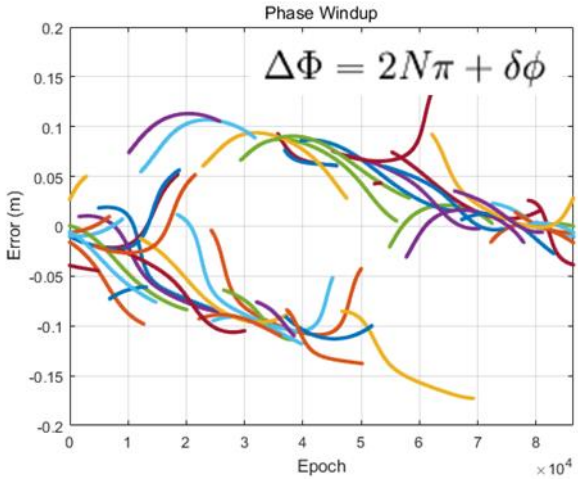

Figure 2.7 An example of phase wind-up corrections
(2014-09-01, DOND, Korea)

The corrections for the phase wind-up can be calculated by using effective dipole vector between receiver and satellite antennas [50], [53]. Figure 2.7 is an example of phase wind-up corrections at station located on Korea. The compact wide-area RTK will compensate the phase wind-up effect for generating precise carrier-phase based corrections using multiple stations located in continental scale areas.

4) Tide Effect

Since the Earth is not a rigid body, the shape of elastic body of the Earth is deformed by the gravitational attracting force imposed by the Sun and Moon. This phenomenon cause periodic deformation on the Earth and lead to vertical and horizontal site displacement, as shown in Figure 2.8. This effect is called solid Earth tides that can induce the displacement of up to 30 cm in height component and 5 cm in the horizontal plane, according to the station location, tide frequency, and sidereal time [49]. This site displacement caused by solid Earth tides should be calibrated for

centimeter-level positioning system such as the proposed compact wide-area RTK through the appropriate model given in the IERS Conventions 2010 [54], [55].

Similarly to the solid earth tides, the ocean tide loading, induced by the gravitational pull of the Sun and Moon, makes the deformation of elastic body of the Earth due to the weight of the ocean tides. The mass redistribution of the seawater by ocean tides cause periodic loading on the sea floor and adjacent land, as shown in Figure 2.9. This effect is negligible when the stations far away from coast lines. The site displacement caused by ocean tide loading should be compensated since it makes up to 10 cm error in height component. The model equations for ocean tide loading corrections is provided in the IERS Conventions 2010, and the compact wide-area RTK will apply the FES2004 model one of the pure hydrodynamic tide model [54], [55].

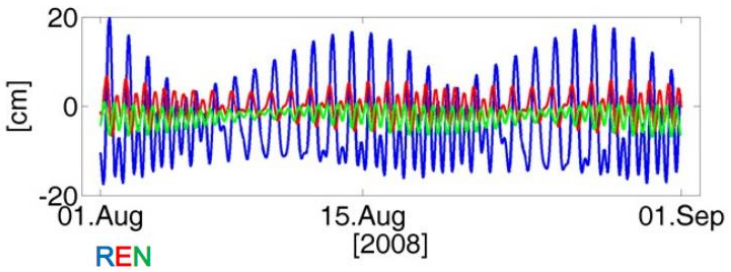

Figure 2.8 An example of solid earth tide effect [56]

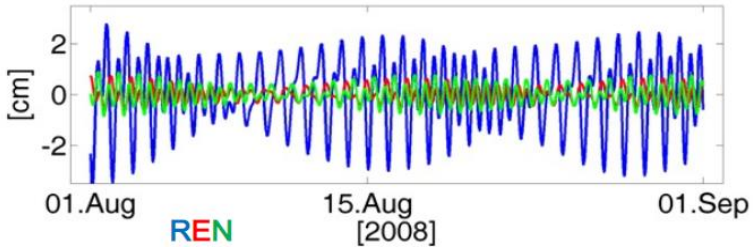

Figure 2.9 An example of ocean tide loading effect [56]

5) Relativistic Effect

Because of the large motion velocities and near circular orbits of the GNSS satellite, the relativistic effects is caused by the gravitational potential difference between the satellite and the receivers, as well as the rotation of the Earth [55]. Important relativistic effects on satellite clocks are subject to two effects: special relativity and general relativity. According to the theory of the special relativity, the satellite clock traveling at a constant speed appears slower than the clock on the ground due to the time dilation effect of their relative motion. This effect is called relativistic effects due to the orbit eccentricity, and it can be corrected by given equations in GPS-ICD 200 [42], [49]. According to the theory of the general relativity, the satellite clock appears to run faster than the one on the ground due to their difference in gravitational potential. This phenomenon is called relativistic path range effects that can be calculated appropriate model, as shown in Figure 2.10 [49], [57], [58].

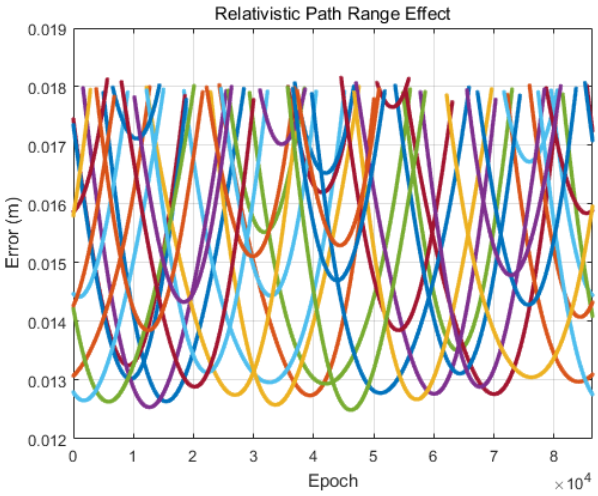

Figure 2.10 An example of relativistic path range effects (2014-09-01, DOND, Korea)

The relativistic effects related to the rotation of the Earth are called Sagna effect. This effect is induced error up to 30 m during the transit of the satellite signal from a satellite to a receiver, and must be taken into account even stand-alone positioning user. The corrections for Sagnac effects are summarized in following papers [55], [57], [58]

2.2.3 Summary

Table 2.2 summarizes the approximately budget of error sources and mitigation methods of the proposed compact wide-area RTK system. In particular, the special error sources in GNSS measurements should be calibrated to appropriate models for positioning centimeter-level accuracy.

Table 2.2 Summary of GNSS error sources and mitigation methods of compact wide-area RTK system

Error Source	***Error Budget***	***Mitigation Method***
Satellite orbit	1 m	Corrections
Satellite clock and hardware bias	4 m	Corrections (Proposed)
Ionospheric delay	50 m	Linear combinations
Tropospheric delay	25 m	Corrections (Proposed)
Receiver clock and hardware bias	~ m	Satellite-difference
Receiver noise and multipath	2 m	Filtering (see 3.1.2.)
Antenna PCO and PCV	10 cm	Model (ANTEX igs14)
Phase wind up	20 cm	Model
Tide effect	30 cm	Model (IERS 2010, FES2004)
Relativistic effect	cm ~ m	Model

2.3 GNSS Augmentation System

Generally, the position accuracy of stand-alone GNSS users is greater than 10 m because of the remaining GNSS error sources in measurements. For applications demanding an accuracy of less than one meter-level, a GNSS augmentation system is required [1], [2]. The GNSS augmentation system generates the corrections for reducing GNSS error components using the reference stations whose precise locations are known. The GNSS augmentation systems can be classified according to the types of measurements and correcting techniques. Typically, there are pseudorange based DGPS and SBAS that provide an accuracy about 1 m-level. There are RTK and network RTK that is the carrier phase-based relative position technique to obtain centimeter-level accuracy. Recently, the PPP and PPP-RTK that is the carrier phase-based absolute position technique are considered another type of systems. In this section, the advantage and disadvantage of these GNSS augmentation systems as well as their basic concept are discussed.

2.3.1 Satellite-Based Augmentation System (SBAS)

The DGPS, which provides the pseudorange observations of single reference station, is the most widely used augmentation system for 1~3 m position accuracy. This technique takes advantage of characteristics that GPS error sources have similar value for two different receivers whose baseline distance is sufficiently short. However, the DGPS performance is degraded due to the spatial decorrelation errors when users locates more than 200 km away from the reference station. In other words, the DGPS require a huge number of stations for providing service over nationwide [35], [59].

The Wide-Area DGPS (WADGPS) is proposed by Kee and developed in 1990's in order to overcome the limitation of DGPS. The corrections of the traditional DGPS is scalar observations that include all GPS error sources. On the other hand, the WADGPS estimates vector-type corrections for each error component for expanding service area. The system architecture of WADGPS consists of Wide-area Master Station (WMS), several number of Wide-area Reference Stations (WRS), and GEO Uplink Station (GEO), as conceptually shown in Figure 2.11. The WMS, which is the main processing facility of WADGPS, generates satellite orbit and clock corrections for each satellite, and grid-based vertical ionospheric corrections by using pseudorange measurements collected from the multiple WRS distributed over nationwide. Their estimated corrections are broadcasted to users via GEO satellite. Finally, the users can calculate their positions with 1 m-level accuracy by interpolating the vector-type corrections of WADGPS for their proper locations [35], [60]–[62].

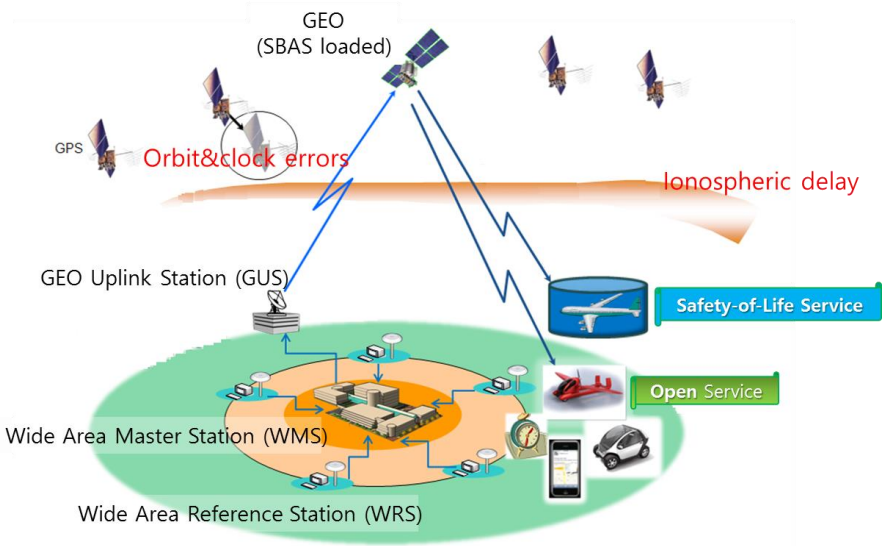

Figure 2.11 Conceptual figure of WADGPS and SBAS [62]

Recently, the WADGPS has been internationally standardized as the SBAS, which is safety critical system regarded as essential infrastructure in aviation fields such as aircraft landing. The SBAS provides the integrity information with corresponding to vector-type corrections for highly reliable and accurate positioning of users [62], [63].

The International Civil Aviation Organization (ICAO) recommended all nations to comply with the SBAS for navigation safety. The Wide-Area Augmentation System (WAAS) in USA, the European Geostationary Navigation Overlay Service (EGNOS) in Europe, the MTSAT Satellite based Augmentation System (MSAS) in Japan, and the GPS Aided GEO Augmented Navigation (GAGAN) in India are currently in operation. South Korea has also started the development of the Korea Augmentation Satellite System (KASS) has aimed to provide APV-I service for safety of life in 2022 [64].

The WADGPS and SBAS uses smaller number of reference stations compared to that of traditional DGPS for covering same size of region. It has significant benefits in terms of system and user infrastructures. The users with only a low-cost single-frequency receiver can be obtained 1 m level position accuracy and its reliability anywhere inside service network. However, the WADGPS and SBAS is not suitable for users want to require a centimeter-level position accuracy.

2.3.2 Real-Time Kinematic (RTK)

A RTK is a carrier-phase based navigation system which can be achieved centimeter-level position accuracy in real-time after correctly resolving the double-differenced integer ambiguity. The RTK technique is similar to the DGPS in aspect of differencing measurements between reference stations and users. The conventional single-station RTK has been constrained to be available within the distance between reference station and user under 10 km, due to the spatial decorrelation error likewise DGPS [3], [65].

In order to expand the service coverage of traditional RTK, a network RTK technique has been developed. The network RTK generates the high-precision corrections for reducing spatial decorrelation error effectively using the carrier-phase measurements collected from multiple reference stations. This technique can enlarge RTK coverage up to 70 km radius with 4~5 reference stations while maintaining centimeter-level accuracy at the same time [3], [4]. The network RTK is classified into three methods: MAC [9], VRS [10], and FKP [11]. These network RTK methods sharing a common goal are processed through several steps as shown in Figure 2.12, and all of them can be realized from the MAC approach [66]. The MAC approach, which is conceptually shown in Figure 2.13, is most suitable for a lot of dynamic users in RTK coverage considering one-way communication link and representation errors at user locations. The MAC-based network RTK can quickly and accurately determine user location; however, it requires high-speed data links about 2,000 bps to broadcast their corrections. In addition, the coverage area is still narrow at 50~70 km to service in nationwide [4], [5].

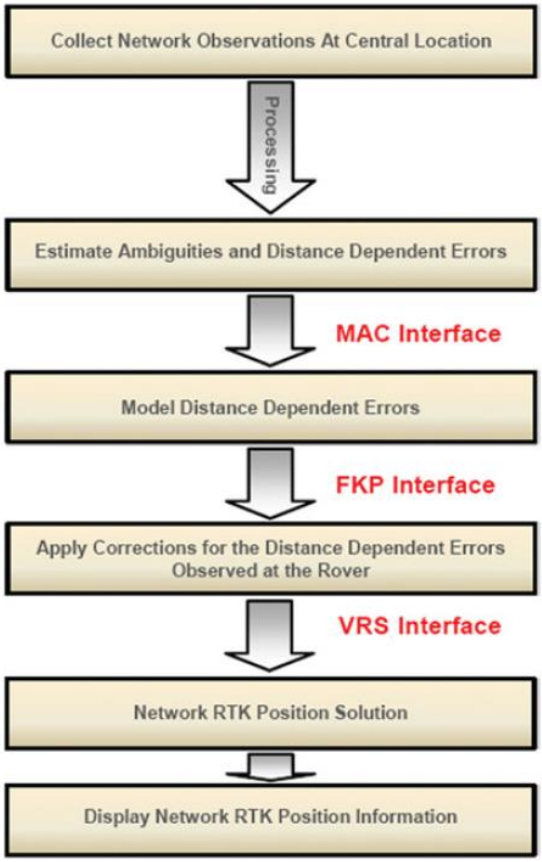

Figure 2.12 General processed involved in network RTK solutions [66]

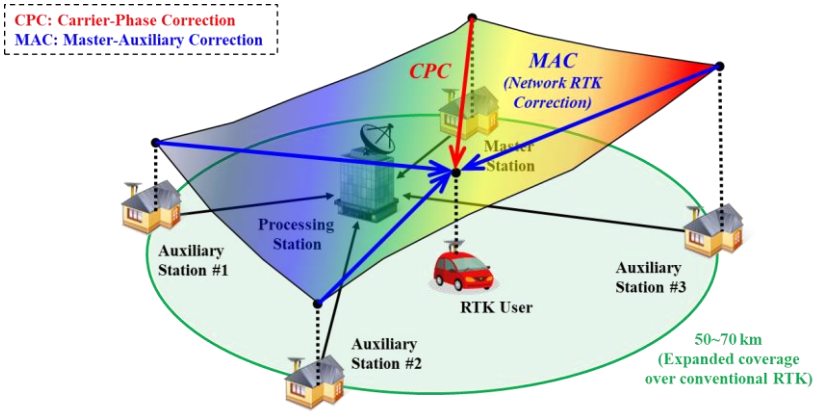

Figure 2.13 Conceptual figure of network RTK system

The WARTK concept, as shown in Figure 2.14, was first introduced in the late 1990s in Europe to dramatically expand the service coverage of RTK and network RTK, with permanent stations separated by up to 400~1,000 km. The most important product of this system is the precise ionospheric corrections modeled by dual-layer ionospheric tomography [16]–[18]. The ionospheric delay is the biggest error sources affecting the performance of long-baseline RTK users. As shown in **Figure 2.15**, The WARTK users equipped triple-frequency receiver can calculate centimeter-level position through the TCAR approach of solving the ambiguities from the longest to the shortest wavelength using the accurate real-time ionospheric corrections [21].

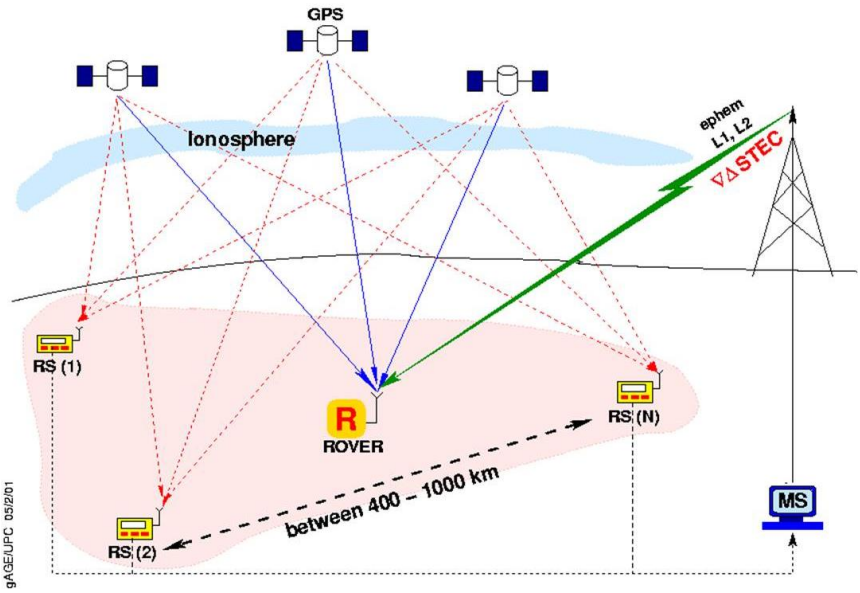

Figure 2.14 Conceptual figure of WARTK system of Europe [17]

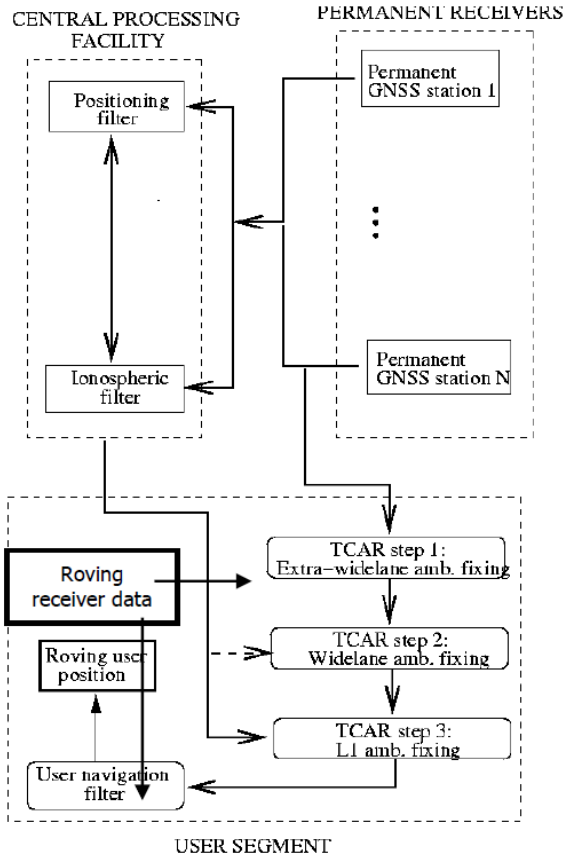

Figure 2.15 Block diagram of WARTK-3 algorithms of Europe [21]

Although the RTK service coverage is vastly expanded, this system still has the same limitation as RTK and network RTK. Because it broadcasts six linear combinations of raw measurements from only one master stations to resolve integer ambiguity, WARTK requires high-speed data link more than network RTK, and is very vulnerable to communications failures [21]. Furthermore, unlike network RTK, which is achieved accurate positioning in less than 1 minute, WARTK takes about 5~15 minutes to converge the position and relatively inaccurate than network RTK [20].

2.3.3 Precise Point Positioning (PPP)

Unlike the relative positioning of RTK that requires observations from reference stations, PPP is absolute positioning concept using un-differenced carrier-phase measurements of user receiver. PPP enables users around the world to compute decimeter or centimeter accuracy position with precise orbit and clock data from global GPS network. Typically, the mathematical model of PPP uses un-difference ionospheric-free combinations based on dual-frequency signals, which does not preserve integer nature of ambiguities. Therefore, PPP require very-long convergence times of about 30 minutes to an hour for high-accuracy positioning [22], [23].

The PPP-RTK system has been studied to overcome the limitations of PPP. This technique, which is a combination of PPP and RTK networks as shown in Figure 2.16, can reduce convergence time of PPP through recovering integer nature of ambiguities. The traditional RTK and network RTK generates observation-based corrections that is lump sum of all error components. This concept called Observation Space Representations (OSR) as shown in Figure 2.17. The OSR corrections should be generated per stations, per satellites, and per frequencies; therefore, a lot of data bandwidth are required to broadcasting. On the other hand, the PPP-RTK generates high-precision corrections using state-space modeling by each error components. This is termed as State Space Representation (SSR) as shown in Figure 2.18. The SSR corrections is not dependent on single reference stations like RTK, and their data bandwidth is significantly reduced compared to OSR corrections of RTK [7], [24].

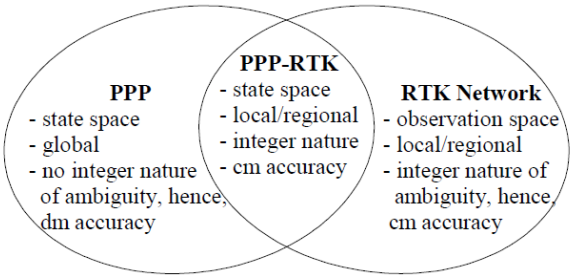

Figure 2.16 PPP-RTK: synthesis of PPP and RTK network [7]

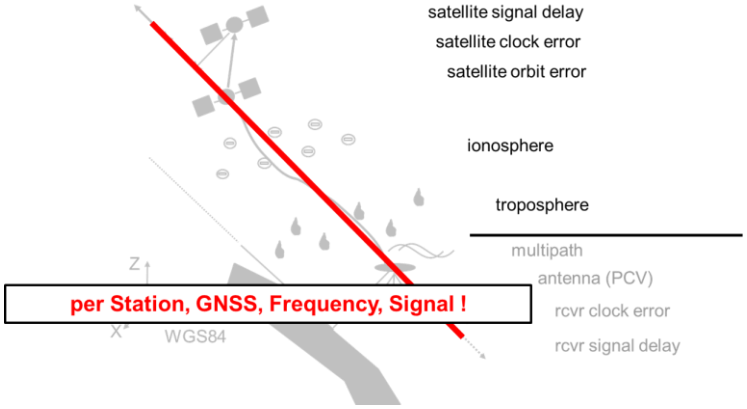

Figure 2.17 Concept of observation space representation (OSR)

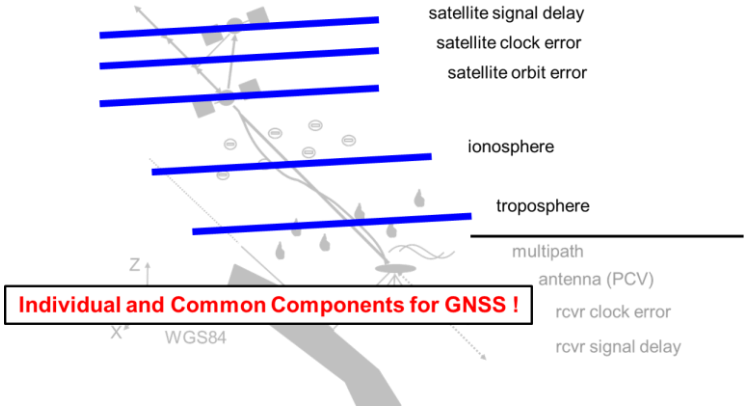

Figure 2.18 Concept of state space representation (SSR)

Typically, the satellite related SSR corrections, which consists of satellite orbit, clock and signal hardware bias are estimated by the global GPS network. The SSR corrections for ionospheric delay and tropospheric delay, which are local phenomenon, are modeled by the local RTK networks whose baseline distance is under 50 km. These SSR corrections can be easy to broadcast the message according to each update interval considering the each error characteristic unlike OSR corrections [7], [24]. The PPP-RTK can reduce the message bandwidth compare to network RTK while maintaining the centimeter-level accuracy. However, the PPP-RTK still requires a huge number of locally distributed reference stations equipped high-cost permanent receiver for nationwide service likewise the network RTK.

The Centimeter-Level Augmentation Service (CLAS) in Japanese QZSS, as shown in Figure 2.19, adopted the PPP-RTK technique is the world's first GEO broadcasting-based centimeter-level positioning system. The CLAS utilizes more than 1,200 stations located nationwide to generate SSR corrections for providing centimeter-level service in whole Japanese region. The CLAS corrections consist of satellite orbit corrections, clock corrections, code and phase bias corrections, gridded ionospheric corrections, and gridded tropospheric corrections. The message of these SSR corrections is broadcast to the users via L6 signals (1278.75 MHz) of GEO satellite. Although the PPP-RTK message has not yet been internationally standardized, the CLAS has been designed as their own compact SSR format for reducing data bandwidth to 2,000 bps. Table 2.3 summarizes the performance specifications of CLAS in Japanese QZSS. This system has been designed for multi-GNSS and multi-frequency signals [25]–[30].

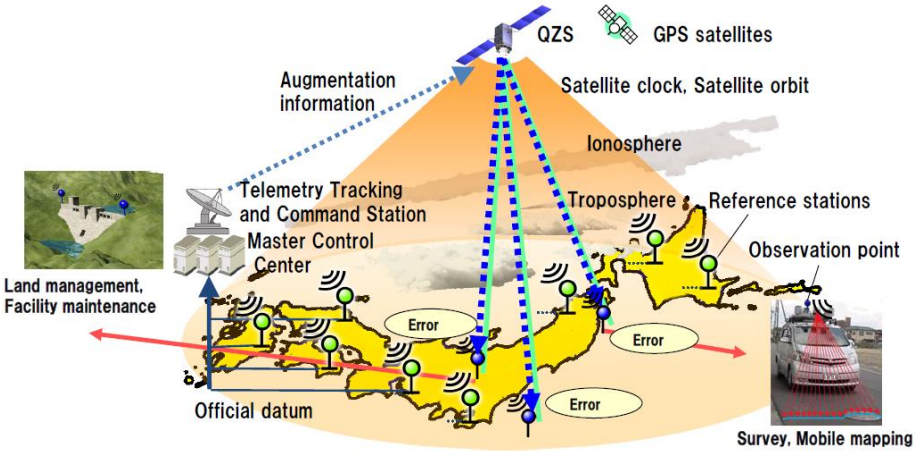

Figure 2.19 Conceptual figure of CLAS (PPP-RTK) system of Japan [25]

Table 2.3 Performance specifications of CLAS [27], [30]

Item	Specification
Augmentation Signal*	GPS:L1CA,L1C,L2P,L2C,L5 QZS:L1CA,L2C,L5 Galileo: E1B, E5a GLONASS(CDMA): L1OS, L2OS
Area	Japan with territorial waters
Positioning accuracy (open-sky, static)	Horizontal 6cm (95%) Vertical 12cm (95%)
Time to First Fix	<=60[s] (95%)
Service Availability	>=0.99 (constellation) >=0.97 (satellite) >=0.92 (high elevation(60deg))
TTA	<=10.2[s] (QZS-1) <=9.2[s] (QZS2-4)

* Augmentation for GLONASS and Galileo and GPS new signals are future services.

2.3.4 Summary

Figure 2.20 conceptually shows the performance comparison that focuses on the position accuracy and coverage per station of the traditional GNSS augmentation systems introduced in the previous subsections. Table 2.4 summarizes the pros and cons of each systems. The green color is the advantage, and the red box means the limitation. The yellow color is not a bad or good feature. The proposed system called compact wide-area RTK is a new concept to overcome the limitations of SBAS, network RTK, and PPP-RTK systems. The advantage of each augmentation system are combined. The compact wide-area RTK aim to centimeter-level accuracy uniformly within 1,000 km coverage utilizing the SBAS infrastructure. The details are described as following Chapters.

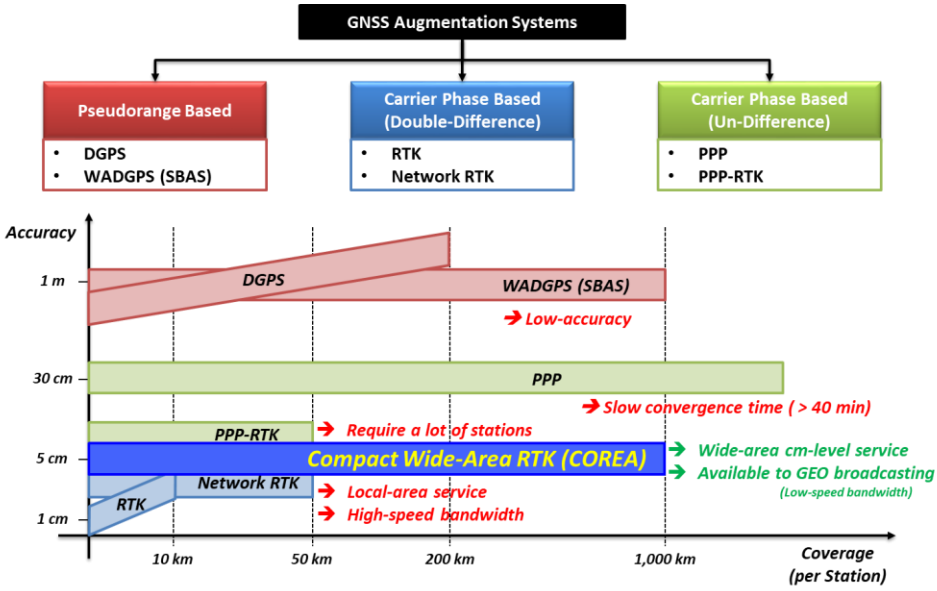

Figure 2.20 Performance comparison of GNSS augmentation systems (Coverage per station versus position accuracy)

Table 2.4 Summary of pros and cons of GNSS augmentation systems

System	Pseudorange	OSR (Observation Space Representation)			SSR (State Space Representation)		OSR+SSR
	SBAS	RTK	Network RTK	WARTK (Europe)	PPP	PPP-RTK (Japan, CLAS)	Compact Wide-Area RTK (Proposed)
Position Accuracy	0.5~1 m	2~5 cm	5~10 cm	10~30 cm	10~30 cm	5~10 cm	5~10 cm
Time-To-First-Fix (Convergence Time)	Instantly	< 10 sec	~ 1 min	5~10 min	30~60 min	~ 1 min	~ 1 min
Service Coverage per Network	Nationwide / Continental	Local	Regional	Nationwide / Continental	Global	Nationwide	Nationwide / Continental
Baseline Distance between Stations	200~1,000 km	< 10 km	50~70 km	200~1,000 km	-	10~50 km	200~1,000 km
Number of Stations (for Korea)	5~7	300	80~100	5~7	-	100~300	5~7
Required Bandwidth	Low (250 bps)	Medium (~1,200 bps)	High (~2,000 bps)	Very-High	Low	High (2,000 bps)	Low (250 bps)
Correction Types	• SV Orbit • SV Clock • Ionosphere	• RS Observations	• RS Observations • MAC	• RS Observations • SV Orbit • Ionosphere	• SV Orbit • SV Clock	• SV Orbit • SV Clock • Code/Phase Bias • Ionosphere • Troposphere	• SV Orbit • SV Clock + Code/Phase Bias • Troposphere

Intentionally Blank Page

CHAPTER 3. COMPACT WIDE-AREA RTK SYSTEM ARCHITECTURE

3.1 Compact Wide-Area RTK Architecture

The Compact Wide-Area RTK (Compact WARTK) is a new concept of GNSS augmentation system for centimeter-level positioning services in continental scale through GEO satellite broadcasting. The compact WARTK system provides vector-type corrections for each error component instead of calculating scalar-type corrections for each reference station, as in network RTK. As shown in Figure 3.1, the scalar-type corrections of network RTK are not sufficiently accurate for the user beyond the baseline distance of 70 km because the GNSS spatial decorrelation error occurs as the distance between the reference station and the user increases. On the other hands, as shown in Figure 3.2, the vector-type corrections of each error element have the advantage of expanding service coverage. It is possible to interpolate the corrections properly at the user location. This concept is the similar as the coverage of the DGPS that provides scalar-type pseudorange corrections was expanded through the vector-type corrections of the WADGPS or SBAS [35], [60]. Through this strategy, the compact WARTK system can achieve centimeter-level services using a few number of reference stations whose baseline distances are 200~1,000 km. In other words, it is possible to expand the network RTK coverage to continental scale using a similar number of reference stations as legacy SBAS.

Furthermore, the vector-type corrections for each error component can be reduced message amounts through scheduling based on error characteristics. Therefore, it is available to broadcast the compact WARTK corrections over the continent via a GEO satellite with very low-speed datalink of 250 bps like legacy SBAS.

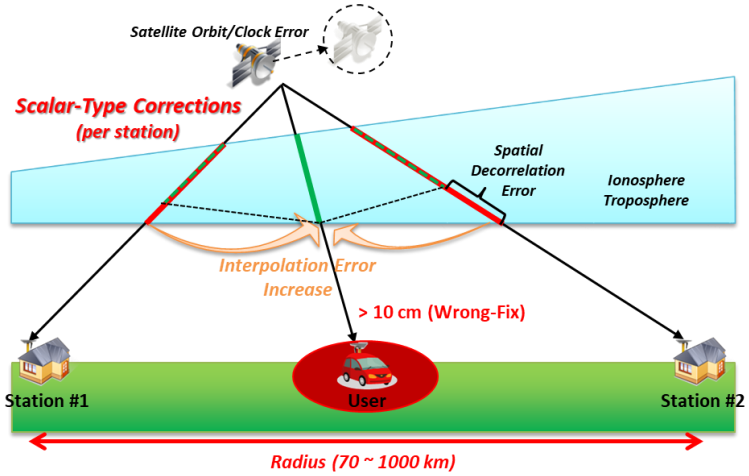

Figure 3.1 Concept of scalar-type corrections in wide-area network

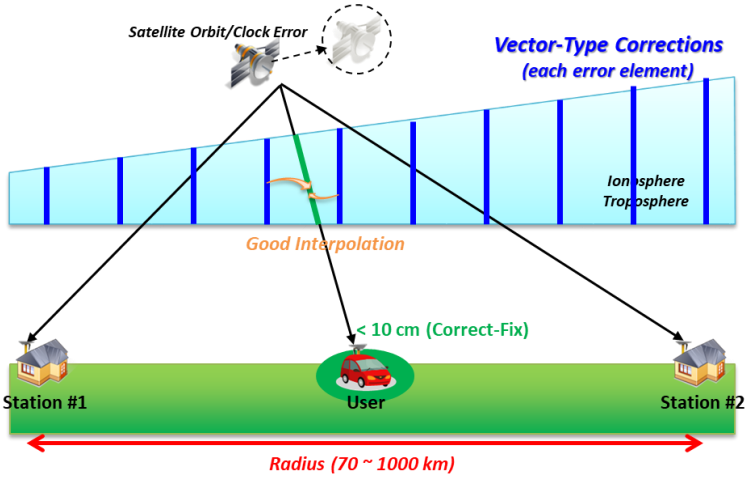

Figure 3.2 Concept of vector-type corrections in wide-area network

Figure 3.3 represents the conceptual figure of compact WARTK system, and Figure 3.4 shows the block diagram of the system architecture. The system consists of a number of WARTK Reference Stations (WRS), a WARTK Processing Facility (WPF), a WARTK Uplink Facility (WUF) with GEO satellite, and users. The system infrastructure is very similar to legacy SBAS. This system has the advantage of utilizing the infrastructure of meter-level SBAS to enable centimeter-level positioning. This means that the number of reference stations required for nationwide centimeter-level services can be dramatically reduced compared to network RTK, as shown in Figure 3.5. In fact, only 5~7 reference stations are necessary for 1,000 km radius service area.

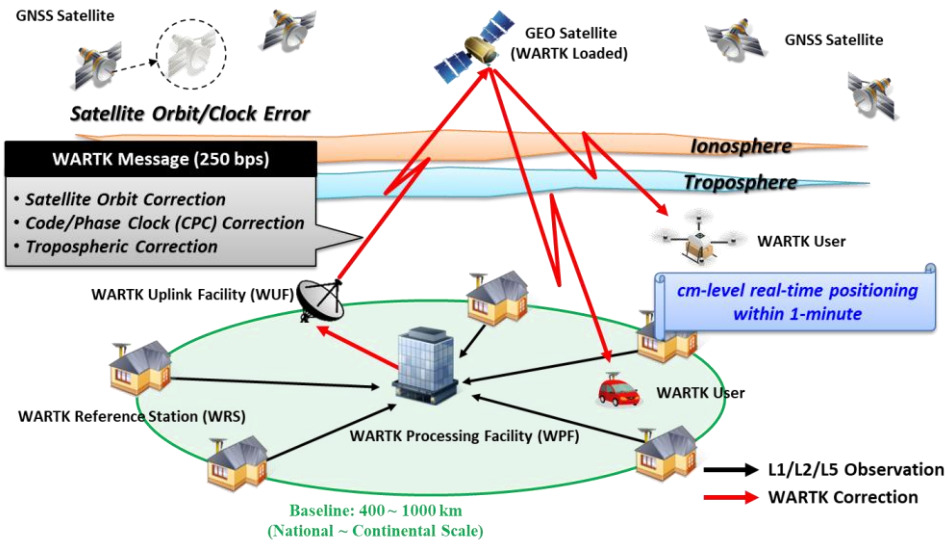

Figure 3.3 Conceptual figure of compact wide-area RTK system

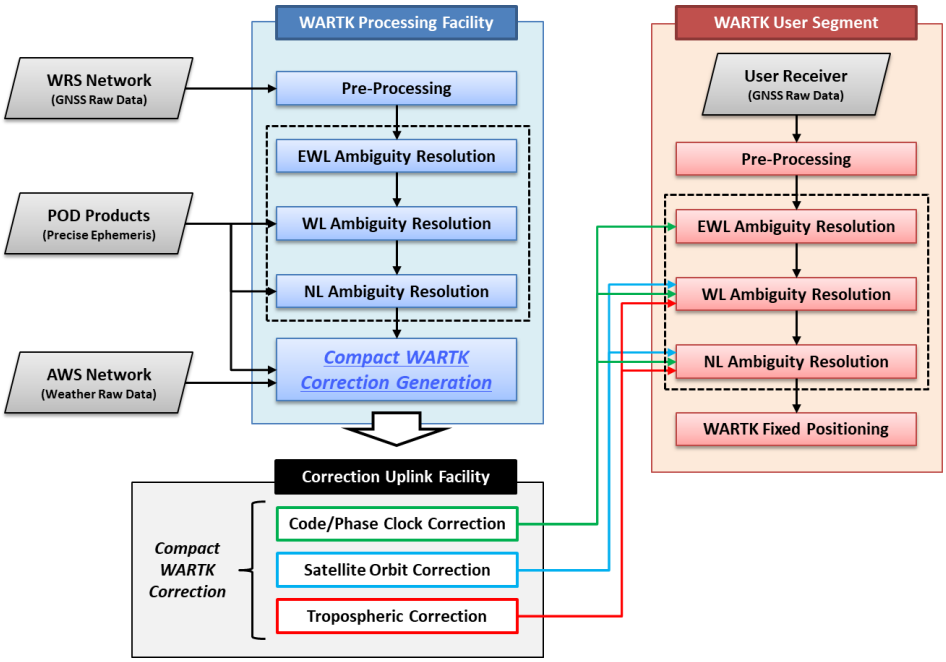

Figure 3.4 Block diagram of compact wide-area RTK system architecture

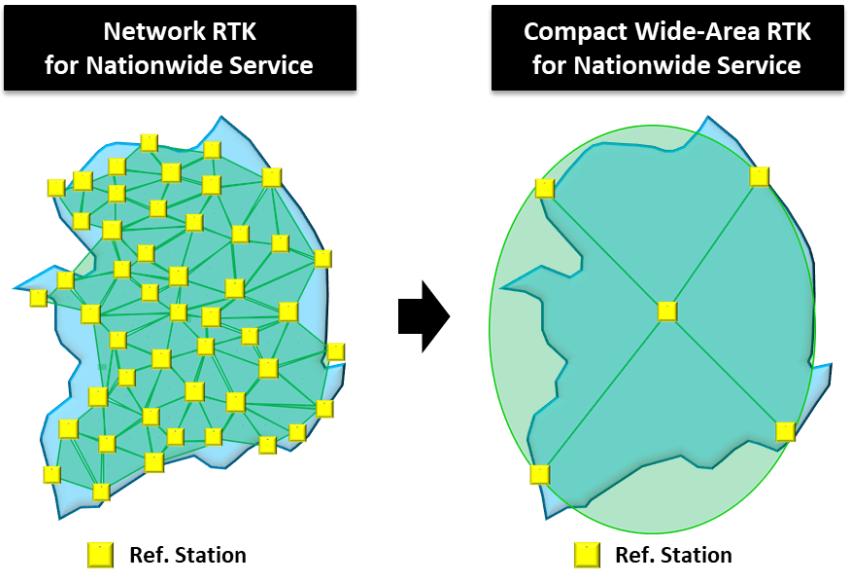

Figure 3.5 The number of reference stations required for nationwide centimeter-level services

The overall process and function of each module is summarized as follows:

1. The WRSs, which are scattered in service area within baseline distance about 1,000 km, collect multi-frequency pseudorange and carrier-phase measurements from all satellites in the field of view. GNSS measurements taken at each WRS are sent to the WPF.

2. The WPF produces three types of high-precision corrections: satellite orbit corrections, satellite code and phase clock (CPC) corrections, and tropospheric corrections. Since these corrections are generated by using carrier-phase observations, the WPF has the function of an integer ambiguity resolution and validation. Finally, the WPF transmits the corrections as the message designed at 250 bps to the WUF.

3. The WUF uploads the message upon SBAS-like signals, and broadcast to users within the service area via GEO satellite. It is also possible to broadcast through other convenient ground-based communication links such as internet, LTE, 5G, or etc.

4. Users who receive the multi-GNSS multi-frequency observations and the compact WARTK corrections correctly solve their double-differenced integer ambiguity within 1 minute. After fixing integer ambiguity, users can calculate centimeter-level position in real-time.

The detailed function of WRS, WPF, and user are described in the following subsections.

3.1.1 WARTK Reference Station (WRS)

The WRS are scattered at distance between about 200~1,000 km within target service network. The WRS are installed in an environment where there is no multipath of a concrete fixed antenna in accordance with the installation guidelines [67]. Figure 3.6 shows an example of WRS site environment managed by National Geodetic Survey (NGS) of USA. The location of each WRS is pre-surveyed at a centimeter-level accuracy, and the horizontal velocity of surveyed position due to motion of Earth's plates, which is called GPS time series, should be continuously monitored [68]. Each WRS is equipped with a multi-frequency GNSS receiver including a highly stable rubidium clock. This stable oscillator enables the precise estimation of the receiver clock offset [14].

The function of the WRS is to collect multi-frequency GNSS measurements from all tracking satellites in the field of view whose mask angle of five degrees. The receiver of WRS collects pseudorange and carrier-phase measurements with 1-second intervals. In addition, Doppler, C/N0, and navigation messages are collected. The observed data from all WRS is transmit to the WPF via communication links such as internet.

Figure 3.6 An example of WRS site environments
(GRTN, CORS site managed by NGS)

Unlike the network RTK and PPP-RTK system, which requires densely installed reference stations at about 10~50 km interval for nationwide service, the compact WARTK system requires only a few reference stations at about 200~1,000 km intervals likewise the legacy SBAS. In this thesis, six CORS sites in USA, which is managed by the NGS of National Oceanic and Atmospheric Administration (NOAA), are selected for WRS of compact WARTK system for preliminary test. There locations are shown in Figure 3.7, and all the stations have a Trimble NetR9 receiver connected with a Trimble zephyr antenna. Table 3.1 summarizes the location of antenna reference point of each WRS, and Table 3.2 lists the types of receiver and antenna.

Table 3.1 Location of antenna reference point of selected WRS in USA

No.	*Name*	*State*	*Latitude (deg)*	*Longitude (deg)*	*Height (m)*
1	GRTN	OH	38.86 N	83.88 W	252.0 m
2	KNTN	OH	40.63 N	83.61 W	264.8 m
3	NCSO	NC	35.39 N	76.33 W	-31.3 m
4	NCFF	NC	33.96 N	77.94 W	-30.6 m
5	ARMO	AR	33.59 N	91.81 W	52.7 m
6	WINL	WI	43.84 N	90.14 W	243.7 m

**Coordinates: IGS08 (Epoch 2005.0)*

Table 3.2 Receiver and antenna type of selected WRS in USA

No.	*Name*	*State*	*Receiver Type*	*Antenna Type*
1	GRTN	OH	TRIMBLE NETR9 v5.22	TRM59800.00 SCIS
2	KNTN	OH	TRIMBLE NETR9 v5.37	TRM59900.00 SCIS
3	NCSO	NC	TRIMBLE NETR9 v5.22	TRM57971.00 TZGD
4	NCFF	NC	TRIMBLE NETR9 v5.37	TRM55971.00 TZGD
5	ARMO	AR	TRIMBLE NETR9 v5.33	TRM57971.00 NONE
6	WINL	WI	TRIMBLE NETR9 v5.22	TRM57971.00 NONE

**Reference date: 2019.01.24*

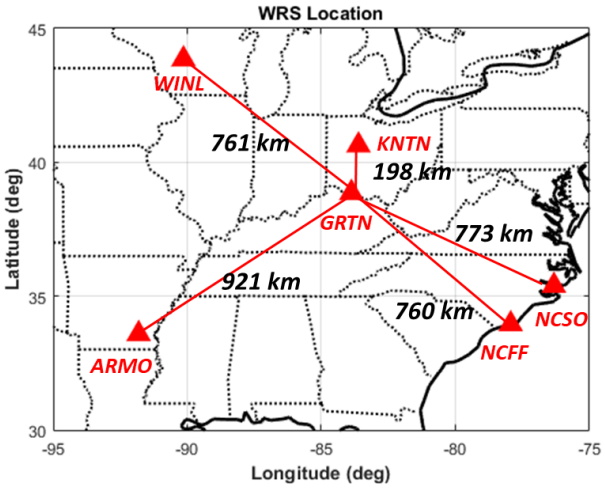

Figure 3.7 Locations of selected WRS in USA and its distance from GRTN

3.1.2 WARTK Processing Facility (WPF)

The primary function of the WPF is to generate high-precision corrections using collected GNSS measurements from WRSs. Another major function of the WPF is to monitor the integrity of the corrections. As shown the architecture of Figure 3.4, the WPF process is divided into a pre-processing module, an ambiguity resolution and validation module, and correction generation module. The WPF also sends the produced corrections to the WUF.

1) Pre-Processing Module

The pre-processing module includes anomaly detection and quality monitoring for collected raw measurements from WRSs. This module is very important because the WPF must insure that all corrections are reliable for user safety. If anomalies in measurements are not correctly detected and eliminated, the WPF may generate wrong corrections that threatens user safety and degrade accuracy. The pre-processing module also includes noise and multipath mitigation process. The function of pre-processing module is summarized as follows:

- Reference Station Integrity Monitoring (RSIM)

This function includes signal quality monitoring (SQM), data quality monitoring (DQM), and measurement quality monitoring (MQM) [69], [70]. The SQM monitor the quality of the satellite signal itself, signal power, and code-carrier divergence. The SQM uses multiple correlators to monitor for signal deformation [71]. The DQM checks the validity of the broadcast ephemeris and clock data for each satellite. The MQM detects anomalies of sudden step or impulsive errors in pseudorange and carrier-phase measurements. The MQM includes the receiver lock time check,

carrier-acceleration-step test, and carrier-smoothed code innovation test. Figure 3.8 shows an example of the RSIM for Ground-Based Augmentation System (GBAS) in USA. The augmentation system to ensure user safety should include the RSIM functions like GBAS and SBAS.

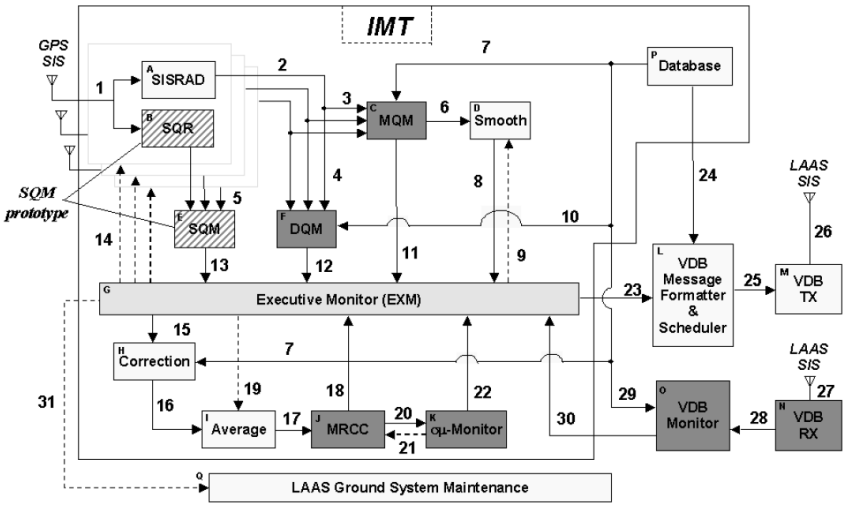

Figure 3.8 An example of reference station integrity monitoring of GBAS in USA [69]

- Cycle Slip Detection and Compensation

A cycle slip, which is an instantaneous jump of an integer number of a cycle on carrier-phase measurements, occurs unexpectedly when the receiver's phase-locked loop (PLL) has a loss of lock during a temporary signal blockage or an ionospheric scintillation [72]–[74]. The cycle slip must be handled at the pre-processing stage since it induces an error with an unpredictable range, which can seriously affect the quality of high-precision corrections and user position solution [75]–[77]. We propose a new algorithm based on two independent and complementary carrier-

phase combinations to detect and compensate dual-frequency cycle slip. The proposed method can successfully detect all cycle slip pairs even severe ionospheric storm conditions, and is not affected by pseudorange multipath. Figure 3.9 shows the overall block diagram of algorithms and Figure 3.10 represents an example result of cycle-slip detection. The detailed algorithm describes in the following paper [78].

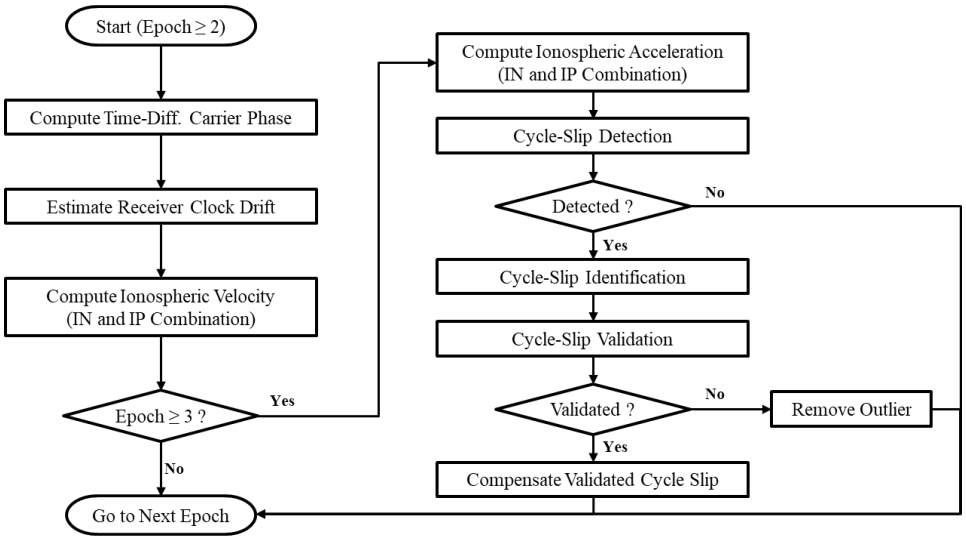

Figure 3.9 Block diagram of cycle slip detection and compensation [78]

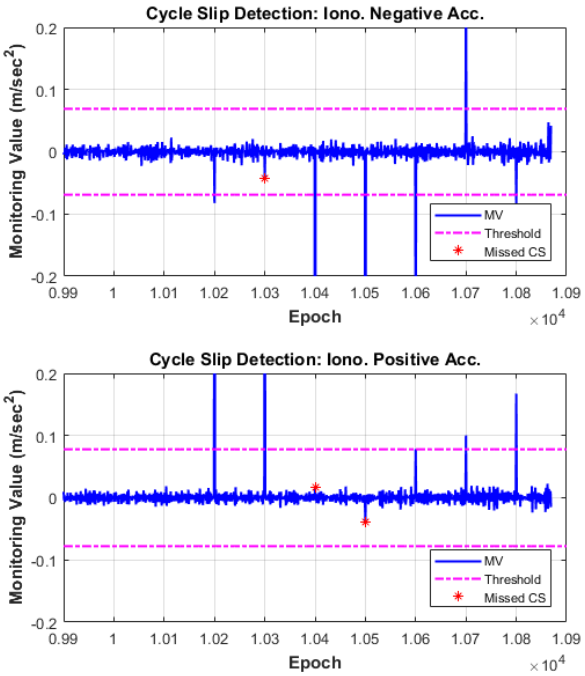

Figure 3.10 Cycle-slip detection results of proposed method [78]

- Code Noise and Multi-Path (CNMP) Processing

Pseudorange measurements of WRS have a meter-level code noise and multipath (CNMP) that is one of the critical error sources on augmentation system. The purpose of CNMP processing is to greatly reduce the noise and multipath of measurements and provide confidence-level for bounding error distribution. The CNMP algorithm contains three major components; dual-frequency smoothing, mean filter, and CNMP standard deviation processing [79], [80]. The purpose of dual-frequency smoothing so-called divergence-free Hatch filter is to suppress the pseudorange noise using the variation of precise carrier phase while mitigating the ionospheric divergence [36], [81]–[83]. The mean filter processing estimates the

long-term multipath through computing the average bias of carrier-phase ambiguity by lag-filter. Finally, we can obtain the multipath-corrected pseudorange. The CNMP standard deviation processing provides the confidence term for residual error in the multipath-corrected pseudorange. The WAAS already developed the CNMP standard deviation function considered the threat models [79], [80], and this study applies the WAAS CNMP model. Figure 3.11 represents the residual error and standard deviation of L1 multipath-corrected pseudorange for signal tracking time (or smoothing time).

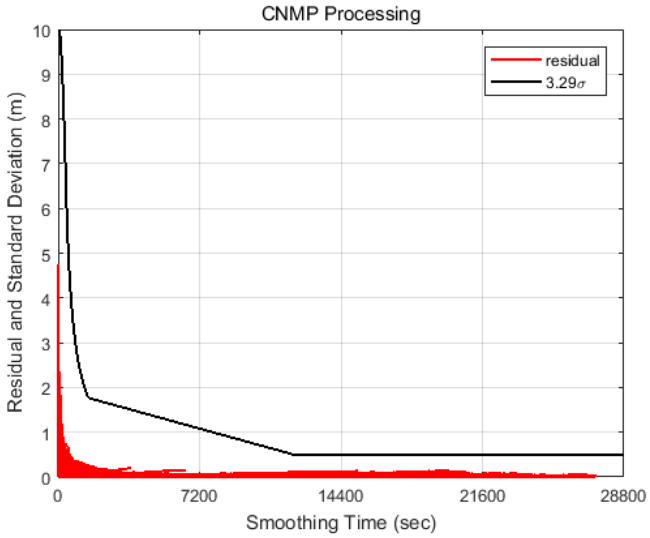

Figure 3.11 Residual error and standard deviation of L1 smoothed pseudorange by WAAS CNMP processing

2) Ambiguity Resolution and Validation Module

In order to generate high-precision corrections using carrier-phase observations, the integer ambiguity of carrier phase must be correctly resolved and validated. The WPF applies a new TCAR algorithm based on ionospheric-free combinations of multi-frequency signals. This method consists of three steps: extra-wide-lane (EWL) ambiguity resolution, wide-lane (WL) ambiguity resolution, and narrow-lane (NL) ambiguity resolution.

Unlike the traditional TCAR method used in WARTK system on Europe [19], the proposed TCAR uses geometry-based ionospheric-free (GBIF) linear combinations that includes satellite orbit error and tropospheric delay error. Therefore, the WPF required real-time precise ephemeris products from precise orbit determination (POD) process for reducing satellite orbit error. The WPF applied our own real-time POD products which have similar accuracy of the ultra-rapid products of the International GNSS Service (IGS) [84]. These POD products are also used to generate satellite orbit corrections. In the WL and NL process which utilize GBIF combinations, the WPF estimates the zenith tropospheric delay of each WRS and the double-differenced integer ambiguity together using the Kalman filter. The precise tropospheric delay estimated by the filter is used to generate tropospheric corrections. The detailed algorithms of ambiguity resolution and validation will be discussed in section 3.2.

3) Correction Generation Module

The correction generation module is a major function of the WPF. The WPF produces the high-precision corrections using carrier-phase measurements after integer ambiguity is correctly determined. The WPF has three correction generation process for satellite orbit corrections, satellite CPC corrections, and tropospheric corrections. The satellite orbit corrections are generated based on the real-time POD product to reduce three-dimensional orbit errors for each satellite. The satellite CPC corrections for eliminating satellite clock and hardware bias of each satellite are generated using multiple stations together for robustness on communication failures. The tropospheric corrections for zenith tropospheric delay are modelled using the carrier-phase observations and weather data together based on the spherical harmonics function. The weather data obtain from the automatic weather stations (AWS). The ionospheric corrections does not produced since the new TCAR methods for the WPF and users applies ionosphere-free linear combinations. The more detailed description of compact WARTK corrections will be discussed in section 3.3.

3.1.3 WARTK User

The user process is similar to the WPF process as shown in Figure 3.4. The user collects pseudorange and carrier-phase observations and ephemeris data for all GNSS satellites in field of view. In addition, the user receive the compact WARTK corrections broadcasted via GEO satellite or other communication links. The anomalies of raw observed data are detected and removed in the pre-processing stage. After the pre-processing, the screened observation data is corrected by the compact WARTK corrections. Next, the double-difference integer ambiguity included in user carrier-phase observation resolves through the similar TCAR method of the WPF. The difference from the WPF algorithms is that the user does not known its location; therefore, the navigation Kalman filter has the estimated states of position, velocity, and acceleration. Finally, the high-accuracy position are calculated after correctly solved the integer ambiguity. The sub-meter level position can obtain immediately, and the centimeter-level position can obtain after fixing NL ambiguity. The detailed algorithms of user will be discussed in Chapter 6.

The user who would the greatest benefit from the compact WARTK system has a receiver tracking triple-frequency signals. Dual-frequency users can also calculate the centimeter-level position using the compact WARTK corrections, but have longer convergence time than triple-frequency users.

3.2 Ambiguity Resolution and Validation Algorithms of Compact Wide-Area RTK System

This section introduces the resolution and validation algorithms of double-differenced integer ambiguity for WPF and users. The WPF and user of compact WARTK system applies a new TCAR algorithms for suitable of wide-area networks.

The TCAR is basically a method of fixing integer ambiguity in order of long wavelength using linear combinations of triple-frequency signals. However, the traditional TCAR method which applies geometry-free ionospheric-based combinations cannot be used to estimate integer ambiguity if the baseline distance between receivers are more than 10 km due to the ionospheric residual error. Therefore, the WARTK system on Europe requires the additional precise ionospheric corrections for ambiguity resolution of users whose baseline length from stations is more than 10 km [19].

On the other hand, the proposed TCAR method of compact WARTK system applies GBIF combinations to completely eliminate the ionospheric delay error. Without considering the ionospheric delay with the largest GNSS error sources, the integer ambiguity can be resolved in the wide-area networks regardless of the distance between the receivers. The Kalman filter of the new TCAR method estimates the tropospheric delay of each station in WPF process, and estimate the position, velocity, and acceleration in user process. This method is also an extended version of the dual-frequency medium-baseline RTK [4] to triple-frequency WARTK .

3.2.1 Basic Theory of Ambiguity Resolution and Validation

This subsection summarizes the basic theory of ambiguity resolution and validation. Figure 3.12 shows the four steps of integer ambiguity resolution and validation [85]. Generally, every carrier-phase based GNSS model can be formulated in the mixed integer linearized form as following equation where $\bar{y}$ is the GNSS measurements, $\bar{a}$ is the integer ambiguities, $\bar{b}$ represents the real-valued parameters such as position coordinates and tropospheric delay. A and B are design matrices of the GNSS model. $\bar{v}$ is the Gaussian random noise vector with variance-covariance matrix $Q_{\bar{y}\bar{y}}$.

$$\bar{y} = A\bar{a} + B\bar{b} + \bar{v} \qquad \bar{v} \sim N(0, Q_{\bar{y}\bar{y}}) \tag{3.1}$$

In the first step, we estimate the float solutions, discarding the integer nature of ambiguity. Typical estimation techniques include least-squares, reculsive least-squares, and Kalman filtering. The obtained float solutions and their variance-covariance matrix can be expressed as follows.

$$\begin{bmatrix} \hat{a} \\ \hat{b} \end{bmatrix}, \begin{bmatrix} Q_{\hat{a}\hat{a}} & Q_{\hat{a}\hat{b}} \\ Q_{\hat{b}\hat{a}} & Q_{\hat{b}\hat{b}} \end{bmatrix} \tag{3.2}$$

In the second step, the real-valued float ambiguities are mapped to an integer space taking into account the constraints. Among the various integer mapping methods, the LAMBDA (Least-squares AMBiguity Decorrelation Adjustment) method applying the integer least-squares principle is the best because it has the largest success-rate [86]–[88].

$$\breve{a} = I(\hat{a}), \quad I : \mathbb{R}^n \mapsto \mathbb{Z}^n \qquad \hat{a} \in \mathbb{R}^n, \ \breve{a} \in \mathbb{Z}^n \tag{3.3}$$

The third step is the integer ambiguity validation test. The purpose of this step is to provide confidence in the integer outcomes of ambiguity resolution. The integer solution from step 2 is accepted when satisfying the conditions of validation test. Several such tests have been studied and typically, the threshold test, ratio test, and difference test are conducted for ambiguity validation [85], [89]–[94].

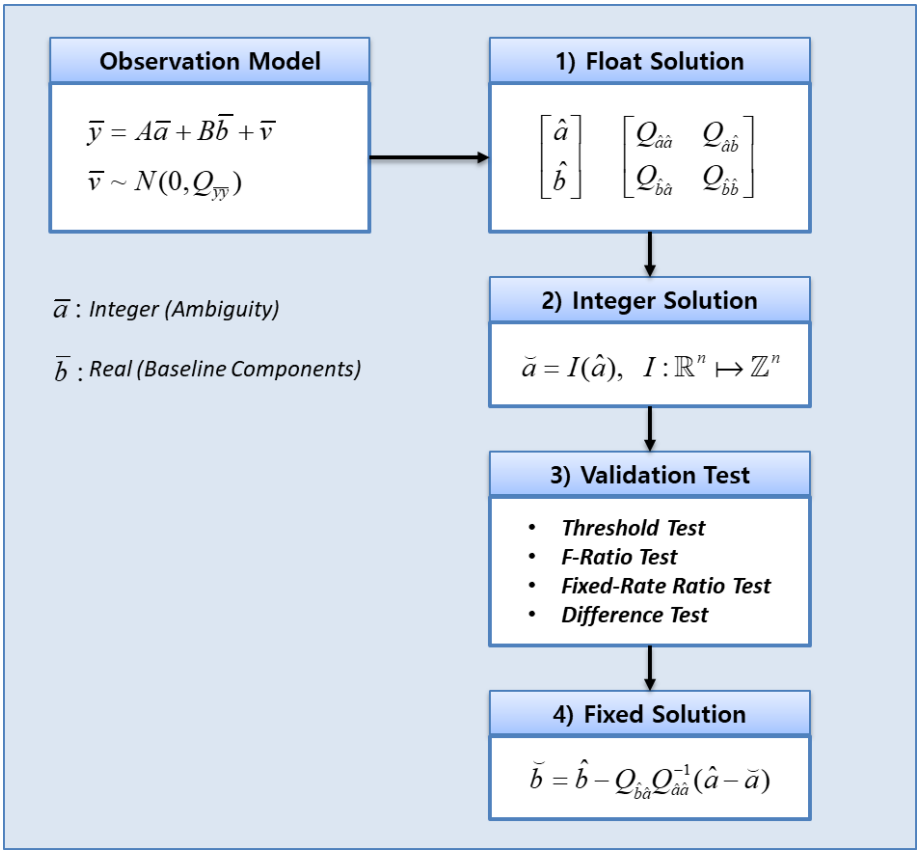

Figure 3.12 Basic processing of ambiguity resolution and validation

The integer solution that passes the threshold test based on chi-square distribution is considered as a candidate solution. The ratio test or difference test are conducted to distinguish between the best and the second best of the candidate solutions in the search space. In this thesis, two tests are used to verify the integer ambiguity: F-ratio test based on observation residuals [91], [94] and fixed-rate ratio test based on ambiguity residuals [89], [90]. The threshold of the F-ratio test is set to 1.5 empirically. The threshold of the fixed-rate ratio test is set through the look-up tables for a given fixed failure rate. Figure 3.13 shows an example of threshold c-value by look up tables of fixed-rate ratio test when a number of visible satellites is 9 and fixed failure rate is 0.1%.

- F-ratio test

$$\frac{\Omega_{2nd}}{\Omega_{1st}} > k = 1.5 \qquad where \;\; \Omega_i = \left\| \bar{y} - A\breve{a}_i - B\breve{b}_i \right\|^2_{Q_{\bar{y}\bar{y}}} \tag{3.4}$$

- Fixed-rate ratio test

$$\frac{R_{2nd}}{R_{1st}} > c = f(P_{f,\,fixed}) \quad where \;\; R_i = \left\| \hat{a} - \breve{a}_i \right\|^2_{Q_{\hat{a}\hat{a}}} \tag{3.5}$$

In the final step, once the best integer solution $\breve{a}$ is accepted, the fixed solution can be calculated from the re-adjustment of the float solution as considering of their correlation.

$$\breve{b} = \hat{b} - Q_{\hat{b}\hat{a}} Q^{-1}_{\hat{a}\hat{a}} (\hat{a} - \breve{a}) \tag{3.6}$$

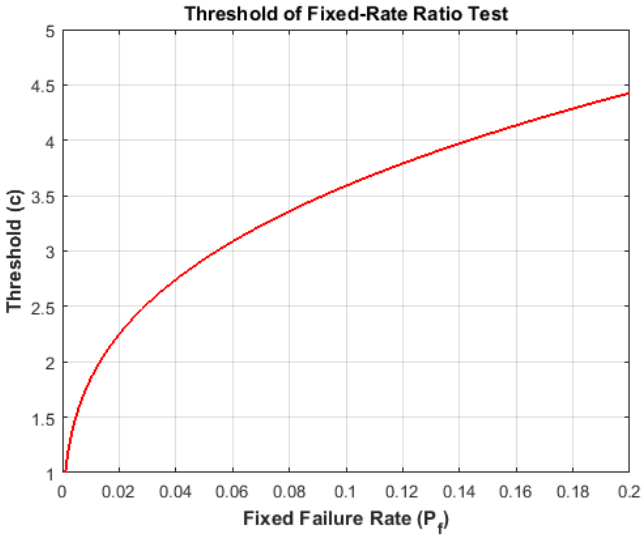

Figure 3.13 Threshold of fixed-rate ratio test by look-up table (n = 9, Pf,fixed = 0.1%)

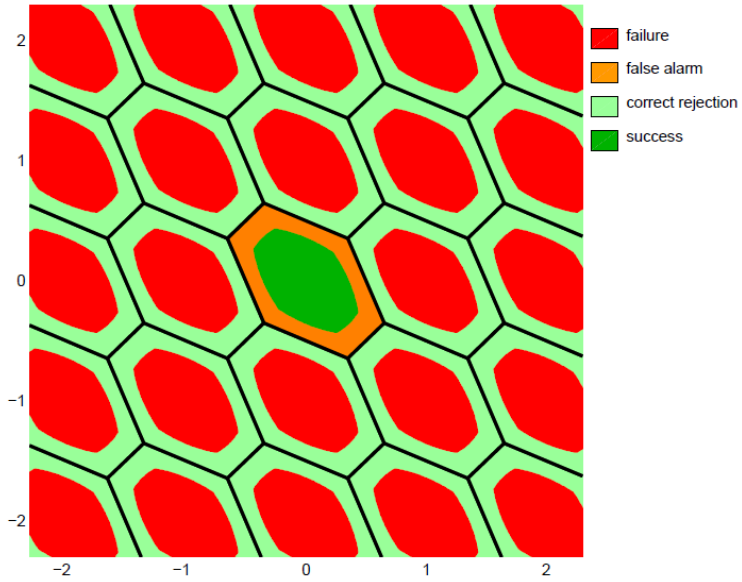

Figure 3.14 Acceptance regions of LAMBDA with ratio test [85]

Figure 3.14 represents the two-dimensional acceptance region of LAMBDA method with ratio test. The green areas are the regions of correct acceptance (success rate), and the red areas mean wrong acceptance (failure rate). The orange and light green areas are undecided regions that is not fixed to integer. The ambiguity performance is assessed based on the corresponding probabilities of success (s), failure (f), and undecided (u) [85], [90]:

$$\begin{aligned} P_s &= P\left(\breve{a} = a\right) \\ P_f &= P\left(\breve{a} = z \neq a\right) \\ P_u &= P\left(\breve{a} = \hat{a}\right) \end{aligned} \tag{3.7}$$

There is important performance indicator called success-fix (sf) rate that means the probability that the ambiguity is correct if fixed by the validation test.

$$P_{sf} = \frac{P_s}{P_s + P_f} \tag{3.8}$$

Another useful performance indicator is the ambiguity dilution of precision (ADOP) which one can expect to have a successful validation of the ambiguities. The ADOP can be simply calculated from the determinant of variance-covariance matrix of ambiguity estimation. If the ADOP is sufficiently smaller than one cycle, successful validation is expected [95], [96].

$$ADOP = \sqrt{\det Q_{\hat{a}\hat{a}}}^{1/n} \tag{3.9}$$

3.2.2 A New Ambiguity Resolution Algorithms for Multi-Frequency Signals

Because of benefits of improving reliability and availability performance compared to the dual-frequency signals, the ambiguity resolution methods using triple-frequency have been intensively studied in the past decades [97]–[99]. Especially, many algorithms suggested the triple-frequency RTK for long-baseline distances that overcome the limitations of traditional TCAR method [100]–[102]. Among them, the compact WARTK system uses the method based on the geometry-based ionospheric-free (GBIF) combinations in order to completely eliminate the effects on ionospheric delay while expanding the service area. The overall structure of algorithm is similar with Jia's method designed on BeiDou triple-frequency signals [102]; however, the new TCAR method can be used on both dual- and triple-frequency signals unlike Jia's method which cannot be used for dual-frequency signals. Furthermore, the proposed method has improved WL ambiguity resolution performance over the method suggested by Jia.

In order to demonstrate the new TCAR method, this subsection briefly reviews the typical linear combinations of multi-frequency signals. Any geometry-based linear combination of L1, L2, and L5 signals which preserves the integer nature of the ambiguity can be formulated as following equations [97]–[99], [103]. ρ_x and ϕ_x are pseudorange and carrier phase measurements on frequency f_x $(x = 1, 2, 5)$. The linear-combination coefficients l, m, n for pseudorange, and i, j, k for carrier phase are all integers.

$$\rho_{(l,m,n)} = \frac{l \cdot f_1 \cdot \rho_1 + m \cdot f_2 \cdot \rho_2 + n \cdot f_5 \cdot \rho_5}{l \cdot f_1 + m \cdot f_2 + n \cdot f_5} \quad \textbf{(3.10)}$$

$$\phi_{(i,j,k)} = \frac{i \cdot f_1 \cdot \phi_1 + j \cdot f_2 \cdot \phi_2 + k \cdot f_5 \cdot \phi_5}{i \cdot f_1 + j \cdot f_2 + k \cdot f_5} \quad \textbf{(3.11)}$$

The geometry-based linear combinations of double-differenced pseudorange and carrier-phase measurements can be expresses as follow equations. $\Delta\nabla$ indicates the double-difference operator.

$$\Delta\nabla\rho_{(l,m,n)} = \Delta\nabla d + \Delta\nabla T + \beta_{(l,m,n)}\Delta\nabla I + \varepsilon_{\Delta\nabla\rho_{(l,m,n)}} \quad \textbf{(3.12)}$$

$$\Delta\nabla\phi_{(i,j,k)} = \Delta\nabla d + \Delta\nabla T - \beta_{(i,j,k)}\Delta\nabla I + \lambda_{(i,j,k)}\Delta\nabla N_{(i,j,k)} + \varepsilon_{\Delta\nabla\phi_{(i,j,k)}} \quad \textbf{(3.13)}$$

The combined measurement has the virtual combined wavelength

$$\lambda_{(i,j,k)} = \frac{c}{i \cdot f_1 + j \cdot f_2 + k \cdot f_5} \qquad c : speed\ of\ light \quad \textbf{(3.14)}$$

with integer ambiguity

$$N_{(i,j,k)} = i \cdot N_1 + j \cdot N_2 + k \cdot N_5 \quad \textbf{(3.15)}$$

and ionospheric scale factor (ISF).

$$\beta_{(i,j,k)} = \frac{i/f_1 + j/f_2 + k/f_5}{i \cdot f_1 + j \cdot f_2 + k \cdot f_5} \cdot f_1^2 \quad \textbf{(3.16)}$$

Assuming that the measured noises of three frequency signals are independent and has same precision, the standard deviation for pseudorange and carrier phase are given as following equations. μ indicates the noise scale factor (NSF).

$$\sigma_{\rho_{(l,m,n)}} \simeq \underbrace{\frac{\sqrt{(l\cdot f_1)^2+(m\cdot f_2)^2+(n\cdot f_5)^2}}{l\cdot f_1+m\cdot f_2+n\cdot f_5}}_{=\mu_{(l,m,n)}}\sigma_\rho \quad \left(\because \sigma_\rho=\sigma_{\rho_1}=\sigma_{\rho_2}=\sigma_{\rho_5}\right) \tag{3.17}$$

$$\sigma_{\phi_{(i,j,k)}} \simeq \underbrace{\frac{\sqrt{(i\cdot f_1)^2+(j\cdot f_2)^2+(k\cdot f_5)^2}}{i\cdot f_1+j\cdot f_2+k\cdot f_5}}_{=\mu_{(i,j,k)}}\sigma_\phi \quad \left(\because \sigma_\phi=\sigma_{\phi_1}=\sigma_{\phi_2}=\sigma_{\phi_5}\right) \tag{3.18}$$

In case of GPS, all three signal frequencies L1, L2, and L5 are derived from the same base frequency $f_0 = 10.23 MHz$; that is, $f_1 = 154 f_0$ (1575.42 MHz), $f_2 = 120 f_0$ (1227.6 MHz), and $f_5 = 115 f_0$ (1176.45 MHz) [103].

The proposed TCAR method is designed based on geometry-based linear combinations according to the above definition. Generally, the combinations with longer wavelength relative to the noise level in cycle, their integer ambiguity can be correctly fixed easier. Thus, the proposed TCAR method determines the integer ambiguity over three stages (EWL, WL, and NL) sequentially from linear combinations with long wavelengths likewise traditional TCAR method. Figure 3.15 shows the block diagram of proposed TCAR method based on GPS triple-frequency signals. Table 3.3 summarized the ionospheric-free linear combinations used in proposed TCAR method. We assume the standard deviations of double-differenced observations are $\sigma_{\Delta\nabla\rho} = 1.5 m$ and $\sigma_{\Delta\nabla\phi} = 4 mm$, respectively.

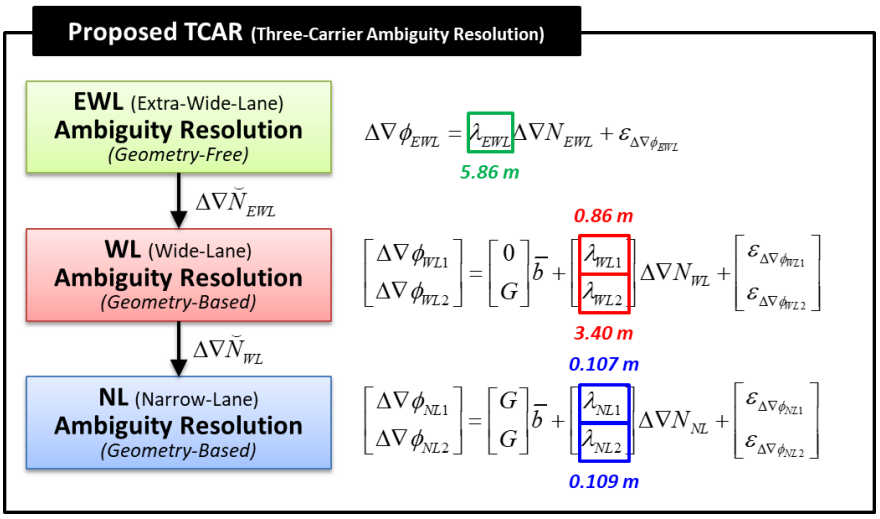

Figure 3.15 Block diagram of proposed TCAR algorithm based on GPS triple-frequency signals

Table 3.3 Linear combinations of GPS triple-frequency signals for compact wide-area RTK

Observation Combination		Error Factor		Wavelength (λ)	Noise SF (μ)		Total Noise (σ)	Ratio (σ/λ)
		Tropo	Iono		PR	CP		
CP-EWL	Melbourne-Wübbena (L2/L5)	0	0	5.86 m	0.71	33.24	1.07 m	0.18 cycle
CP-WL1	Melbourne-Wübbena (L1/L2)	0	0	0.86 m	0.71	5.74	1.07 m	1.24 cycle
CP-WL2	Wide-Lane Iono-Free (L1/L2/L5)	1	0	3.40 m	0	109.98	0.44 m	0.13 cycle
CP-NL1	Narrow-Lane Iono-Free (L1/L2)	1	0	10.7 cm	0	2.98	11.9 mm	0.11 cycle
CP-NL2	Narrow-Lane Iono-Free (L1/L5)	1	0	10.9 cm	0	2.59	10.4 mm	0.10 cycle
PR-IF*	Pseudorange Iono-Free (L1/L2)	1	0	-	2.98	-	4.47 m	-

*Required for initializing user position

$\sigma(\varepsilon_{\Delta\nabla\phi}) = 4\,mm \quad \sigma(\varepsilon_{\Delta\nabla\rho}) = 1.5\,m$

The EWL ambiguity can be easy to fix by the traditional method, while the WL and NL ambiguity resolution is still challenging issue. Therefore, the proposed method mainly discusses the WL and NL ambiguity resolution based on geometry-based ionospheric-free combinations of GPS triple-frequency signals. The details are described on follow subsections.

3.2.3 Extra-Wide-Lane (EWL) Ambiguity Resolution

The EWL ambiguity is easily resolved using Melbourne-Wübbena linear-combination by L2 and L5 frequency [102]. The Melbourne-Wübbena linear-combination that combining the NL pseudorange combination and WL carrier-phase combination is a geometry-free ionospheric-free model [4]. The EWL combination can be expressed as follows.

$$\begin{aligned}\Delta\nabla\phi_{EWL} &= \Delta\nabla\phi_{(0,1,-1)} - \Delta\nabla\rho_{(0,1,1)} \\ &= \lambda_{EWL}\Delta\nabla N_{EWL} + \varepsilon_{\Delta\nabla\phi_{EWL}}\end{aligned} \quad \textbf{(3.19)}$$

The corresponding wavelength and integer ambiguity are written as,

$$\lambda_{EWL} = \lambda_{(0,1,-1)} = 5.86\,m \quad \textbf{(3.20)}$$

$$\Delta\nabla N_{EWL} = \Delta\nabla N_{(0,1,-1)} \quad \textbf{(3.21)}$$

and the noise level of linear-combination is expressed as follow.

$$\begin{aligned}\sigma\left(\varepsilon_{\Delta\nabla\phi_{EWL}}\right) &= \sigma\left(\varepsilon_{\Delta\nabla\phi_{(0,1,-1)}} - \varepsilon_{\Delta\nabla\rho_{(0,1,1)}}\right) \\ &\approx \mu_{(0,1,1)}\cdot\sigma_{\Delta\nabla\rho} = 0.71\cdot\sigma_{\Delta\nabla\rho} \\ &= 1.07\,m\end{aligned} \quad \textbf{(3.22)}$$

The EWL combination contains the EWL integer ambiguity and pseudorange noise and multipath without any extra geometry-related error. The Kalman filter of EWL ambiguity resolution estimates the float ambiguity with pseudorange multipath modeled as the 1st order Markov process [4]. The WPF process and the user process

have same EWL filter state and model equations. Finally, the float ambiguity estimated by the filter is determined by an integer by the LAMBDA algorithm. The ratio of the noise to the wavelength $\sigma\left(\varepsilon_{\Delta\nabla\phi_{EWL}}\right)\big/\lambda_{EWL} \approx 0.18 cycle$ is sufficiently small that the EWL ambiguity is successfully resolved by the constructed EWL ambiguity resolution filter.

The ambiguity resolution performance was analyzed through simple Monte-Carlo simulation. 5000 simulations were performed for a two-dimensional environment with 8 visible satellites. Figure 3.16 shows the log-scaled ADOP performance according to epoch-history. If the ADOP is smaller than 0.1 cycle, successful resolution and validation is expected. Table 3.4 and Table 3.5 show the summary of Monte-Carlo simulation results. As a result, the success-fix rate of EWL ambiguity resolution is 100% and RMS statistics of time-to-first-fix (TTFF) is about 1.02 epochs. That means that the EWL integer ambiguity can be successfully solved on average within 2 epochs.

Table 3.4 Monte-Carlo simulation results of EWL ambiguity resolution

5000 samples	***Correct (Success, P_s)***	***Wrong (Failure, P_f)***
Fixed	100%	0%
Float (undecided, P_u)	0%	

Table 3.5 RMS statistics at the fixed time of EWL integer ambiguity

RMS statistics (5000 samples)	
Time-To-First-Fix (epoch)	1.02
Ambiguity DOP (cycle)	0.11
Position DOP	1.06

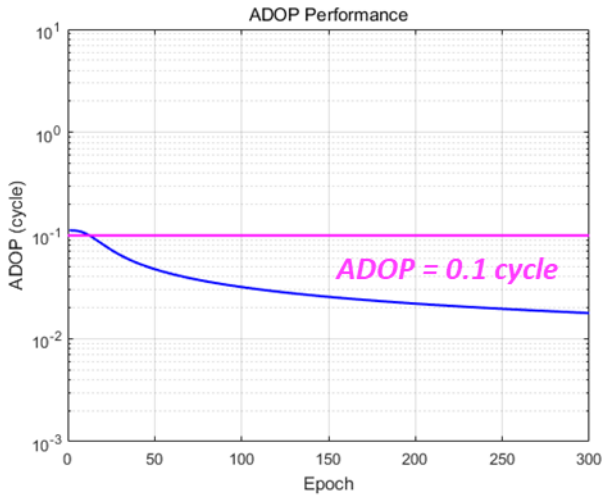

Figure 3.16 ADOP performance of EWL ambiguity resolution

3.2.4 Wide-Lane (WL) Ambiguity Resolution

When the EWL integer ambiguity is correctly resolved, the fixed EWL ambiguity $\Delta\nabla\breve{N}_{EWL}$ can be used in WL ambiguity resolution. Therefore. the WL ambiguity of L1 and L5 frequency can be re-formed using the fixed EWL ambiguity as following equation.

$$\Delta\nabla N_{(1,0,-1)} = \Delta\nabla N_{(1,-1,0)} + \Delta\nabla\breve{N}_{EWL} \quad \textbf{(3.23)}$$

Through the integer adjusting by this relationship, the L1/L2 WL carrier-phase combination $\Delta\nabla\phi_{(1,-1,0)}$ and L1/L5 WL carrier-phase combination $\Delta\nabla\phi_{(1,0,-1)}$ have the same WL integer ambiguity value $\Delta\nabla N_{WL} = \Delta\nabla N_{(1,-1,0)}$ with different wavelengths.

$$\begin{aligned}\Delta\nabla\phi_{WL(1,2)} &= \Delta\nabla\phi_{(1,-1,0)} \\ &= \Delta\nabla d + \Delta\nabla T - \beta_{(1,-1,0)}\Delta\nabla I + \lambda_{(1,-1,0)}\Delta\nabla N_{WL} + \varepsilon_{\Delta\nabla\phi_{(1,-1,0)}}\end{aligned} \quad \textbf{(3.24)}$$

$$\begin{aligned}\Delta\nabla\phi_{WL(1,5)} &= \Delta\nabla\phi_{(1,0,-1)} - \lambda_{(1,0,-1)}\Delta\nabla\breve{N}_{(0,1,-1)} \\ &= \Delta\nabla d + \Delta\nabla T - \beta_{(1,0,-1)}\Delta\nabla I + \lambda_{(1,0,-1)}\Delta\nabla N_{WL} + \varepsilon_{\Delta\nabla\phi_{(1,0,-1)}}\end{aligned} \quad \textbf{(3.25)}$$

In order to completely eliminate the ionospheric delay, the wide-lane ionospheric-free (WLIF) combination is constructed by linear combination of equation (3.24) and (3.25). The a_1 and a_2 are combination coefficients that satisfy $a_1 + a_2 = 1$ for retaining geometry terms and $a_1\beta_{(1,-1,0)} + a_2\beta_{(1,0,-1)} = 0$ for eliminating ionospheric delay term [102].

$$\Delta\nabla\phi_{WL-IF} = a_1 \cdot \Delta\nabla\phi_{WL(1,2)} + a_2 \cdot \Delta\nabla\phi_{WL(1,5)} \quad \textbf{(3.26)}$$

The values of combination coefficient are computed as follows.

$$a_1 = \frac{-\beta_{(1,0,-1)}}{\beta_{(1,-1,0)} - \beta_{(1,0,-1)}} = \frac{f_2}{f_2 - f_5} \quad \textbf{(3.27)}$$

$$a_2 = \frac{\beta_{(1,-1,0)}}{\beta_{(1,-1,0)} - \beta_{(1,0,-1)}} = -\frac{f_5}{f_2 - f_5} \quad \textbf{(3.28)}$$

The corresponding wavelength is written as,

$$\lambda_{WL-IF} = 77 \cdot \lambda_{(77,-468,391)} = 3.4\,m \tag{3.29}$$

and the noise level and the ratio of the noise to the wavelength are expressed as follows.

$$\begin{aligned} \sigma\left(\varepsilon_{\Delta\nabla\phi_{WL-IF}}\right) &= \sigma\left(a_1\varepsilon_{\Delta\nabla\phi_{(1,-1,0)}} + a_2\varepsilon_{\Delta\nabla\phi_{(1,0,-1)}}\right) \\ &= \mu_{(77,-468,391)} \cdot \sigma_{\Delta\nabla\phi} = 109.98 \cdot \sigma_{\Delta\nabla\phi} \\ &\approx 0.44\,m \end{aligned} \tag{3.30}$$

$$\frac{\sigma\left(\varepsilon_{\Delta\nabla\phi_{WL-IF}}\right)}{\lambda_{WL-IF}} \sim 0.13\,cycle \tag{3.31}$$

The carrier-phase based WLIF combinations has sufficiently small (0.13 cycle) the ratio of the noise to the wavelength; however, the rank deficiency problem is still exist because of the geometry terms. Therefore, the WL filter requires another mutually independent ionospheric-free combination to compute the initial value of states, or to solve the rank problem. The carrier-phase combination alone does not allow the construction of a new mutually independent combination. The additional ionospheric-free combination using the pseudorange observation should be considered. The new pseudorange-aided WL combination can be expressed as follow.

$$\Delta\nabla\phi_{WL-PR} = \Delta\nabla\rho_{(l,m,n)} + b_1 \cdot \Delta\nabla\phi_{WL(1,2)} + b_2 \cdot \Delta\nabla\phi_{WL(1,5)} \tag{3.32}$$

The b_1 and b_2 are combination coefficients that satisfy $b_1 + b_2 = 0$ for retaining geometry terms and $\beta_{(l,m,n)} - b_1\beta_{(1,-1,0)} + b_2\beta_{(1,0,-1)} = 0$ for eliminating ionospheric delay term. The values of combination coefficient are computed as follows.

$$b_1 = \frac{\beta_{(l,m,n)}}{\beta_{(1,-1,0)} - \beta_{(1,0,-1)}} \tag{3.33}$$

$$b_2 = -\frac{\beta_{(l,m,n)}}{\beta_{(1,-1,0)} - \beta_{(1,0,-1)}} \tag{3.34}$$

The corresponding wavelength and noise level are expressed as,

$$\lambda_{WL-PR} = \left|\beta_{(l,m,n)} \cdot K_1\right| \tag{3.35}$$

$$\begin{aligned}\sigma\left(\varepsilon_{\Delta\nabla\phi_{WL-PR}}\right) &= \sigma\left(\varepsilon_{\Delta\nabla\rho_{(l,m,n)}} + b_1\varepsilon_{\Delta\nabla\phi_{(1,-1,0)}} + b_2\varepsilon_{\Delta\nabla\phi_{(1,0,-1)}}\right) \\ &= \sqrt{\left(\mu_{(l,m,n)} \cdot \sigma_{\Delta\nabla\rho}\right)^2 + \left(\beta_{(l,m,n)} \cdot K_2 \cdot \sigma_{\Delta\nabla\phi}\right)^2}\end{aligned} \tag{3.36}$$

where

$$K_1 = \frac{\lambda_{(1,-1,0)} - \lambda_{(1,0,-1)}}{\beta_{(1,-1,0)} - \beta_{(1,0,-1)}} = -1.98\,m \tag{3.37}$$

$$K_2 = \frac{\mu_{(1,-1,0)} - \mu_{(1,0,-1)}}{\beta_{(1,-1,0)} - \beta_{(1,0,-1)}} = 83.1 \tag{3.38}$$

Unlike Jia's strategy of finding new combination coefficients with the minimum ratio of noise to the wavelength [102], this thesis finds new coefficients with the minimum ADOP performance considering the noise correlation with carrier-phase based WLIF combination.

- Performance criteria of Jia's strategy [102]

$$\min J_1 = \left| \frac{\sigma\left(\varepsilon_{\Delta\nabla\phi_{WL-PR}}\right)}{\lambda_{WL-PR}} \right| \approx \frac{\mu_{(l,m,n)}}{\left|\beta_{(l,m,n)} \cdot K_1\right|} \quad \textbf{(3.39)}$$

- Performance criteria of proposed method

$$\min J_2 = \left| \frac{\sigma\left(\varepsilon_{\Delta\nabla\phi_{WL-PR}} - \varepsilon_{\Delta\nabla\phi_{WL-IF}}\right)}{\lambda_{WL-PR} - \lambda_{WL-IF}} \right| \approx \frac{\mu_{(l,m,n)}}{\left|\beta_{(l,m,n)} \cdot K_1 - \lambda_{WL-IF}\right|} \quad \textbf{(3.40)}$$

The pseudorange coefficients of GPS triple-frequency signals for satisfying the minimize criterion of Jia's strategy are selected as $(l,m,n) = (3,6,7)$, and the minimize criterion of proposed method are selected as $(13,2,0)$. Table 3.6 summarizes the linear coefficients of the new pseudorange aided WL combination and its performance index according to each criteria. Figure 3.17 shows the ADOP performance according to each coefficient. As a result, the proposed coefficients $(13,2,0)$ shows the best ADOP performance when it uses with carrier-phase based WLIF combination together. On the other hand, the Jia's criterion of $(3,6,7)$ shows the minimum noise ratio for wavelength, which means the best performance when used alone without a WLIF combination.

The typical L1/L2 pseudorange NL combination $(1,1,0)$ is also analyzed together. This typical combination shows the better ADOP performance than Jia's combination of $(3,6,7)$, and have similar ADOP performance with optimal combination $(13,2,0)$. Therefore, the compact WARTK system has chosen the coefficients $(1,1,0)$ considering an engineering perspective. This typical combination is equivalent to the L1/L2 Melbourne-Wübbena linear-combination

$\Delta\nabla\phi_{MW}$ considering the correlation with WLIF combination, and have near optimal performance.

$$\begin{aligned}\Delta\nabla\phi_{WL-PR} &= \Delta\nabla\rho_{(1,1,0)} + b_1 \cdot \Delta\nabla\phi_{WL(1,2)} + b_2 \cdot \Delta\nabla\phi_{WL(1,5)} \\ &= \Delta\nabla\phi_{WL-IF} - \left(\Delta\nabla\phi_{(1,-1,0)} - \Delta\nabla\rho_{(1,1,0)}\right) \\ &= \Delta\nabla\phi_{WL-IF} - \Delta\nabla\phi_{MW}\end{aligned} \tag{3.41}$$

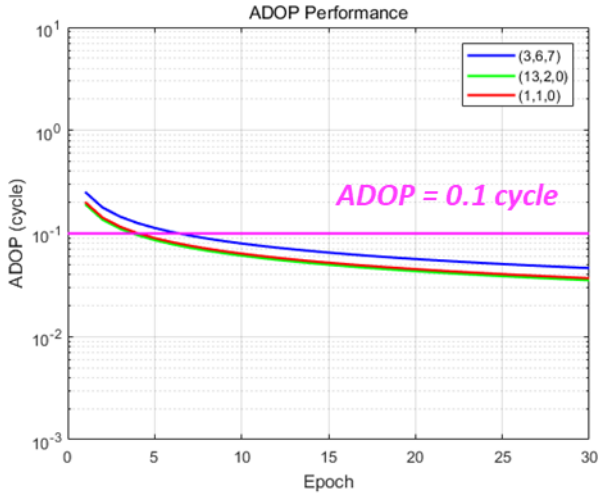

Figure 3.17 ADOP performance for WL ambiguity resolution according to each pseudorange coefficients

Table 3.6 Coefficients of pseudorange aided WL combination

PR Coeff.	*NSF (μ)*	*Wavelength (m)*	*Criteria J_1*	*Criteria J_2*
(3,6,7)	0.59	3.08	0.19	1.83
(13,2,0)	0.90	2.12	0.42	0.70
(1,1,0)	0.71	2.54	0.28	0.83

Finally, the observation model for WL ambiguity resolution can be constructed using two mutually independent ionospheric-free combinations; one is the L1/L2 Melbourne-Wübbena combination and another is the WLIF combination using triple-frequency signals.

$$\begin{bmatrix} \Delta\nabla\phi_{WL1} \\ \Delta\nabla\phi_{WL2} \end{bmatrix} = \begin{bmatrix} 0 \\ G \end{bmatrix} \bar{b} + \begin{bmatrix} \lambda_{WL1} \\ \lambda_{WL2} \end{bmatrix} \Delta\nabla N_{WL} + \begin{bmatrix} \varepsilon_{\Delta\nabla\phi_{WL1}} \\ \varepsilon_{\Delta\nabla\phi_{WL2}} \end{bmatrix} \quad \textbf{(3.42)}$$

where

$$\Delta\nabla\phi_{WL1} = \Delta\nabla\phi_{MW} = \Delta\nabla\phi_{(1,-1,0)} - \Delta\nabla\rho_{(1,1,0)} \quad \textbf{(3.43)}$$

$$\begin{aligned} \Delta\nabla\phi_{WL2} &= \Delta\nabla\phi_{WL-IF} \\ &= a_1 \cdot \Delta\nabla\phi_{(1,-1,0)} - a_2 \cdot \left(\Delta\nabla\phi_{(1,0,-1)} - \lambda_{(1,0,-1)} \Delta\nabla\breve{N}_{(0,1,-1)} \right) \end{aligned} \quad \textbf{(3.44)}$$

This observation model is available for both dual- and triple-frequency signals. The WPF and triple-frequency user takes full advantage of the geometry-based WL filter. The WPF process which known station locations estimates the zenith tropospheric delay of each station with WL integer ambiguity. The user process estimates the position, velocity, and acceleration with WL integer ambiguity. On the other hand, the dual-frequency users who applies only geometry-free L1/L2 Melbourne-Wübbena combination estimates the multipath modeled as the 1st order Markov process [4]. Likewise EWL ambiguity resolution, the WL ambiguity resolution performance of triple-frequency user was analyzed through simple Monte-Carlo simulation. Table 3.7 and Table 3.8 show the summary of Monte-Carlo simulation results. As a result, the success-fix rate of WL ambiguity resolution is 100% and RMS statistics of TTFF is about 2.05 epochs.

Table 3.7 Monte-Carlo simulation results of WL ambiguity resolution

5000 samples	*Correct (Success, P_s)*	*Wrong (Failure, P_f)*
Fixed	100%	0%
Float (undecided, P_u)	0%	

Table 3.8 RMS statistics at the fixed time of WL integer ambiguity

RMS statistics (5000 samples)	
Time-To-First-Fix (epoch)	2.05
Ambiguity DOP (cycle)	0.13
Position DOP	1.06

3.2.5 Narrow-Lane (NL) Ambiguity Resolution

In order to calculate the centimeter-level position, the NL ambiguity must be accurately determines but it is very difficult compared to EWL and WL ambiguity resolution. This paper introduces the NL ambiguity resolution method based on geometry-based ionospheric-free combination using triple-frequency signals to improve the NL resolution performance.

When the EWL and WL integer ambiguity is correctly resolved, the fixed EWL ambiguity $\Delta\nabla\breve{N}_{EWL}$ and WL ambiguity $\Delta\nabla\breve{N}_{WL}$ can be used in NL ambiguity resolution. Therefore, the integer ambiguities of L2, and L5 frequency can be re-formed as L1 integer ambiguity as following equation.

$$\Delta\nabla N_{(0,1,0)} = \Delta\nabla N_{(1,0,0)} - \Delta\nabla \breve{N}_{WL} \tag{3.45}$$

$$\Delta\nabla N_{(0,0,1)} = \Delta\nabla N_{(1,0,0)} - \Delta\nabla \breve{N}_{WL} - \Delta\nabla \breve{N}_{EWL} \tag{3.46}$$

Through the integer adjusting by this relationship, the L1, L2, and L5 carrier-phase observations have the same NL integer ambiguity value $\Delta\nabla N_{NL} = \Delta\nabla N_{(1,0,0)}$ with different wavelengths.

$$\begin{aligned}\Delta\nabla\phi_{L1} &= \Delta\nabla\phi_{(1,0,0)} \\ &= \Delta\nabla d + \Delta\nabla T - \beta_{(1,0,0)}\Delta\nabla I + \lambda_{(1,0,0)}\Delta\nabla N_{NL} + \varepsilon_{\Delta\nabla\phi_{(1,0,0)}}\end{aligned} \tag{3.47}$$

$$\begin{aligned}\Delta\nabla\phi_{L2} &= \Delta\nabla\phi_{(0,1,0)} + \lambda_{(0,1,0)}\Delta\nabla \breve{N}_{WL} \\ &= \Delta\nabla d + \Delta\nabla T - \beta_{(0,1,0)}\Delta\nabla I + \lambda_{(0,1,0)}\Delta\nabla N_{NL} + \varepsilon_{\Delta\nabla\phi_{(0,1,0)}}\end{aligned} \tag{3.48}$$

$$\begin{aligned}\Delta\nabla\phi_{L5} &= \Delta\nabla\phi_{(0,0,1)} + \lambda_{(0,0,1)}\Delta\nabla \breve{N}_{WL} + \lambda_{(0,0,1)}\Delta\nabla \breve{N}_{EWL} \\ &= \Delta\nabla d + \Delta\nabla T - \beta_{(0,0,1)}\Delta\nabla I + \lambda_{(0,0,1)}\Delta\nabla N_{NL} + \varepsilon_{\Delta\nabla\phi_{(0,0,1)}}\end{aligned} \tag{3.49}$$

All of the mutually independent NL combination can be constructed from these L1, L2, and L5 basis observation. Likewise the WL ambiguity resolution, the two independent ionospheric-free combination that constructed by basis observations are used for NL ambiguity resolution. The L1/L2 ionospheric-free combination and L1/L5 ionospheric-free combination selected for compact WARTK system can be expressed as follows.

$$\begin{aligned}\Delta\nabla\phi_{NL1} &= \frac{f_1^2}{f_1^2 - f_2^2}\cdot\Delta\nabla\phi_{L1} - \frac{f_2^2}{f_1^2 - f_2^2}\cdot\Delta\nabla\phi_{L2} \\ &= \Delta\nabla d + \Delta\nabla T + \lambda_{NL1}\Delta\nabla N_{NL} + \varepsilon_{\Delta\nabla\phi_{(77,-60,0)}}\end{aligned} \tag{3.50}$$

$$\begin{aligned}\Delta\nabla\phi_{NL2} &= \frac{f_1^2}{f_1^2 - f_5^2}\cdot\Delta\nabla\phi_{L1} - \frac{f_5^2}{f_1^2 - f_2^2}\cdot\Delta\nabla\phi_{L5} \\ &= \Delta\nabla d + \Delta\nabla T + \lambda_{NL2}\Delta\nabla N_{NL} + \varepsilon_{\Delta\nabla\phi_{(154,0,-115)}}\end{aligned} \tag{3.51}$$

The corresponding wavelength are written as,

$$\lambda_{NL1} = \lambda_{(1,1,0)} = 10.7\,cm \tag{3.52}$$

$$\lambda_{NL2} = \lambda_{(1,0,1)} = 10.9\,cm \tag{3.53}$$

and the noise level are expressed as follows.

$$\begin{aligned}\sigma\left(\varepsilon_{\Delta\nabla\phi_{NL1}}\right) &= \mu_{(77,-60,0)} \cdot \sigma_{\Delta\nabla\phi} = 2.98 \cdot \sigma_{\Delta\nabla\phi} \\ &\approx 11.9\,mm\end{aligned} \tag{3.54}$$

$$\begin{aligned}\sigma\left(\varepsilon_{\Delta\nabla\phi_{NL2}}\right) &= \mu_{(154,0,-115)} \cdot \sigma_{\Delta\nabla\phi} = 2.59 \cdot \sigma_{\Delta\nabla\phi} \\ &\approx 10.4\,mm\end{aligned} \tag{3.55}$$

Using these two independent ionosphere-free combinations, the geometry-based model for NL ambiguity resolution can be expressed as follow.

$$\begin{bmatrix}\Delta\nabla\phi_{NL1} \\ \Delta\nabla\phi_{NL2}\end{bmatrix} = \begin{bmatrix}G \\ G\end{bmatrix}\bar{b} + \begin{bmatrix}\lambda_{NL1} \\ \lambda_{NL2}\end{bmatrix}\Delta\nabla N_{NL} + \begin{bmatrix}\varepsilon_{\Delta\nabla\phi_{NL1}} \\ \varepsilon_{\Delta\nabla\phi_{NL2}}\end{bmatrix} \tag{3.56}$$

This observation model is also available for both dual- and triple-frequency signals. The WPF and triple-frequency user takes full advantage of the geometry-based NL filter. The dual-frequency users have slightly low performance than the triple-frequency users. In the Kalman filter of NL ambiguity resolution, the WPF process estimates the precise zenith tropospheric delay of each station, and the user estimates the position, velocity, and acceleration. After applying the Kalman filter, the NL integer ambiguity can be fixed and validated by the LAMBDA algorithm.

The NL ambiguity resolution performance of triple-frequency and dual-frequency users were analyzed through simple Monte-Carlo simulation. Figure 3.18 and Figure 3.19 show the log-scaled ADOP performance of triple-frequency users and dual-frequency user, respectively.

Table 3.9 and Table 3.10 show the summary of Monte-Carlo simulation results of triple-frequency users. As a result, the success-fix rate of NL ambiguity resolution is 100% and RMS statistics of TTFF is about 3.08 epochs. Table 3.11 and Table 3.12 show the summary of Monte-Carlo simulation results of dual-frequency users. As a result, the success-fix rate of NL ambiguity resolution is 99.8% and RMS statistics of TTFF is about 27.08 epochs. As a result, the triple-frequency users can quickly and correctly determine the NL integer ambiguity than dual-frequency users.

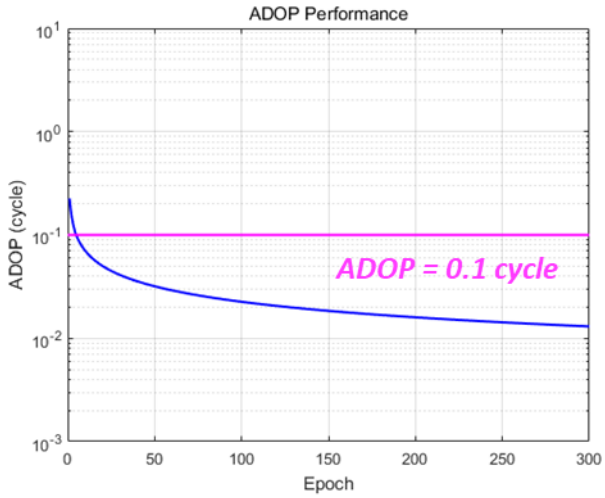

Figure 3.18 ADOP performance of NL ambiguity resolution (Triple-frequency user)

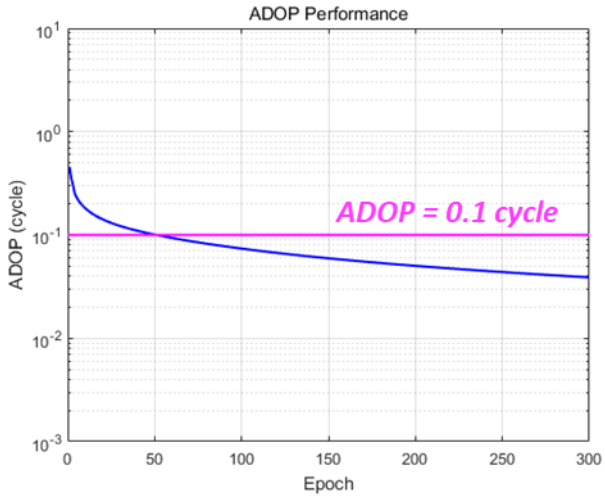

Figure 3.19 ADOP performance of NL ambiguity resolution (Dual-frequency user)

Table 3.9 Monte-Carlo simulation results of NL ambiguity resolution (Triple-frequency user)

5000 samples	***Correct (Success, P_s)***	***Wrong (Failure, P_f)***
Fixed	100%	0%
Float (undecided, P_u)	0%	

Table 3.10 RMS statistics at the fixed time of NL integer ambiguity (Triple-frequency user)

RMS statistics (5000 samples)	
Time-To-First-Fix (epoch)	3.08
Ambiguity DOP (cycle)	0.13
Position DOP	1.06

Table 3.11 Monte-Carlo simulation results of NL ambiguity resolution (Dual-frequency user)

5000 samples	***Correct (Success, P_s)***	***Wrong (Failure, P_f)***
Fixed	99.8 % (4990 samples)	0.2 % (10 samples)
Float (undecided, P_u)	0 %	

Table 3.12 RMS statistics at the fixed time of NL integer ambiguity (Dual-frequency user)

RMS statistics (5000 samples)	
Time-To-First-Fix (epoch)	27.08
Ambiguity DOP (cycle)	0.14
Position DOP	1.06

3.3 Compact Wide-Area RTK Corrections

The compact WARTK system generates the vector-type concept of correction for each error component using precise carrier-phase observations after the WPF process correctly resolved the integer ambiguity. There are three types of corrections: satellite orbit corrections, satellite CPC corrections, and tropospheric corrections. The satellite orbit corrections are expressed as a three-dimensional orbit error vector form for each satellite. The satellite CPC corrections for fully eliminating the satellite clock related error are expressed as a scalar-range form for each satellite. The tropospheric corrections are expressed as a vector form for zenith wet delay that is modeled by 16 coefficients of spherical harmonics function.

Figure 3.20 shows the comparison of correction concept of network RTK, PPP-RTK, and compact WARTK. The double-differenced observations by OSR corrections of network RTK can perfectly eliminate the satellite clock related error and receiver clock related error; while the representation error increase when the size of network is expanded due to spatial decorrelation. Furthermore, the OSR corrections generated for each satellite and each station require a lot of broadcast bandwidth. On the other hands, the SSR corrections of PPP-RTK can apply the characteristics of each error component independently, and significantly reduced the bandwidth compared to OSR [7]. However, the un-differenced observations of PPP-RTK have a residual error for satellite and receiver clock related components. In addition, the PPP-RTK require a lot of reference stations globally and locally to generate their SSR corrections.

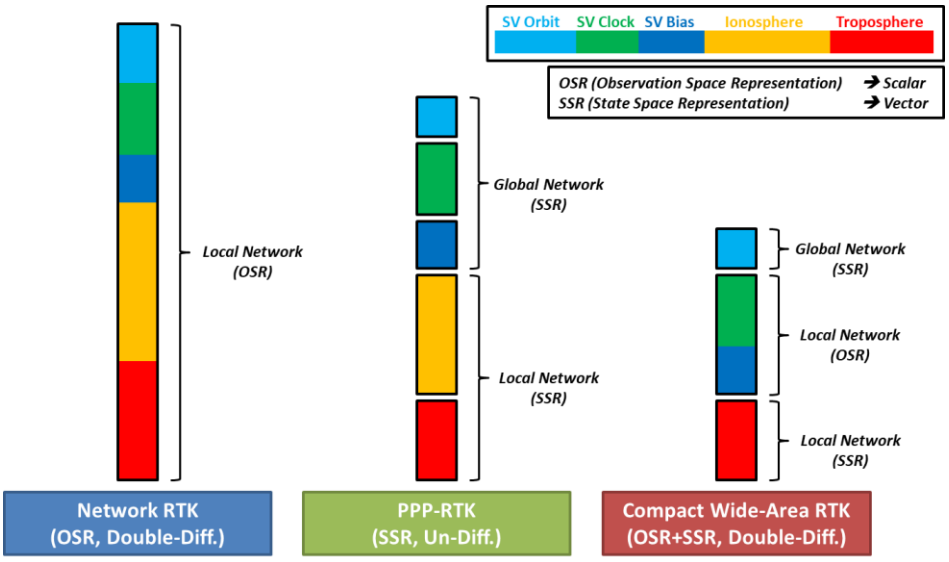

Figure 3.20 Concept of corrections for network RTK, PPP-RTK, and compact wide-area RTK

The corrections of compact WARTK system only combines the advantages of the OSR concept of network RTK and that of the SSR concept of PPP-RTK. The overall strategy of compact WARTK that adopts the vector-type corrections of each error component for expanding service coverage is very similar to PPP-RTK system. The satellite orbit corrections and tropospheric corrections of compact WARTK system are similar concept of SSR corrections of PPP-RTK system. However, the satellite CPC corrections of compact WARTK system remains the OSR form like the network RTK. The PPP-RTK produces the satellite clock corrections and code/phase bias corrections separately using reference stations around the world, while the compact WARTK generates the satellite CPC corrections using only local network without distinction of satellite clock error and code/phase hardware bias. This allows for complete elimination of satellite clock related errors as in network RTK.

Furthermore, the message amounts of compact WARTK corrections can be dramatically reduced even then network RTK and PPP-RTK. The compact WARTK system does not require ionospheric corrections since the user computes their integer ambiguity and position based on ionospheric-free linear combinations. The bandwidth for satellite orbit corrections is same as that of PPP-RTK, while the bandwidth for satellite CPC corrections and tropospheric corrections is further reduced than the PPP-RTK. In addition, as shown the Figure 3.21, the message scheduling is conceptually possible according to properties of each error element likewise SSR corrections. This thesis focuses on how to reduce the bandwidth of satellite CPC corrections and tropospheric corrections than network RTK and PPP-RTK.

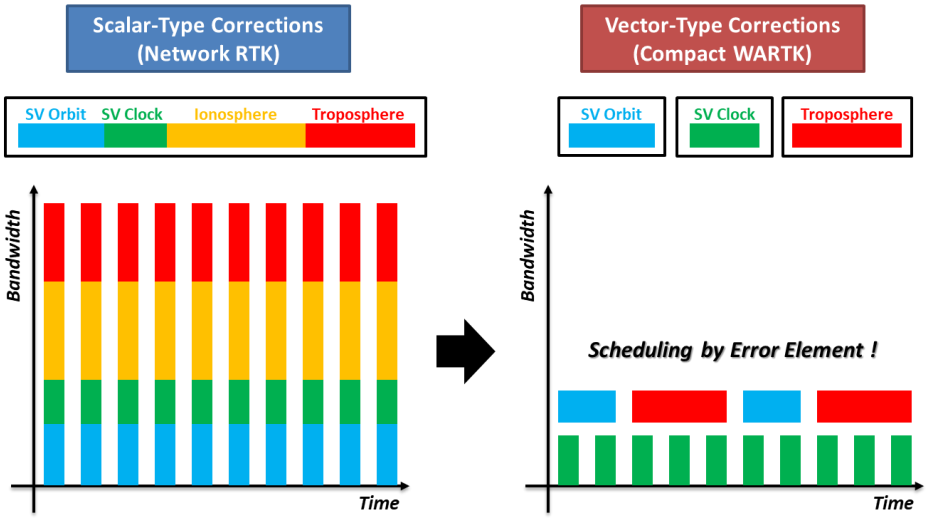

Figure 3.21 Message scheduling concept of scalar-type corrections and vector-type corrections

3.3.1 Satellite Orbit Corrections

The satellite orbit corrections for calculating precise satellite position contain the three-dimensional orbit vectors in radial, along-track, and cross-track components. IGS provides the precise ultra-rapid products as real-time SSR orbit corrections in RTCM standards. This product are computed using recent satellite signals of 3 days to predict the precise orbit for 24 hour thereafter. The accuracy of the ultra-rapid orbit is 1D mean RMS 5 cm over the three XYZ geocentric components [12], [50], [104]. Similar with SSR orbit corrections in IGS, the WPF of compact WARTK system applied our own real-time POD products that estimates precise orbit position using double-differenced carrier-phase observations and real-time orbit propagation model. Our POD products have similar accuracy of IGS ultra-rapid product as shown in Figure 3.22 [84].

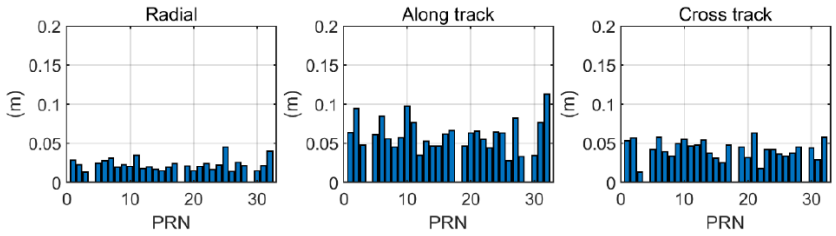

Figure 3.22 RMS error statistics of precise orbit determination [84]

The satellite orbit corrections of radial, along-track, cross-track components are generated from the position difference between precise orbit product and broadcast ephemeris orbit as following equation. The details are beyond the scope of this dissertation. As with the Compact SSR orbit corrections in the QZSS CLAS, the satellite velocity information is not provided to users since the rate of change in satellite orbit error is much slower than correction update interval [28], [29].

$$\delta\bar{O} = \begin{bmatrix} \delta O_{radial} \\ \delta O_{along} \\ \delta O_{cross} \end{bmatrix} = T_{ECEF\,2\,RAC} \cdot \left(\bar{R}_{POD} - \bar{R}_{broadcast} \right) \tag{3.57}$$

where

$\delta\bar{O}$: satellite orbit corrections in RAC coordinates

$\bar{R}_{POD}$: satellite precise position in ECEF coordinates by POD products

$\bar{R}_{broadcast}$: satellite position in ECEF coordinates by broadcast ephemeris

$T_{ECEF\,2\,RAC}$: transformation matrix of ECEF coordinates to RAC coordinates

3.3.2 Satellite Code/Phase Clock (CPC) Corrections

The satellite CPC corrections of each satellite to eliminate the satellite clock offset and code/phase hardware bias consist of the five linear-combinations called CPC-EWL, CPC-WL, CPC-NL1, CPC-NL2, and CPC-PRIF. These corrections are linear combinations as summarized in Table 3.3 for resolving the integer ambiguity using the proposed TCAR method. CPC-EWL is represented by L2/L5 Melbourne-Wübbena combination for EWL ambiguity resolution. CPC-WL1 is represented by L1/L2 Melbourne-Wübbena combination for WL ambiguity resolution. CPC-NL1 and CPC-NL2 are L1/L2 and L1/L5 ionospheric-free combinations for NL ambiguity resolution. CPC-PRIF is pseudorange-based combinations for initializing user positions.

$$CPC_{EWL} = \beta^{Tx}_{\phi_{EWL}} - \delta\breve{\beta}^{Rx}_{\phi_{EWL}} - \lambda_{(0,1,-1)}\delta N_{(0,1,-1)} \quad \textbf{(3.58)}$$

$$CPC_{WL1} = \beta^{Tx}_{\phi_{WL1}} - \delta\breve{\beta}^{Rx}_{\phi_{WL1}} - \lambda_{(1,-1,0)}\delta N_{(1,-1,0)} \quad \textbf{(3.59)}$$

$$CPC_{NL1} = \left(\delta b + \beta^{Tx}_{\phi_{NL1}}\right) - \delta\breve{\beta}^{Rx}_{\phi_{NL1}} - \lambda_{(77,-60,0)}\delta N_{(77,-60,0)} \quad \textbf{(3.60)}$$

$$CPC_{NL2} = \left(\delta b + \beta^{Tx}_{\phi_{NL2}}\right) - \delta\breve{\beta}^{Rx}_{\phi_{NL2}} - \lambda_{(154,0,-115)}\delta N_{(154,0,-115)} \quad \textbf{(3.61)}$$

$$CPC_{PRIF} = \left(\delta b + \beta^{Tx}_{\rho_{IF}}\right) - \delta\breve{\beta}^{Rx}_{\rho_{IF}} \quad \textbf{(3.62)}$$

The CPC corrections for WLIF combination that is another combination for WL ambiguity resolution is not required to broadcasting to users. It can be produced by the user itself by combining the CPC-NL1 and CPC-NL2 as following equation.

$$CPC_{WL2} = \frac{f_1 + f_2}{f_2 - f_5} \cdot CPC_{NL1} - \frac{f_1 + f_5}{f_2 - f_5} \cdot CPC_{NL2} \quad \textbf{(3.63)}$$

The rate of change of satellite clock error is faster than the satellite orbit and tropospheric delay; therefore, the message update interval is relatively fast. Among the satellite CPC corrections, CPC-EWL, CPC-WL1, and CPC-PRIF, which are combined with the pseudorange measurements, have low message resolution and low update interval. On the other hand, CPC-NL1 and CPC-NL2, which are linear combinations of carrier phase only, have high message resolution and fast update interval. The detailed algorithms for correction generating method will be discussed in Chapter 4.

3.3.3 Tropospheric Corrections

The tropospheric corrections contain the 16 coefficients of 3rd order spherical harmonics function that represents the zenith wet delay (ZWD) on mean-sea-level. C_{nm}, S_{nm} represent the spherical harmonics coefficients.

$$\hat{x}_{ZWD} = \{C_{00}, C_{10}, C_{20}, C_{30}, C_{11}, C_{21}, C_{31}, C_{22}, C_{32}, C_{33}, \cdots \\ S_{11}, S_{21}, S_{31}, S_{22}, S_{32}, S_{33}\} \quad \textbf{(3.64)}$$

The user can precisely eliminate the zenith wet delay at user location by reconstructing the coefficients. The zenith hydrostatic delay can be eliminated by the user itself using the empirical tropospheric model. The rate of change of tropospheric delay is slow that means the message for tropospheric corrections have a long update interval. The detailed algorithms for correction generating method will be discussed in Chapter 5.

3.3.4 Message Design for GEO Broadcasting

In this study, the message of compact WARTK are designed to be broadcast through GEO satellite in compliance with international standards, i.e. the SBAS standard messages developed by the Ratio Technical Commission for Aeronautics (RTCA) [105].

The SBAS message of the international standard is possible to broadcast via GEO satellite of 250 bps. Figure 3.23 shows the message format of SBAS. A block is defined as the complete 250 bits, while a message is defined as the 212 bits data field. The 8-bit preamble starts at bit 0 of the 250-bit block followed by the 6-bit message type at bit 8. The data field then starts at bit 14, followed by the parity field that starts at bit 226. 24 bits of Cyclic Redundancy Check (CRC) parity will provide protection against burst as well as random error [63].

The compact WARTK messages are designed to conform to the data field of 212 bits in accordance with this SBAS standards. The suggested message data field and update time for transmission of the compact WARTK correction is shown in Table 3.13. The message data fields for satellite orbit corrections borrowed the format and scheduling of compact SSR messages in QZSS CLAS [28]–[30]. The message data fields of satellite CPC corrections and tropospheric corrections are defined taking into account the characteristics of each correction. More details will be discussed on Chapter 4 and Chapter 5, respectively.

According to Table 3.13, satellite orbit and CPC corrections for one satellite require 10.6 bps considering the message update interval. The tropospheric corrections of 16 coefficients require 25.6 bps. Therefore, the corrections for 16

satellites can be broadcast even considering the spare 8 bits for issue of data for message time tagging. In conclusion, the compact WARTK message is available to expand for multi-GNSS corrections.

$$25.6+10.6\times N_{sv} \le 204(=212-8)\,bps$$
$$\therefore Maximum\,N_{sv}=16 \qquad \textbf{(3.65)}$$

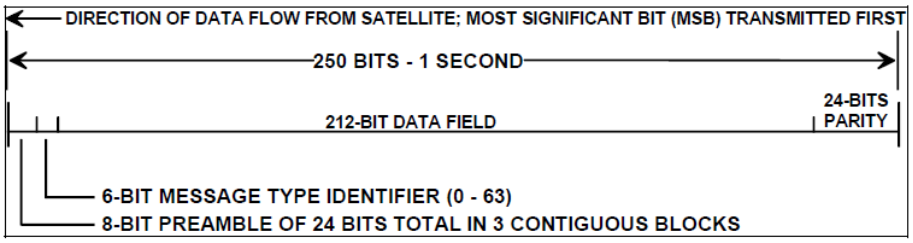

Figure 3.23 SBAS message data block format (250 bps) [63]

Table 3.13 Compact wide-area RTK message data field (TBD)

Data Field		*Data Type*	*Resolution*	*Range*	*Update*
Orbit	Radial	int 15	0.0016 m	±26.2128 m	30 sec
	Along-Track	int 13	0.0064 m	±26.208 m	30 sec
	Cross-Track	int 13	0.0064 m	±26.208 m	30 sec
CPC	PRIF	int 12	0.01 m	±20.47 m	10 sec
	EWL	int 12	0.01 m	±20.47 m	10 sec
	WL1	int 12	0.01 m	±20.47 m	10 sec
	NL1	int 14	0.001 m	±8.191 m	5 sec
	NL2	int 14	0.001 m	±8.191 m	5 sec
Tropo	ZWD	int 16	0.001	±32.767	10 sec

Intentionally Blank Page

CHAPTER 4. CODE/PHASE CLOCK (CPC) CORRECTION GENERATION ALGORITHM

4.1 Former Research of RTK Correction Protocol

Generally, the traditional RTK and network RTK provide the precise location of reference station and RTK corrections to fully eliminate the satellite clock related error and to reduce the other GNSS error in user measurements. There are two groups of data protocols for broadcasting RTK corrections through the communication links such as internet. First one is observation based data protocol that is standardized by the RTCM special committee no.104 (SC-104). The other one is correction based data protocol such as Compact RTK [13], [14]. This section introduces existing RTK correction protocols and discuss their pros and cons.

4.1.1 Observation Based RTK Data Protocol

The observation based RTK data protocol broadcasts raw observations of reference stations themselves as RTK corrections. This protocol has three advantages. First of all, there is no need to transmit the Issue of Data, Ephemeris (IODE) value of reference stations to the users, and no need to strictly unify the function of satellite position and clock calculation. The RTK users can calculate the GPS satellite position and clock offset using the recent received IODE value without having to synchronize with IODE of reference stations. That is, different GPS instruments can be interoperable. Second, the message amount can be reduced since the pseudorange and carrier-phase observations simultaneously broadcasts through

a single message with high compression efficiency. Third, the maintenance and operation for RTK service is easy because there is no need to equip the RTK correction generators [3], [13], [106].

However, this protocols are very vulnerable to communication failure since the raw GNSS observations contain very large nonlinear values such as geometric distance and receiver clock offset. Therefore, the observation based protocol requires high-speed data bandwidth to reduce performance degradation induced by communication failure, and RTK users should have special algorithm for latency compensation to reduce temporal decorrelation error. Furthermore, the RTK users have to monitor and compensate the correction roll-over, which is induced by limiting and compressing the range of raw observations to reduce the message volumes [3], [13], [106].

Typically, there are MT 18-19 of RTCM version 2, and MT 1001-1004 of RTCM version 3. In order to support full L1/L2 RTK service through RTCM version 3 protocol, MT 1004 of GPS L1/L2 observations and MT 1005 of station coordinates are broadcasted to users. Table 4.1 describes the data contained in MT 1004 of RTCM version 3 [12]. According to RTCM recommendation, the L1/L2 GPS-RTK services for 9 visible satellites with 1 Hz scheduling require an average of 1,240 bps of data. Consequently, this requires at least 1,200 bps of data communication link to transmit RTK corrections [6], [106].

Table 4.1 MT 1004 of RTCM version 3 (GPS Extended RTK, L1/L2) [12]

DATA FIELD	DF NUMBER	DATA TYPE	NO. OF BITS
GPS Satellite ID	DF009	uint6	6
GPS L1 Code Indicator	DF010	bit(1)	1
GPS L1 Pseudorange	DF011	uint24	24
GPS L1 Phaserange – L1 Pseudorange	DF012	int20	20
GPS L1 Lock time Indicator	DF013	uint7	7
GPS Integer L1 Pseudorange Modulus Ambiguity	DF014	uint8	8
GPS L1 CNR	DF015	uint8	8
GPS L2 Code Indicator	DF016	bit(2)	2
GPS L2-L1 Pseudorange Difference	DF017	int14	14
GPS L2 Phaserange – L1 Pseudorange	DF018	int20	20
GPS L2 Lock time Indicator	DF019	uint7	7
GPS L2 CNR	DF020	uint8	8
TOTAL			***125***

4.1.2 Correction Based RTK Data Protocol

The correction based RTK data protocol has the advantage of reducing temporal decorrelation errors by utilizing the linearity of the corrections. Unlike the observation based protocol, the correction based protocol is very robust to latency and easy to compensate latency error using range-rate correction without special latency compensation filter. Furthermore, the range of corrections is much narrower than the observation, and the required data bandwidth is also lower; therefore, the RTK user does not need to monitor the roll-over of the corrections. However, there is interoperability problem that the algorithms of satellite position and clock calculation and the IODE value between reference station and user must be exactly same [3], [13], [106].

Typically, there are MT 20-21 of RTCM version 2, and the Compact RTK protocol proposed by Kee and Kim [13]. The correction-based compact RTK protocol was designed as the basic frame structure of RTCM version 3 to enhance the robustness of latency without significant degradation in accuracy using low-speed data-links. This protocol structure is more compact and advanced than that of the RTCM version 2. Currently, the compact RTK protocol for GPS L1 and L2 signal is assigned in RTCM SC-104 proprietary message, MT 4081 [5]. The following subsections introduce a more detailed about the compact RTK protocol.

4.1.3 Compact RTK Protocol

The compact RTK is a new technique that produces RTK corrections linearly by reducing high-variable errors over time for improving the robustness of latency [106]–[109]. Figure 4.1 represents the block diagram of compact RTK correction generator. The most important function is receiver clock offset estimator. The receiver clock offset is non-linear and has very high variation over time, it should be estimated and removed.

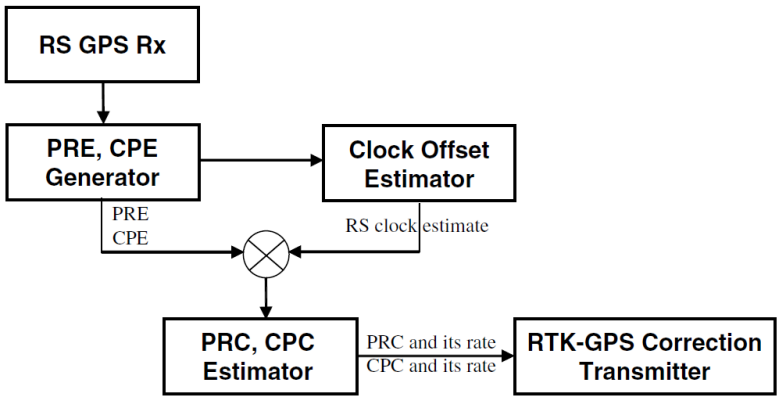

Figure 4.1 Block diagram of compact RTK correction generator [14]

Equation (4.1) and (4.2) represent the conventional observation-based RTCM correction ϕ and the compact RTK correction $\delta\phi$, respectively. The compact RTK correction can be calculated from raw observations by eliminating the non-linear value of geometric distance d and estimated receiver clock offset $\hat{B}$. The receiver clock offset of permanent stationary receivers equipped on WRS can be precisely estimated [14]. The satellite clock offset b computed from the broadcast ephemeris also removed, and the integer ambiguity N is initialized to reduce the size of corrections. The remaining terms in the compact RTK consist of satellite orbit residual error of line-of-sight direction δR, satellite clock residual error δb, satellite phase (or code) bias β_{ϕ}^{Tx}, ionospheric delay I, and tropospheric delay T. These error terms vary slowly over time, less than 2 cm/sec [5]; therefore, the compact RTK can be assumed linear in short time.

- Conventional RTK correction of RTCM MT 1004:

$$\phi = d + \delta R - \left(b + \delta b + \beta_{\phi}^{Tx}\right) - I + T + \left(B + \beta_{\phi}^{Rx}\right) + \lambda N + \varepsilon_{\phi} \qquad \textbf{(4.1)}$$

- Compact RTK correction of RTCM MT 4081:

$$\begin{aligned} \delta\phi &= \phi - d + b - \hat{B} - \lambda\hat{N} \\ &= \delta R - \left(\delta b + \beta_{\phi}^{Tx}\right) - I + T + \delta\beta_{\phi}^{Rx} + \lambda\delta N + \varepsilon_{\delta\phi} \end{aligned} \qquad \textbf{(4.2)}$$

where

$$\delta\beta_{\phi}^{Rx} = \left(B + \beta_{\phi}^{Rx}\right) - \hat{B} \qquad \textbf{(4.3)}$$

$$\delta N = N - \hat{N} \qquad \textbf{(4.4)}$$

The receiver clock residual error with hardware bias $\delta\beta_{\phi}^{Rx}$ is a common bias of all visible satellites that is completely eliminated by single-difference between satellites. The remained integer ambiguities after initialization δN sustain the integer property that it is possible to resolve them in double-difference observations of RTK users.

The compact RTK also provides the range rate-of-change correction to enhance the performance even in the communication outage. Figure 4.2 shows the conceptual figure of latency compensation of compact RTK. Since the compact RTK corrections have very low variation over time through removing most of the non-linear components, it can be effectively compensated their latency error via 1st order extrapolation using the range rate correction. The range rate correction can be estimated from the RTK correction generation filter [14].

- Compact RTK range rate correction of RTCM MT 4081:

$$\delta\dot{\phi} = \frac{d}{dt}\delta\phi \approx \delta\dot{R} - \delta\dot{b} - \dot{I} + \dot{T} + \varepsilon_{\delta\dot{\phi}} \tag{4.5}$$

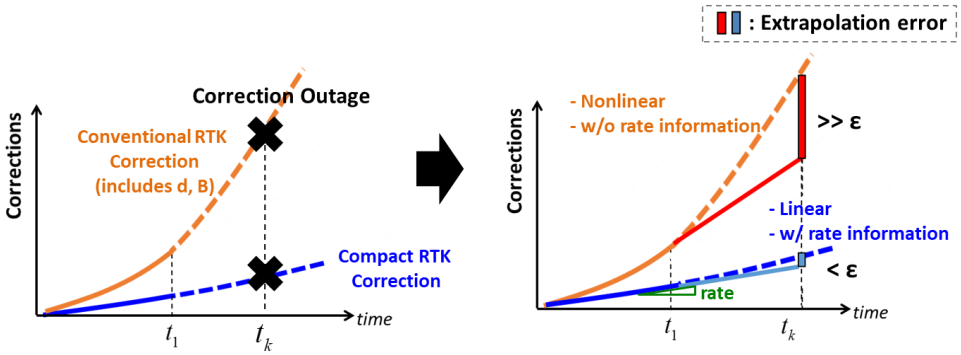

Figure 4.2 Concept of latency compensation of compact RTK [15]

The compact RTK protocol that is suitable for low-speed communication link about 250~600 bps was developed based on RTCM version 3 (Draft 15). This protocol called SNUR-2000 version 2.2. This protocol was designed the separate messages for carrier-phase and pseudorange; therefore, they can be transmit to different update interval depending on the linearity of each corrections. MT 131 contains the carrier-phase correction (CPC), carrier-phase rate correction (CPRC), and several information related to CPC. MT 132 consists of a pseudo-range correction (PRC), pseudo-range rate correction (PRRC), and several information related to PRC [13], [106]. Table 4.2 summarizes the message data field of compact RTK protocol. The message data bit itself is larger than the RTCM MT 1004 as shown in Table 4.1, but the average bandwidth can be reduced about 50 % considering the scheduling. The L1/L2 GPS-RTK services by compact RTK protocol requires a low-speed data-link of 600 bps, assuming that CPC is sent every 2 seconds and PRC is transmit every 20 seconds for 9 visible satellites [106].

Table 4.2 SNUR-2000 v2.2 protocol message data field [106]

Data Field		***Data Type***	***Resolution***	***Range***	***Update***
MT131	L1 CPC	int 19	0.001 m	±262.143 m	2 sec
	L2 CPC	int 19	0.001 m	±262.143 m	2 sec
	L1 CPRC	int 12	0.0001 m/s	±0.2047 m/s	2 sec
	L2 CPRC	int 12	0.0001 m/s	±0.2047 m/s	2 sec
MT132	L1 PRC	int 15	0.02 m	±327.66 m	20 sec
	L2 PRC	int 15	0.02 m	±327.66 m	20 sec
	L1 PRRC	int 8	0.002 m/s	±0.254 m/s	20 sec
	L2 PRRC	int 8	0.002 m/s	±0.254 m/s	20 sec

4.2 Satellite CPC Correction Generation Algorithm

While the compact RTK protocol has the advantage of being able to support the GPS-RTK service without significant accuracy degradation through low-speed data link about 600 bps, there are still performance degradation issues on low-elevation satellites, especially. Figure 4.3 represents the conceptual figure of latency error in high- and low-elevation angle. The compact RTK correction includes the ionospheric delay and tropospheric delay, which are rapidly changing at low-elevation angle; therefore, it requires to schedule the low-elevation corrections more frequently. Furthermore, it is very vulnerable to communication failure induced by complete breakdown of the master station since the corrections are generated by only one receiver.

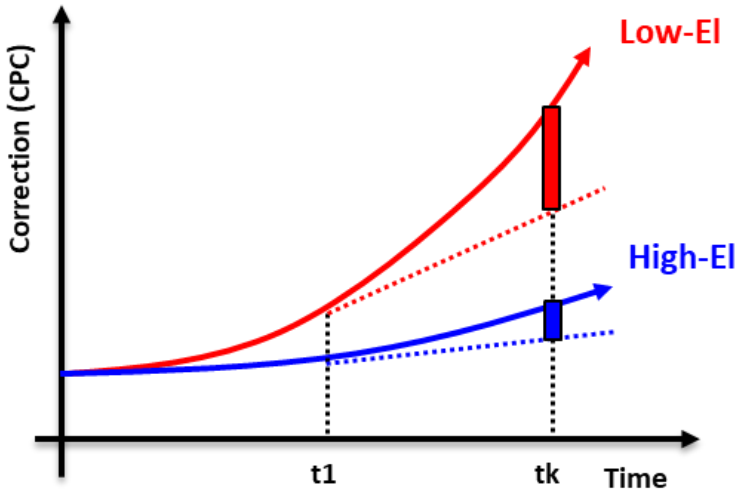

Figure 4.3 Latency performance degradation on low-elevation angle.

The compact WARTK corrections proposed in this thesis are more advanced than the existing compact RTK protocol. Figure 4.4 represents the concept of satellite code/phase clock (CPC) corrections of compact WARTK. The satellite CPC corrections serve as similar to the compact RTK protocol to eliminate the satellite clock offset and code/phase hardware bias. The difference is that the satellite CPC corrections are generated using observations of multiple reference stations; therefore, the system can continuously operate and provide centimeter-level service even when a particular reference station is breakdown. Moreover, the satellite CPC corrections have the lowest variation over time through eliminating the ionospheric delay and tropospheric delay originally included in compact RTK protocol. That means the performance of latency compensation can be enhanced at low-elevation satellite without additional range-rate corrections.

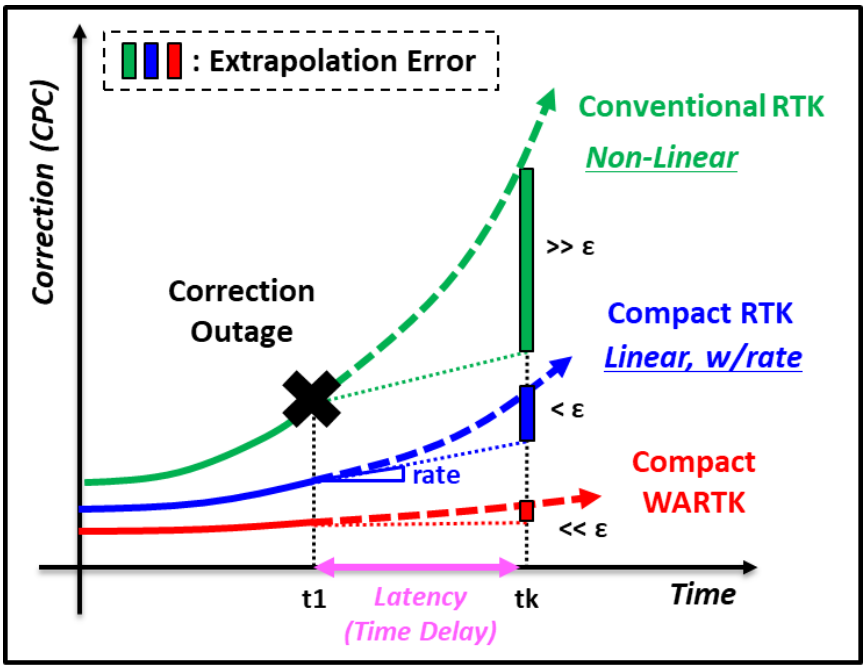

Figure 4.4 Concept of satellite CPC corrections of compact wide-area RTK

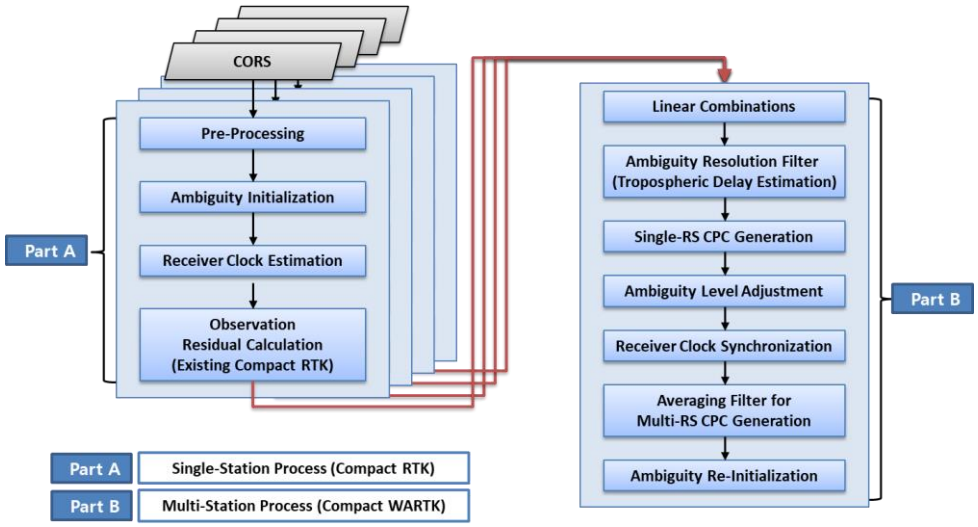

Figure 4.5 Overall process for generating satellite CPC corrections

Figure 4.5 shows the block diagram of overall process for generating satellite CPC corrections in WPF process. Part A is an algorithm for single-station process, which is same to produce existing compact RTK corrections. Part B is a new proposed algorithm for generating multi-station based satellite CPC corrections using the obtained data from part A process. This section introduces the detailed algorithm of part B process using multiple stations.

4.2.1 Temporal Decorrelation Error Reduced Methods

The original compact RTK protocol contains the satellite orbit residual error, satellite clock residual error, ionospheric delay, and tropospheric delay. The absolute value of satellite orbit residual error has a several meter, and that of ionospheric delay and tropospheric delay has a tens of meter. Figure 4.6 shows the temporal variabilities of these error components, and the maximum values of rate-of-change are less than 2 cm/sec [3], [6], [110]–[112]. These GNSS error sources change

relatively slowly over time, but as shown in Figure 4.6, the large rate-of-change value in low-elevation satellite due to ionospheric delay and tropospheric delay causes the temporal decorrelation error even after latency compensation.

The compact WARTK is a technique that produces correction value more linear and smaller than the compact RTK by removing these remaining error sources without satellite clock related terms. First of all, the satellite orbit residual error can be reduced less than 5 cm using the product of precise orbit determination [84]. As considering the spatial characteristics of satellite orbit error, the precise orbit residual error in correction can be more reduced less than 1 cm in double-differenced user range domain within 1,000 km baseline distance [3].

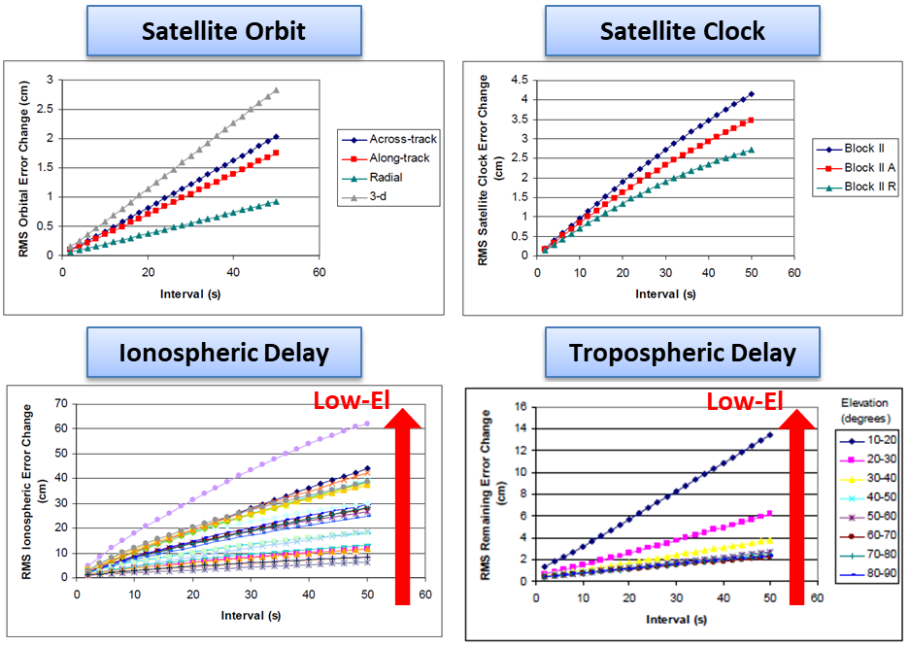

Figure 4.6 Temporal characteristic of GNSS error sources [111], [112]

Second, the ionospheric delay can be fully eliminated by ionosphere-free linear-combinations. The compact WARTK users do not require any ionospheric correction because they apply the proposed TCAR algorithm based on ionospheric-free combinations. Therefore, unlike the conventional RTK, which broadcast the corrections for each frequency signal, the five satellite CPC correction based on ionosphere-free combinations are sufficient to service dual and triple-frequency WARTK users. Third, the tropospheric delay can be precisely estimated and reduced by the proposed TCAR algorithm. After correctly determining he NL integer ambiguity, the WPF process calculates the precise zenith tropospheric delay for each reference station in real-time. More detailed algorithm for tropospheric delay estimation is discussed in Chapter 5. Finally, the five linear-combinations in which the temporal decorrelation error, which consists of satellite orbit, ionospheric delay, and tropospheric delay, has been removed are as follows.

$$\begin{aligned}\delta\tilde{\phi}_{EWL} &= \phi_{(0,1,-1)} - \rho_{(0,1,1)} \\ &= -\beta^{Tx}_{\phi_{EWL}} + \delta\beta^{Rx}_{\phi_{EWL}} + \lambda_{(0,1,-1)}N_{(0,1,-1)} + \varepsilon_{\delta\tilde{\phi}_{EWL}}\end{aligned} \tag{4.6}$$

$$\begin{aligned}\delta\tilde{\phi}_{WL1} &= \phi_{(1,-1,0)} - \rho_{(1,1,0)} \\ &= -\beta^{Tx}_{\phi_{WL1}} + \delta\beta^{Rx}_{\phi_{WL1}} + \lambda_{(1,-1,0)}N_{(1,-1,0)} + \varepsilon_{\delta\tilde{\phi}_{WL1}}\end{aligned} \tag{4.7}$$

$$\begin{aligned}\delta\tilde{\phi}_{NL1} &= \phi_{(77,-60,0)} - d + b - \hat{B} - \delta\hat{R} - \hat{T} \\ &= -\left(\delta b + \beta^{Tx}_{\phi_{NL1}}\right) + \delta\beta^{Rx}_{\phi_{NL1}} + \lambda_{(77,-60,0)}N_{(77,-60,0)} + \varepsilon_{\delta\tilde{\phi}_{NL1}}\end{aligned} \tag{4.8}$$

$$\begin{aligned}\delta\tilde{\phi}_{NL2} &= \phi_{(154,0,-115)} - d + b - \hat{B} - \delta\hat{R} - \hat{T} \\ &= -\left(\delta b + \beta^{Tx}_{\phi_{NL2}}\right) + \delta\beta^{Rx}_{\phi_{NL2}} + \lambda_{(154,0,-115)}N_{(154,0,-115)} + \varepsilon_{\delta\tilde{\phi}_{NL2}}\end{aligned} \tag{4.9}$$

$$\begin{aligned}\delta\tilde{\rho}_{IF} &= \rho_{(77,-60,0)} - d + b - \hat{B} - \delta\hat{R} - \hat{T} \\ &= -\left(\delta b + \beta^{Tx}_{\rho_{IF}}\right) + \delta\beta^{Rx}_{\rho_{IF}} + \varepsilon_{\delta\tilde{\rho}_{IF}}\end{aligned} \tag{4.10}$$

Above linear combinations called single-station based CPC measurements are suitable enough to be considered as the corrections since they contain the satellite clock error and signal biases. The remaining receiver clock offset and integer ambiguity is not a problem since these values are remove or absorbed by the double-differences process. They are much more robust against latency than the compact RTK protocol because we reduced most of the error terms that affect rate-of-change of corrections. However, these CPC measurements still have problems vulnerable to complete breakdown of the reference station. Therefore, the following sections describe how to generate satellite CPC corrections using all CPC measurements of the multiple stations.

4.2.2 Ambiguity Level Adjustment

The satellite clock related error contained in the single-station based CPC measurements of equation (4.11) and (4.12) are common components of all reference stations. The subscripts m and r represent the master station index and the auxiliary station index, respectively. The superscript j represents the visible satellite index. The remaining receiver clock offset and integer ambiguity have different values for each reference station.

- Master-station based CPC measurement:

$$\delta\tilde{\phi}_m^j = -\left(\delta b + \beta_\phi^{Tx}\right)^j + \left(\delta\beta_\phi^{Rx}\right)_m + \lambda N_m^j + \left(\varepsilon_{\delta\tilde{\phi}}\right)_m^j \quad \textbf{(4.11)}$$

- Auxiliary-station based CPC measurement:

$$\delta\tilde{\phi}_r^j = -\left(\delta b + \beta_\phi^{Tx}\right)^j + \left(\delta\beta_\phi^{Rx}\right)_r + \lambda N_r^j + \left(\varepsilon_{\delta\tilde{\phi}}\right)_r^j \quad \textbf{(4.12)}$$

Therefore, the level of integer ambiguity of each auxiliary station must be adjusted to the same value to the master station using a fixed double-difference integer ambiguity between stations. If the level of integer ambiguity is not adjusted, the satellite CPC corrections does not preserve the integer characteristics of ambiguity. The double-difference integer ambiguity between stations can be correctly fixed by the proposed TCAR method. The superscript *ref* represents the reference satellite index.

- Fixed double-difference integer ambiguity between stations:

$$Known \quad {}^{j}_{r}\Delta\nabla^{ref}_{m}\breve{N} \tag{4.13}$$

- Integer ambiguity adjusted CPC measurement of auxiliary station:

$$\begin{aligned}\delta\breve{\phi}_r^{\,j} &= \delta\tilde{\phi}_r^{\,j} - \lambda\cdot {}^{j}_{r}\Delta\nabla^{ref}_{m}\breve{N} \\ &= -\left(\delta b + \beta_{\phi}^{Tx}\right)^{j} + \left(\delta\breve{\beta}_{\phi}^{Rx}\right)_r + \lambda N_m^{j} + \left(\varepsilon_{\delta\tilde{\phi}}\right)_r^{j}\end{aligned} \tag{4.14}$$

where

$$\left(\delta\breve{\beta}_{\phi}^{Rx}\right)_r = \left(\delta\beta_{\phi}^{Rx}\right)_r + \lambda\cdot {}_{r}\Delta^{ref}_{m}N \qquad (r=1,2,\cdots m) \tag{4.15}$$

As we can see equation (4.14), the integer ambiguity of auxiliary station is adjusted to the integer ambiguity of master station. The receiver clock related term of equation (4.15) is still a common bias component of all satellites after absorbing the integer ambiguity term for reference satellite. It can be eliminated by single-difference between satellites.

4.2.3 Receiver Clock Synchronization

The multi-stations based satellite CPC corrections are generated by the average of CPC measurements of each reference station for which integer ambiguity is adjusted. Therefore, even after averaging, the receiver clock related term must have the same value for all satellites to be removed by single-difference between satellites. It does not matter if all reference stations have the same set of visible satellites. However, if a new visible satellite is observed only at a particular station, the value of the receiver clock related term will vary from satellite to satellite after averaging the CPC measurements Therefore, it is necessary to synchronize the receiver clock offset of all reference stations to master station. The common view method, which is one of the algorithm for receiver clock estimation method of SBAS, is applied in this receiver clock synchronization algorithm [61]. The relative value of receiver clock can be calculated by difference between the CPC measurements as follow.

$$\begin{aligned} {}_r\Delta_m^j \delta\breve{\phi} &= \delta\breve{\phi}_r^{\,j} - \delta\breve{\phi}_m^{\,j} \\ &= {}_r\Delta_m \delta\breve{\beta}_\phi^{Rx} + {}_r\Delta_m^j \varepsilon_{\delta\tilde{\phi}} \end{aligned} \tag{4.16}$$

Therefore, the receiver clock offset between stations can be estimated using all measurements of common visible satellite as following equation. n is the number of common visible satellites of two reference stations.

$${}_r\Delta_m \delta\hat{\beta}_\phi^{Rx} = \frac{1}{n}\sum_{j=1}^{n} {}_r\Delta_m^j \delta\breve{\phi} = {}_r\Delta_m \delta\breve{\beta}_\phi^{Rx} + \frac{1}{n}\sum_{j=1}^{n} {}_r\Delta_m^j \varepsilon_{\delta\tilde{\phi}} \tag{4.17}$$

Finally, all CPC measurements for each reference station are synchronized to the receiver clock offset of master station using estimated relative receiver clock value.

$$\begin{aligned}\delta\bar{\phi}_r^{\,j} &= \delta\breve{\phi}_r^{\,j} - {}_r\Delta_m\delta\hat{\beta}_\phi^{Rx} \\ &= -\left(\delta b + \beta_\phi^{Tx}\right)^j + \left(\delta\breve{\beta}_\phi^{Rx}\right)_m + \lambda N_m^j + \left(\varepsilon_{\delta\bar{\phi}}\right)_r^j\end{aligned} \tag{4.18}$$

4.2.4 Averaging Filter of Satellite CPC Correction

For each visible satellite, the satellite clock error, the integer ambiguity, and the receiver clock offset contained in the CPC measurements of equation (4.18) have the same values in all reference stations. Therefore, the satellite CPC corrections can be smoothed using the simple averaging filter as follow equation. M is the number of reference stations used in averaging.

$$\begin{aligned}\delta\hat{\phi}^j &= \frac{1}{M}\sum_{k=1}^{M}\delta\bar{\phi}_k^{\,j} \\ &= -\left(\delta b + \beta_\phi^{Tx}\right)^j + \left(\delta\breve{\beta}_\phi^{Rx}\right)_m + \lambda N_m^j + \left(\varepsilon_{\delta\hat{\phi}}\right)^j\end{aligned} \tag{4.19}$$

This algorithm can theoretically reduce the noise covariance of satellite CPC corrections by inversely proportional to the number of reference stations M as follow.

$$\sigma^2\left(\delta\hat{\phi}\right) = \frac{1}{M}\sigma^2\left(\delta\bar{\phi}\right) \tag{4.20}$$

Through the above process, the multi-station based satellite CPC corrections for five linear-combinations are generated as shown in following equations. These satellite CPC corrections $\delta\hat{\phi}$ can be continuously generated even when a particular reference station is breakdown.

$$\delta\hat{\phi}_{EWL} = -\beta^{Tx}_{\phi_{EWL}} + \delta\breve{\beta}^{Rx}_{\phi_{EWL}} + \lambda_{(0,1,-1)}N_{(0,1,-1)} + \varepsilon_{\delta\hat{\phi}_{EWL}} \quad \textbf{(4.21)}$$

$$\delta\hat{\phi}_{WL1} = -\beta^{Tx}_{\phi_{WL1}} + \delta\breve{\beta}^{Rx}_{\phi_{WL1}} + \lambda_{(1,-1,0)}N_{(1,-1,0)} + \varepsilon_{\delta\hat{\phi}_{WL1}} \quad \textbf{(4.22)}$$

$$\delta\hat{\phi}_{NL1} = -\left(\delta b + \beta^{Tx}_{\phi_{NL1}}\right) + \delta\breve{\beta}^{Rx}_{\phi_{NL1}} + \lambda_{(77,-60,0)}N_{(77,-60,0)} + \varepsilon_{\delta\hat{\phi}_{NL1}} \quad \textbf{(4.23)}$$

$$\delta\hat{\phi}_{NL2} = -\left(\delta b + \beta^{Tx}_{\phi_{NL2}}\right) + \delta\breve{\beta}^{Rx}_{\phi_{NL2}} + \lambda_{(154,0,-115)}N_{(154,0,-115)} + \varepsilon_{\delta\hat{\phi}_{NL2}} \quad \textbf{(4.24)}$$

$$\delta\hat{\rho}_{IF} = -\left(\delta b + \beta^{Tx}_{\rho_{IF}}\right) + \delta\breve{\beta}^{Rx}_{\rho_{IF}} + \varepsilon_{\delta\hat{\rho}_{IF}} \quad \textbf{(4.25)}$$

4.2.5 Ambiguity Re-Initialization and Message Generation

This is the last step to generate messages about satellite CPC corrections. In order to reduce the absolute volume of messages and prevent the roll-over, the integer ambiguity is re-initialized similarly to the compact RTK protocol. The initial ambiguity can be estimated by integer rounding method.

$$\hat{N}_{(0,1,-1)} = round\left(\frac{\delta\hat{\phi}_{EWL}}{\lambda_{(0,1,-1)}}\right) \quad \textbf{(4.26)}$$

$$\hat{N}_{(1,-1,0)} = round\left(\frac{\delta\hat{\phi}_{WL1}}{\lambda_{(1,-1,0)}}\right) \quad \textbf{(4.27)}$$

$$\hat{N}_{(77,-60,0)} = round\left(\frac{\delta\hat{\phi}_{NL1} - \delta\hat{\rho}_{IF}}{\lambda_{(77,-60,0)}}\right) \quad \textbf{(4.28)}$$

The integer ambiguity for each frequency is roughly estimated by the following equation. The remaining error of integer ambiguity is not a problem since it is absorbed by the user observations.

$$\begin{bmatrix} \hat{N}_{(1,0,0)} \\ \hat{N}_{(0,1,0)} \\ \hat{N}_{(0,0,1)} \end{bmatrix} = round\left\{ \begin{bmatrix} 0 & 1 & -1 \\ 1 & -1 & 0 \\ 77 & -60 & 0 \end{bmatrix}^{-1} \begin{bmatrix} \hat{N}_{(0,1,-1)} \\ \hat{N}_{(1,-1,0)} \\ \hat{N}_{(77,-60,0)} \end{bmatrix} \right\} \tag{4.29}$$

Finally, the five satellite CPC corrections for compact WARTK system called CPC-EWL, CPC-WL, CPC-NL1, CPC-NL2, and CPC-PRIF are generated as following equations. The sign of corrections are set to eliminate the satellite clock errors by adding correction to user measurements.

$$\begin{aligned} CPC_{EWL} &= -\delta\hat{\phi}_{EWL} + \lambda_{(0,1,-1)}\hat{N}_{(0,1,-1)} \\ &= \beta^{Tx}_{\phi_{EWL}} - \delta\breve{\beta}^{Rx}_{\phi_{EWL}} - \lambda_{(0,1,-1)}\delta N_{(0,1,-1)} \end{aligned} \tag{4.30}$$

$$\begin{aligned} CPC_{WL1} &= -\delta\hat{\phi}_{WL1} + \lambda_{(1,-1,0)}\hat{N}_{(1,-1,0)} \\ &= \beta^{Tx}_{\phi_{WL1}} - \delta\breve{\beta}^{Rx}_{\phi_{WL1}} - \lambda_{(1,-1,0)}\delta N_{(1,-1,0)} \end{aligned} \tag{4.31}$$

$$\begin{aligned} CPC_{NL1} &= -\delta\hat{\phi}_{NL1} + \lambda_{(77,-60,0)}\hat{N}_{(77,-60,0)} \\ &= \left(\delta b + \beta^{Tx}_{\phi_{NL1}}\right) - \delta\breve{\beta}^{Rx}_{\phi_{NL1}} - \lambda_{(77,-60,0)}\delta N_{(77,-60,0)} \end{aligned} \tag{4.32}$$

$$\begin{aligned} CPC_{NL2} &= -\delta\hat{\phi}_{NL2} + \lambda_{(154,0,-115)}\hat{N}_{(154,0,-115)} \\ &= \left(\delta b + \beta^{Tx}_{\phi_{NL2}}\right) - \delta\breve{\beta}^{Rx}_{\phi_{NL2}} - \lambda_{(154,0,-115)}\delta N_{(154,0,-115)} \end{aligned} \tag{4.33}$$

$$\begin{aligned} CPC_{PRIF} &= -\delta\hat{\rho}_{IF} \\ &= \left(\delta b + \beta^{Tx}_{\rho_{IF}}\right) - \delta\breve{\beta}^{Rx}_{\rho_{IF}} \end{aligned} \tag{4.34}$$

4.3 Correction Performance Analysis Results

4.3.1 Feasibility Test Environments

A preliminary test for performance analysis was conducted on Midwest and south USA. The six reference stations (GRTN, KNTN, NCSO, NCFF, ARMO, WINL), which is currently managed by the NOAA, are selected for WRS of compact WARTK system. All stations have a Trimble NetR9 receiver connected with a Trimble zephyr antenna. Table 3.1 summarizes the location of antenna reference point of each WRS, and Table 3.2 lists the types of receiver and antenna. The GRTN station is chosen as a master WRS, and five other stations are assigned to auxiliary WRS. Their baseline distance are 198 km to 921 km. The compact WARTK user for feasibility test is chosen the SIDN station located in target service area. Their locations are shown in Figure 4.7.

Figure 4.7 Locations of WRS and user for preliminary test

The real observed data for GPS triple-frequency pseudorange and carrier-phase measurements were collected with 1 second intervals on January 24th, 2019. Figure 4.8 represents the satellite geometry during the test time in user stations. The red lines mean dual-frequency satellites of block IIR or IIRM, the blue lines mean triple-frequency satellites of block IIF. The position dilution of precision (DOP) value of user is about 1.76. Table 4.3 summarizes the feasibility test environments.

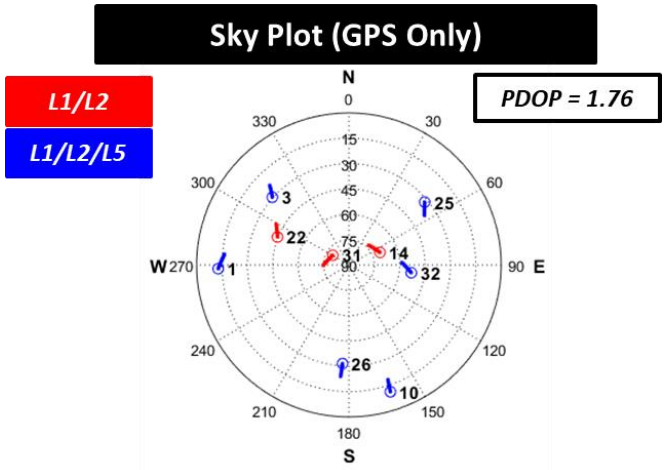

Figure 4.8 Sky plot on 24 January 2019 (GPS-Only)

Table 4.3 Summary of feasibility test environments

Date of Test	January 24th, 2019
Time	UTC 17:46:40 ~ 18:03:19 (1000 epochs)
Interval	1 sec
WRS Sites	6 WRSs (GRTN, KNTN, NCSO, NCFF, ARMO, WINL)
User Sites	1 User (SIDN)
Receiver Type	Trimble NetR9
Constellation	GPS Only (L1/L2/L5 signals) – 9 visible satellites

4.3.2 Comparison of RTK Correction Protocol

The conventional RTCM RTK correction and compact RTK correction are generated using the measurements of master station only. The compact WARTK correction is generated using the measurements of all six WRSs. Figure 4.9 shows the RTCM RTK correction for L1 carrier phase. As we can see in the figure, it has very large value of 10^7 meter level. On the other hand, the compact RTK correction for L1 carrier phase, represented in Figure 4.10, has small value with slow linearly variation over time since it does not contain geometry distance and receiver clock offset. Figure 4.11 shows the satellite CPC-NL1 correction for compact WARTK system. The proposed correction protocol has the smallest correction size and rate-of-change because it does not contain ionospheric and tropospheric delay. It contains only satellite clock related term and it is almost constant. The smaller the rate-of-change of corrections, the more robust the communication delay problem.

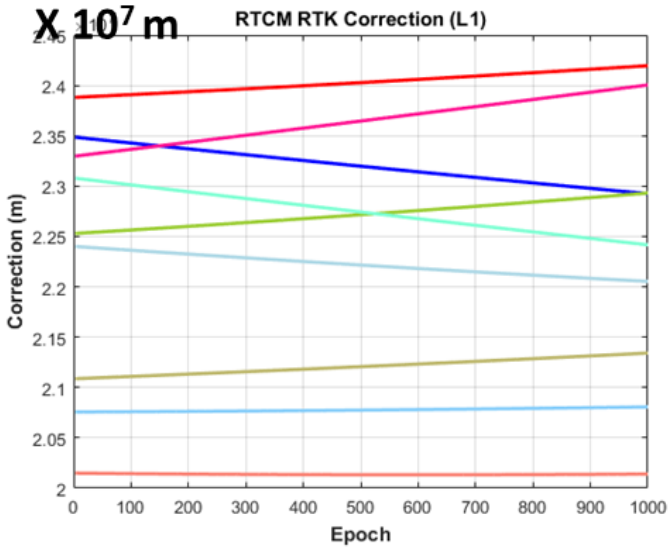

Figure 4.9 RTCM RTK L1 carrier-phase correction (MT 1004)

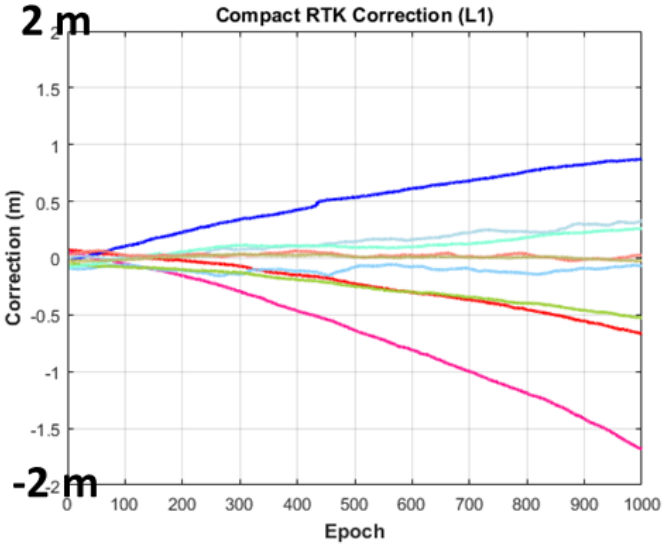

Figure 4.10 Compact RTK L1 carrier-phase corrections (MT 4081)

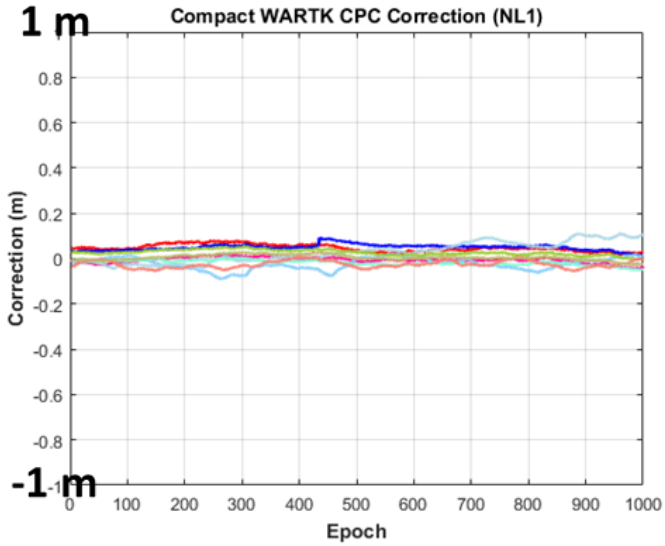

Figure 4.11 Compact WARTK CPC-NL1 corrections

The noise quality of each correction protocol were analyzed by triple-time-difference method [113]. Figure 4.12 shows the analysis results. The RTCM RTK correction, which is a raw observation, has the largest noise level. On the other hand, the noise level of compact WARTK correction is smaller than the compact RTK protocol smoothed by itself using a correction generation filter. Since the compact WARTK corrections are computed using the measurements of multiple station all together, the noise quality is effectively improved. Furthermore, it is possible to continuously provide the corrections to users even when a particular WRS is breakdown.

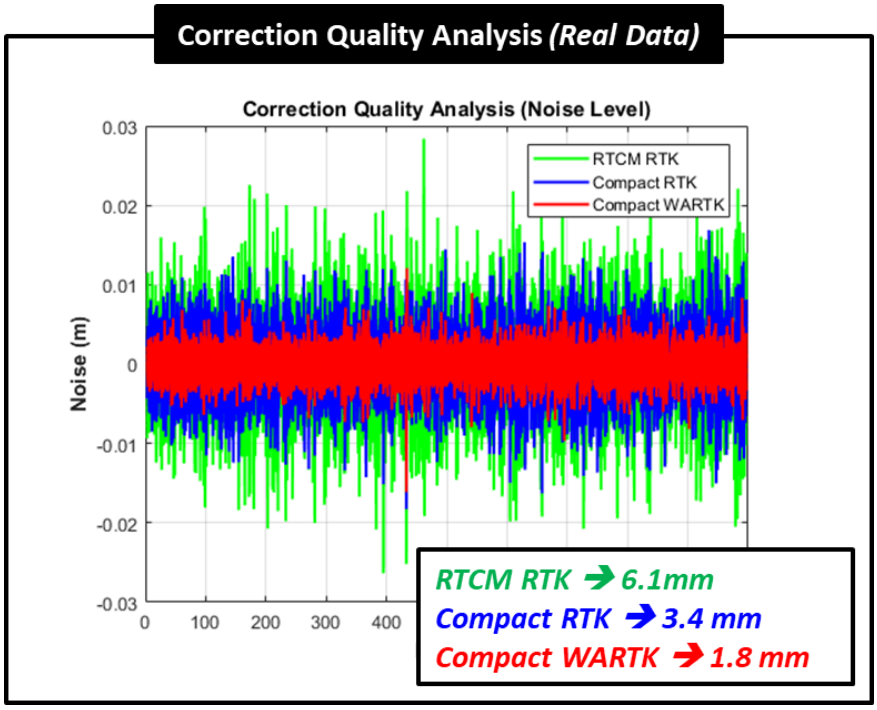

Figure 4.12 Noise quality analysis of RTK correction protocols

4.3.3 Latency Compensation Performance Analysis

The latency compensation performance analysis was conducted by intentionally inducing time delay to verify the robustness of the newly proposed compact WARTK corrections under communication outage. Each RTK correction protocol uses appropriate compensation methods to reduce the latency error in the communication outage environment, as shown in Figure 4.4. The RTCM RTK correction applied 3-state Kalman filter method for latency compensation [114], and the compact RTK correction compensates the latency through 1st order extrapolation using the range-rate correction [13]. The compact WARTK correction does not need any latency compensation method since it has almost linear and constant value.

- 3-state Kalman filter method for RTCM RTK correction:

$$\hat{\phi}(t_k) = \phi(t_1) + \dot{\phi}(t_1)\cdot(t_k - t_1) + \frac{1}{2}\ddot{\phi}(t_1)\cdot(t_k - t_1)^2 \qquad \textbf{(4.35)}$$

- 1st order linear extrapolation of compact RTK correction:

$$\delta\hat{\phi}(t_k) = \delta\phi(t_1) + \delta\dot{\phi}(t_1)\cdot(t_k - t_1) \qquad \textbf{(4.36)}$$

- No need to extrapolation for compact WARTK correction:

$$\delta\hat{\phi}(t_k) = \delta\hat{\phi}(t_1) \qquad \textbf{(4.37)}$$

where

t_1: transmission time of correction

t_k: received time of correction (current time)

Figure 4.13 shows the RMS residual errors of each correction protocol after latency compensation. The green line represents the RTCM RTK, the blue line means the compact RTK, and the red line means the compact WARTK. As can be seen from the results, the RTCM RTK shows rapid degradation when communication outage. The RTK service is not available even if the corrections is delayed for only 10 seconds. The compact RTK protocol, on the other hands, is more robust against latency than the RTCM RTK. It can maintain the RTK service until 30 seconds latency. The compact WARTK enables continuous service even when the satellite CPC correction is interrupted for significant time delay. The residual error is not exceeds the half-cycle threshold even 120 seconds latency. The latency analysis results are summarized in Table 4.4. Consequently, the compact WARTK can reduce error by 99% and 82% compared to RTCM RTK and compact RTK protocol in 60 seconds latency, respectively.

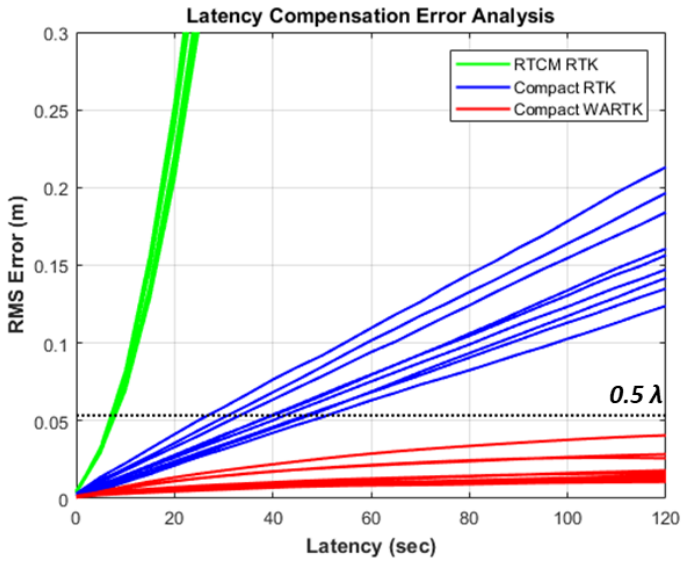

Figure 4.13 RMS residual errors after latency compensation

Table 4.4 Statistics of RMS residual errors after latency compensation

Latency (sec) $\Delta t = t_k - t_1$	RTCM RTK	Compact RTK	Compact WARTK
10	7.4 cm	1.5 cm	0.5 cm
30	45.6 cm	4.2 cm	1.0 cm
60	172.5 cm	8.2 cm	1.5 cm

Figure 4.14 shows the double-differenced residual errors in user range domain. We assume that geometry distance and integer ambiguity have been removed as true values obtained from RTK post-processing. Under normal circumstances without latency in corrections, the residual errors of all RTK protocols show good performance. Under 60 seconds correction latency circumstances, the user residual errors in the RTCM RTK and the compact RTK exceed the half-cycle threshold; that is, the RTK positioning is failed. On the other hand, the compact WARTK still shows good enough performance under the 60 seconds latency. Consequently, the satellite CPC corrections of compact WARTK protocol has superior performance under communication delay and outage.

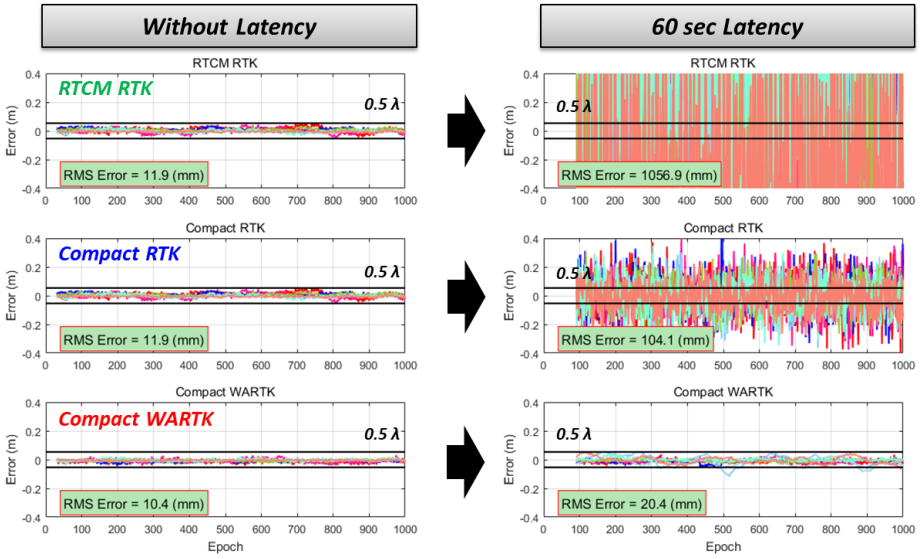

Figure 4.14 Latency effect in user double-differenced range domain

4.3.4 Message Data Bandwidth Analysis

It is possible to design the messages for satellite CPC corrections of compact WARTK as shown in the Table 3.13 because the absolute size of the corrections is small enough and is very robust in communication latency. Unlike the RTCM RTK and compact RTK protocol, which requires broadcasting correction every 1~2 seconds on average, the compact WARTK can be fully serviced without severe performance degradation even at update intervals of 5 seconds or more. Based on Table 4.1 (RTCM RTK), Table 4.2 (compact RTK), and Table 3.13 (compact WARTK), the required data amount of messages for each RTK correction protocol was analyzed. The RTCM RTK and compact RTK are assumed to broadcast corrections for the L5 frequency.

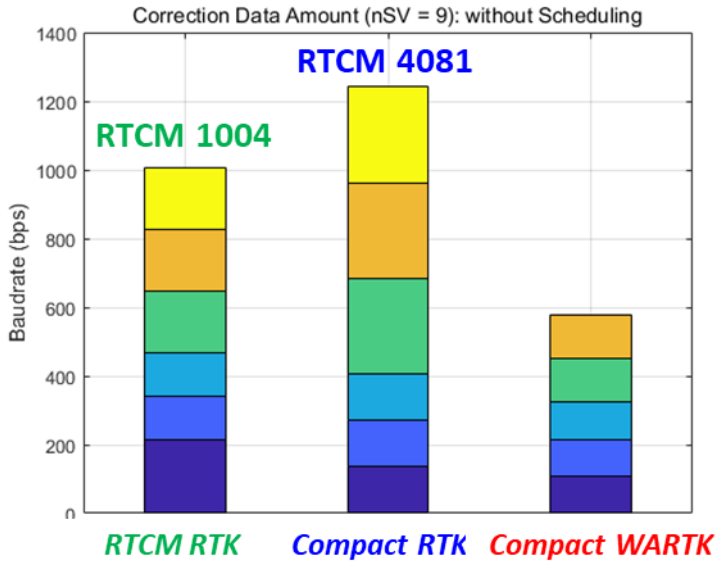

Figure 4.15 Message data mount for 9 visible satellites without scheduling

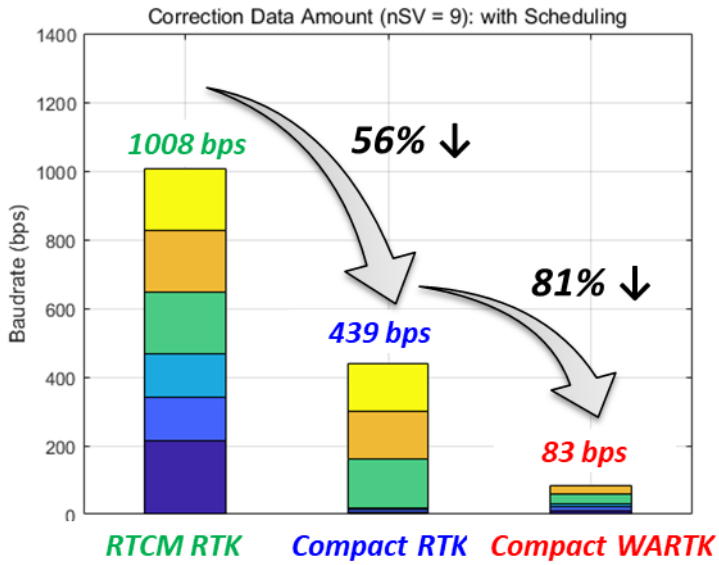

Figure 4.16 Message data mount for 9 visible satellites with scheduling

Legend	RTCM RTK	Compact RTK	Compact WARTK
	L1 PR	L1 PRC	CPC-PRIF
	L2 PR	L2 PRC	CPC-EWL
	L5 PR	L5 PRC	CPC-WL1
	L1 CP	L1 CPC+CPRC	CPC-NL1
	L2 CP	L2 CPC+CPRC	CPC-NL2
	L5 CP	L5 CPC+CPRC	-

Figure 4.17 Color legend for Figure 4.15 and Figure 4.16

Figure 4.15 shows the message data amount for 9 visible satellites without scheduling, and Figure 4.16 represents the message data amount for 9 visible satellites with scheduling. Figure 4.17 shows the color legend for Figure 4.15 and Figure 4.16. Only the message data amount for field of corrections was calculated, excluding the header and other additional information. As a results, the five satellite CPC corrections of compact WARTK system requires only 83 bps for 9 visible satellites with propriety scheduling. The message data amount for compact WARTK is dramatically reduced about 81% comparing to compact RTK protocol. In conclusion, the satellite CPC corrections can be broadcasted via GEO satellite which has very low-speed data link about 250 bps. Furthermore, it is possible to fully expand for multi-GNSS satellite CPC corrections.

Intentionally Blank Page

CHAPTER 5. TROPOSPHERIC CORRECTION GENERATION ALGORITHM

5.1 Former Research of Tropospheric Correction

The high-accuracy modeling of tropospheric delay is one of the important issues for centimeter-level positioning. Over the past few decades, a number of modeling methods for tropospheric delay have been studied. Typically, there are meteorological models such as the Saastmoinen model that require observed weather data [115], and empirical models such as UNB3 model that do not require any additional data [116]. Currently, the SBAS users of meter-level accuracy compute their own tropospheric delay using the UNB3 model whose accuracy is statistically about 12 cm [63]. However, the accuracy of these models is not sufficient to provide centimeter-level positioning service.

As an alternative to these models, precise tropospheric corrections estimated using carrier-phase observations of GPS reference stations are being applied to the centimeter-level navigation systems such as network RTK and PPP-RTK. The network RTK generates the scalar-type corrections for slant tropospheric delay, while the PPP-RTK generated the vector-type corrections for zenith tropospheric delay. In this section, the tropospheric corrections of the SBAS, network RTK, and PPP-RTK are introduced.

5.1.1 Tropospheric Corrections for SBAS

The SBAS users calculate their slant tropospheric delay using the UNB3 model based on empirical meteorological data without any additional data and sensors. In order to simply model the tropospheric delay, the UNB3 model provide the five surface meteorological parameters: pressure [P (mbar)], temperature [T (K)], water vapor pressure [e (mbar)], temperature lapse rate [β (K/m)], and water vapor lapse rate [λ (dimensionless)]. The zenith tropospheric delay (ZTD) can be simply computed from the height of receiver and these meteorological parameters [63], [116].

Table 5.1 Meteorological parameters for SBAS tropospheric model [63]

	Average				
Latitude (°)	P_0 *(mbar)*	T_0 *(K)*	e_0 *(mbar)*	β_0 *(K/m)*	λ_0
15° or less	1013.25	299.65	26.31	6.30e-3	2.77
30	1017.25	294.15	21.79	6.05e-3	3.15
45	1015.75	283.15	11.66	5.58e-3	2.57
60	1011.75	272.15	6.78	5.39e-3	1.81
75° or greater	1013.00	263.65	4.11	4.53e-3	1.55
	Seasonal Variation				
Latitude (°)	ΔP *(mbar)*	ΔT *(K)*	Δe *(mbar)*	$\Delta\beta$ *(K/m)*	$\Delta\lambda$
15° or less	0.00	0.00	0.00	0.00e-3	0.00
30	-3.75	7.00	8.85	0.25e-3	0.33
45	-2.25	11.00	7.24	0.32e-3	0.46
60	-1.75	15.00	5.36	0.81e-3	0.74
75° or greater	-0.50	14.50	3.39	0.62e-3	0.30

Table 5.1 represents the look-up table for five meteorological parameters for SBAS tropospheric delay. The values of each five parameters are calculated using the appropriate interpolation algorithm according to the receiver's latitude and day-of-year using the average and seasonal variation values given in look-up table [63]. The zero-altitude zenith hydrostatic delay (ZHD) and zenith wet delay (ZWD) are calculated as follows. The hydrostatic delay depends on the pressure, and wet delay is affected by the water vapor pressure and temperature.

$$ZHD_0 = \frac{10^{-6} k_1 R_d}{g_m} \cdot P \quad \textbf{(5.1)}$$

$$ZWD_0 = \frac{10^{-6} k_2 R_d}{g_m(\lambda + 1) - \beta R_d} \cdot \frac{e}{T} \quad \textbf{(5.2)}$$

where

k_1 = 77.604 K/mbar

k_2 = 382000 K^2/mbar

R_d = 287.054 J/(kg · K)

g_m = 9.784 m/s^2

The zenith hydrostatic and wet delay of the receiver's height H can be calculated as following equations. Here the height H is units of meters above mean-sea-level, and computed by the difference between ellipsoidal height of WGS-84 and geoid height of EGM-96 model [63]. g is surface gravity of 9.80665 m/s^2.

$$ZHD_H = \left(1 - \frac{\beta H}{T}\right)^{\frac{g}{R_d \beta}} \cdot ZHD_0 \quad \textbf{(5.3)}$$

$$ZWD_H = \left(1 - \frac{\beta H}{T}\right)^{\frac{(\lambda+1)g}{R_d \beta} - 1} \cdot ZWD_0 \quad \textbf{(5.4)}$$

Finally, the tropospheric corrections (TC) for slant tropospheric delay of users can calculated as follows,

$$TC = -\left(ZHD_H + ZWD_H\right) \cdot m(El) \quad \textbf{(5.5)}$$

with the simplified mapping function $m(El)$ for elevation angle El .

$$m(El) = \frac{1.001}{\sqrt{0.002001 + \sin^2(El)}} \quad \textbf{(5.6)}$$

5.1.2 Tropospheric Corrections of Network RTK

The scalar-type corrections of MAC-based network RTK system consist of two types: master station corrections (or observations) and MAC corrections needed for reducing spatial decorrelation error. The master station generates its carrier-phase corrections as the form of observation-based RTK protocol (RTCM MT 1004) or correction-based RTK protocol (RTCM MT 4081). In addition, the network RTK system produces the MAC corrections that are computed by single-differenced observations between the master and the auxiliary station. The detailed generation procedure of the network RTK corrections is described the Park (2008) [3] and Song (2016) [4].

- Carrier-phase corrections of master station:

$$\delta\phi_m^j = \delta R_m^j - \left(\delta b + \beta_\phi^{Tx}\right)^j - I_m^j + T_m^j + B_m + \lambda N_m^j + \varepsilon_{\delta\phi} \quad \textbf{(5.7)}$$

- MAC corrections of network RTK:

$$ {}_r\Delta_m^j \delta\hat{\phi} = {}_r\Delta_m^j \left(\delta R - I + T\right) + {}_r\Delta_m^{ref} \left(B + \lambda N\right) + \varepsilon_{\Delta\delta\hat{\phi}} \quad \textbf{(5.8)}$$

where the subscripts m and r represent the master station index and the auxiliary station index, respectively. The superscript j and ref represents the visible satellite index and reference satellite index, respectively.

Generally, the corrections of network RTK in the form of scaler observations is not divided into each error component; however, the MAC corrections can be divided into the dispersive and non-dispersive components using dual- or triple-frequency signals. The dispersive component contains the ionospheric delay error, and the non-dispersive component contains the satellite orbit error and tropospheric delay error. They are broadcast on MT 1015 and MT 1016 of RTCM version 3 with different update interval, respectively.

- Dispersive MAC corrections (MT 1015):

$$ {}_r\Delta_m^j \delta\hat{\phi}_{disp} = \frac{1}{\gamma - 1} \cdot {}_r\Delta_m^j \delta\hat{\phi}_{L1} - \frac{1}{\gamma - 1} \cdot {}_r\Delta_m^j \delta\hat{\phi}_{L2} \quad \textbf{(5.9)}$$

- Non-dispersive MAC corrections (MT 1016):

$$ {}_r\Delta_m^j \delta\hat{\phi}_{non-disp} = \frac{\gamma}{\gamma - 1} \cdot {}_r\Delta_m^j \delta\hat{\phi}_{L1} - \frac{1}{\gamma - 1} \cdot {}_r\Delta_m^j \delta\hat{\phi}_{L2} \quad \textbf{(5.10)}$$

The network RTK users properly interpolate these network RTK corrections to user locations for eliminating their slant tropospheric delay with other GNSS error sources together.

$$\delta\hat{\phi}_u^j = \delta\phi_m^j + \sum_{k=1}^{m-1} w_k \cdot {}_k\Delta_m^j \delta\hat{\phi} \tag{5.11}$$

where

$$\sum_{k=1}^{m} w_k = 1 \tag{5.12}$$

The appropriate weighting w_k for user locations can be determined by various interpolation methods based on the distance between reference stations. Many correction interpolation methods for network RTK users have been proposed, such as the Distance-based linear Interpolation Method (DIM) [117], the Linear Interpolation Method (LIM) [118], the Linear Combination Model (LCM) [119], [120], and the Low-order Surface Model (LSM) [121] The DIM is a simple method based on inverse distance between reference stations and user. The LIM, LCM, and LSM are similar methods which are based on first-order surface modeling. According to Dai et al. (2003) [122], all of these methods aim to model the distance-dependent biases between the reference station and the user receiver, and the performance of these methods is similar. The interpolation methods based on Kriging are also proposed in a variety of ways [65], [123], [124]. Table 5.2 summarized the typical interpolation method for network RTK users.

Table 5.2 Summary of network RTK user interpolation methods

Interpolation methods	Brief descriptions
Distance-Based Linear Interpolation Method (DIM)	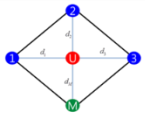 $w_i = \frac{\frac{1}{d_i}}{\sum_{j=1}^{3}\frac{1}{d_j}}$
Linear Combination Model (LCM)	$\sum_{i=1}^{n}\alpha_i = 1$, $\sum_{i=1}^{n}\alpha_i(X_u - X_i) = 0$, $\sum_{i=1}^{n}\alpha_i^2$ minimized; $\begin{bmatrix} 1 & 1 & \cdots & 1 & 1 \\ \Delta X_{1u} & \Delta X_{2u} & \cdots & \Delta X_{n-1u} & 0 \\ \Delta Y_{1u} & \Delta Y_{2u} & \cdots & \Delta Y_{n-1u} & 0 \end{bmatrix}}_{B} \underbrace{\begin{bmatrix} \alpha_1 \\ \alpha_2 \\ \vdots \\ \alpha_n \end{bmatrix}}_{\bar{\alpha}} = \underbrace{\begin{bmatrix} 1 \\ \Delta X_{un} \\ \Delta Y_{un} \end{bmatrix}}_{W}$, $\bar{\alpha} = B^T\left(BB^T\right)^{-1}W$
Linear Interpolation Model (LIM)	$V_{un} = a\cdot\Delta X_{1n} + b\Delta Y_{un}$, $V = \begin{bmatrix} V_{1,M} \\ V_{2,M} \\ \vdots \\ V_{n-1,M} \end{bmatrix} = \begin{bmatrix} \Delta X_{1,M} & \Delta Y_{1,M} \\ \Delta X_{2,M} & \Delta Y_{2,M} \\ \vdots & \vdots \\ \Delta X_{n-1,M} & \Delta Y_{n-1,M} \end{bmatrix} \cdot \begin{bmatrix} a \\ b \end{bmatrix} = A\begin{bmatrix} a \\ b \end{bmatrix} \Rightarrow \begin{bmatrix} \hat{a} \\ \hat{b} \end{bmatrix} = \left(A^TA\right)^{-1}A^TV$, $\therefore \hat{V}_{un} = \begin{bmatrix} \Delta X_{un} & \Delta Y_{un} \end{bmatrix}\begin{bmatrix} \hat{a} \\ \hat{b} \end{bmatrix}$
Low-order Surface Model (LSM)	$V = a\cdot\Delta X + b\cdot\Delta Y + c$ $V = a\cdot\Delta X + b\cdot\Delta Y + c\cdot\Delta H + d$ $V = a\cdot\Delta X + b\cdot\Delta Y + c\cdot\Delta H + d\cdot\Delta H^2 + e$

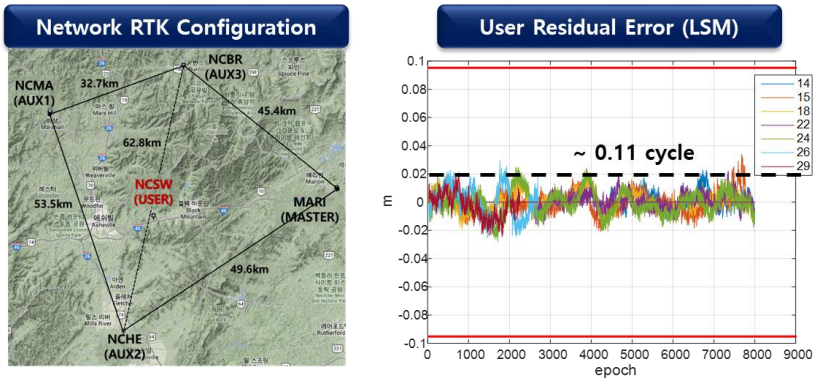

Figure 5.1 Network RTK user residual error by LSM interpolation [125]

Figure 5.1 shows the example of user residual error by LSM interpolation of network RTK corrections. The performance of network RTK user depends on the accuracy of these correction interpolation methods. The integer ambiguity can be correctly resolved by removing sufficient residual errors, including the tropospheric delay, through proper interpolation.

However, as conceptually shown in Figure 3.1, the interpolation method for the network RTK corrections are not sufficiently accurate for the user whose baseline distance is more than 70 km. In other words, the scalar-type corrections of the network RTK is not suitable for applying wide-area coverage because of the spatial correlated interpolation error. In particular, interpolation errors due to the tropospheric delay at satellite low-elevation angle are severe [65].

5.1.3 Tropospheric Corrections of PPP-RTK

A high-precision ZTD can be estimated using un-differenced pseudorange and carrier-phase measurements of single reference station through the PPP technique in real-time. The PPP technique estimates all GNSS error, including precise zenith tropospheric delay, state separately based on state-space functional and stochastic modeling of each error component [7], [49].

There are various state-space models for estimating precise ZTD. Generally, the hydrostatic component is removed by empirical model such as UNB3 model, and the remained wet component is estimated as the Kalman filter. The simplest stochastic model of tropospheric delay implemented in GIPSY-OASIS II software of Jet Propulsion Laboratory (JPL), and gLAB software of European Space Agency (ESA), the typical PPP software packages, is defined as following equations [126].

$$T(El) = T_{z,hyd} \cdot m_{hyd}(El) + T_{z,wet} \cdot m_{wet}(El) \quad \textbf{(5.13)}$$

$$T_{z,dry} = a \cdot e^{-bH} \quad \textbf{(5.14)}$$

$$T_{z,wet} = T_{z_0,wet} + \delta T_{z,wet} \quad \textbf{(5.15)}$$

where $a = 2.3m$, $b = 0.116 \cdot 10^{-3}$, $T_{z_0,wet} = 0.1m$, and H is the height above mean-sea-level in meters. $\delta T_{z,wet}$, which is the residual component of ZWD, is estimated as a random walk process in the PPP Kalman filter together with other state-space parameters [126]. $m_{hyd}(El)$ and $m_{wet}(El)$ are the hydrostatic and wet mapping function. Typically, Niell mapping function (NMF) [127] or Global mapping function (GMF) [128] are used for tropospheric estimation in real-time process. Vienna mapping function, which is based on numerical weather models, sometimes used in PPP post-processing [129].

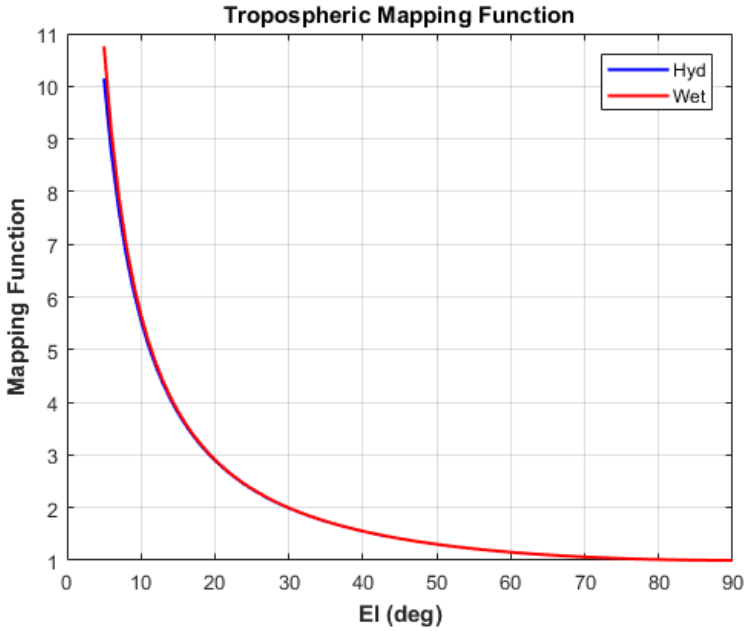

Figure 5.2 Niell mapping function with satellite elevation angle

There is a more advanced estimation model considering the horizontal tropospheric gradients, the azimuthal asymmetry of the local troposphere at observation site [130].

$$T(El) = T_{z,hyd} \cdot m_{hyd}(El) + T_{z,wet} \cdot m_{wet}(El) + m_{grad}(El) \cdot \left\{ G_N \cos(Az) + G_E \sin(Az) \right\} \quad \textbf{(5.16)}$$

The tropospheric gradient mapping function is expressed as follow.

$$m_{grad}(El) = \frac{1}{\sin(El)\tan(El) + 0.0032} \quad \textbf{(5.17)}$$

The G_N and G_E are the northern and eastern horizontal delay gradients that are estimated together with wet delay component from the PPP Kalman filter. This gradient model is adopted in CSRS-PPP developed by Natural Resources Canada (NRC), which is one of the post-processing online PPP service. The accuracy of ZTD estimation by CSRS-PPP is less than 1 cm with compare to IGS precise tropospheric product [126]. Figure 5.3 shows the ZTD estimation error of CSRS-PPP service with compare to the true reference value of ZTD from the UNAVCO COSMIC program. The estimation error is about RMS 5 mm. Therefore, the precise ZTD product from CSRS-PPP service can be considered as true reference data for accuracy analysis.

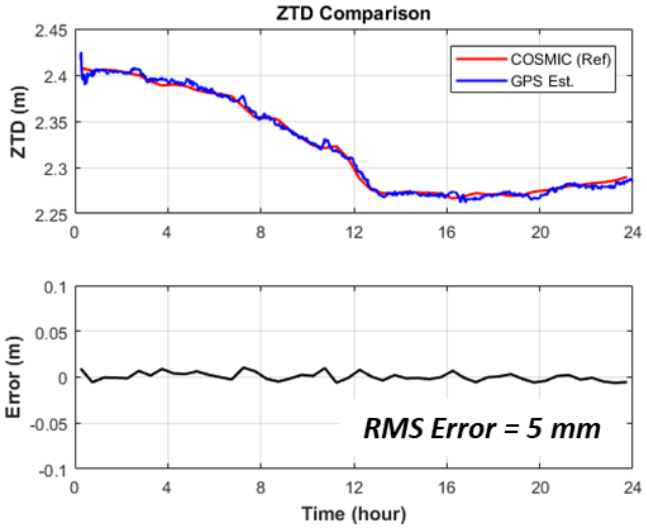

Figure 5.3 ZTD estimation error of CSRS-PPP service

The PPP-RTK system generates the precise zenith tropospheric corrections for nationwide service based on the PPP technique that accurately estimates ZTD in each reference stations. The precise tropospheric corrections are generated with dense GNSS reference station network distributed in 10~50 km units [7]. The carrier-phase based precise ZTD value of each station estimated from dense GNSS network is used to produce the zenith tropospheric corrections in two-dimensional surface. The tropospheric corrections of PPP-RTK is continuously discussed for RTCM standardization, and the message format is considering as the grid-based SSR corrections [12], [30]. Many research have been studied to generate grid-based tropospheric corrections. Typically, as shown in Figure 5.4, inverse distance weighting is used to interpolating ZTD measurements into predefined tropospheric grid points [131], [132]. Kriging method is another weighting method of generating grid-based tropospheric corrections [133].

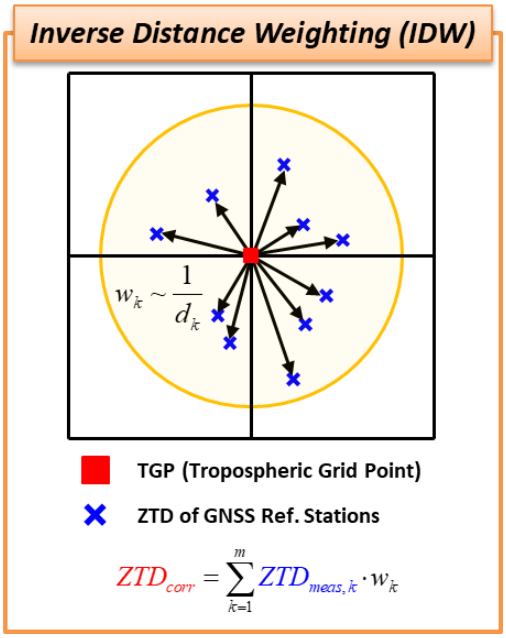

Figure 5.4 Inverse distance weighting for generating tropospheric correction

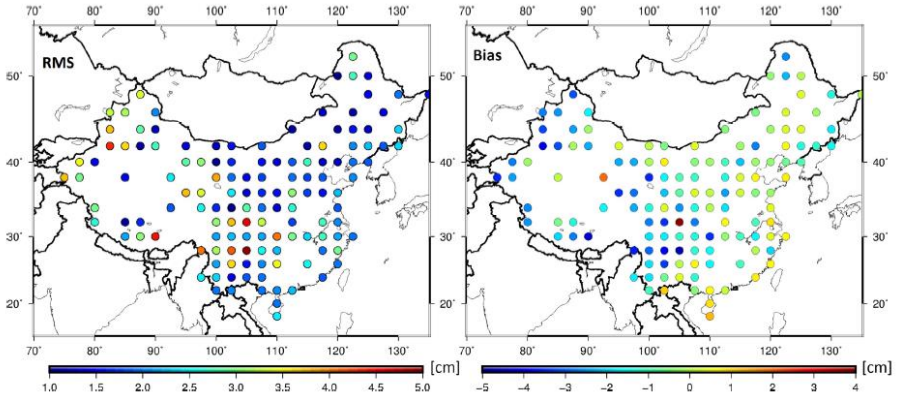

Figure 5.5 Accuracy of grid-based tropospheric corrections for China [132]

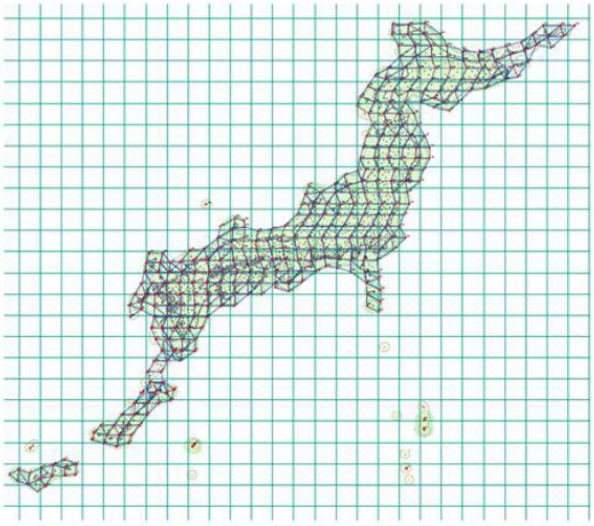

Figure 5.6 Preliminary design of tropospheric grid points for CLAS [25]

The PPP-RTK tropospheric corrections based on GPS dense network give the highest accuracy and the best continuity in real-time. For example, Figure 5.5 shows the accuracy results of zenith tropospheric corrections in China. Their product can provide real-time service with RMS accuracy of 1.8 cm. However, in order to provide the corrections for national or continental areas, the system requires a huge number of GNSS reference stations equipped with expensive permanent receivers. Furthermore, the larger the area of the service coverage, a large number of pre-defined tropospheric grid points are required. For example, Figure 5.6 shows the pre-defined grid points for QZSS CLAS service in Japan. The CLAS system generates its tropospheric corrections using more than 1,200 stations in Japan [25], and have 335 pre-allocated tropospheric grid points whose required message bandwidth is about 1,500 bps [30].

5.2 Tropospheric Correction Generation Algorithm

The accuracy of SBAS tropospheric models is not sufficient to provide centimeter-level positioning service. The network RTK corrections have the limitation of service coverage. The PPP-RTK tropospheric corrections have the disadvantage in cost of infrastructure and message data amounts. In order to overcome the limitations of former research, this thesis propose a new real-time tropospheric modeling technique for compact WARTK system.

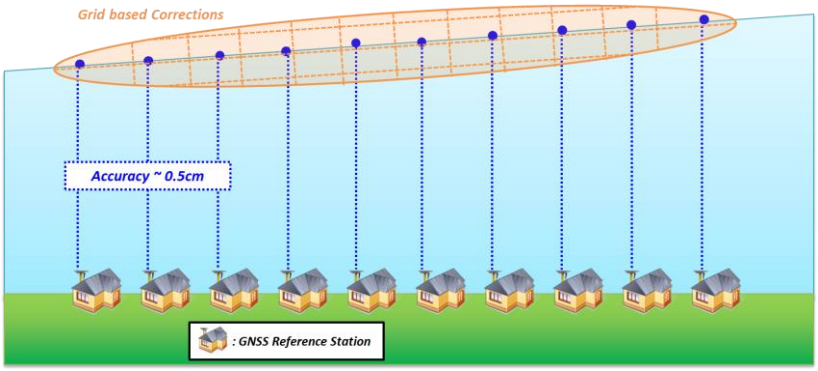

Figure 5.7 Concept of grid-based tropospheric correction (PPP-RTK)

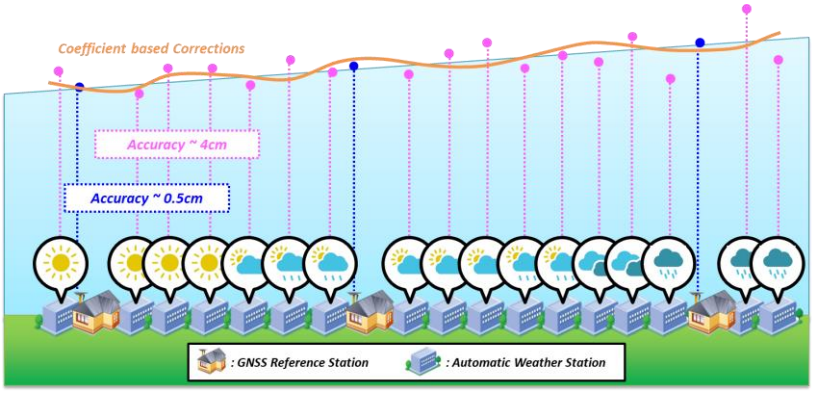

Figure 5.8 Concept of coefficient-based tropospheric correction with weather data (compact WARTK)

Figure 5.7 shows the conceptual figure of grid-based PPP-RTK corrections, which requires a huge number of reference stations. Figure 5.8 represents the concept to generate the tropospheric corrections for compact WARTK. In order to maintain accuracy of tropospheric corrections while dramatically reducing the number of reference stations required to generate the corrections, the automatic weather stations (AWS) are additionally used. AWS are already very densely installed in anywhere nationwide unlike GPS reference stations. The accuracy of tropospheric modeling based on weather data at each AWS is as low as about 4 cm [2], [134], [135]; however, it is possible to estimate high-accuracy tropospheric corrections with combining a small number of GNSS reference stations and a huge number of AWS together. In addition, the proposed algorithm adopts a spherical harmonics for modeling spatial properties of tropospheric delay and also for reducing message amount.

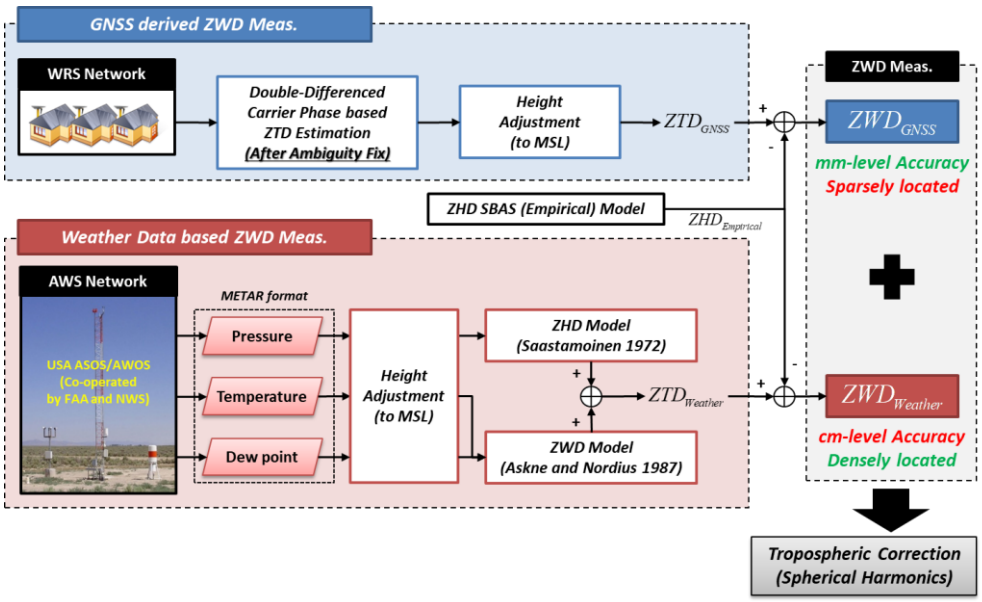

Figure 5.9 Overall processing diagram of ZWD measurements for compact WARTK tropospheric correction generation

Hydrostatic part of tropospheric delay has been modelled very well, while wet part is hard to empirically model. Therefore, the compact WARTK provides the corrections for zenith wet delay on mean-sea-level. Figure 5.9 shows the overall processing diagram for generating tropospheric corrections of compact WARTK. In this section, the detailed algorithm for generating tropospheric corrections is introduced.

5.2.1 ZWD Estimation Using Carrier-Phase Observations

Similar to PPP technique that uses un-difference observations, the precise zenith tropospheric delay of each WRS can be estimated from double-difference carrier-phase measurements. After eliminating hydrostatic and wet delay by SBAS model as a priori model, the NL ambiguity resolution process in the proposed TCAR method estimates the residual of zenith wet delay components $\delta T_{z,wet}$ as a random walk process of Kalman filter. The integer ambiguities are estimated together with zenith wet delay.

The residual of double-differenced wet delay in ionospheric-free observations can be expressed as following equation.

$$ {}^{j}_{r}\Delta\nabla^{ref}_{m}\delta T_{wet} = {}^{j}\nabla^{ref}_{r} m_{wet}\cdot\delta T_{z,wet,r} - {}^{j}\nabla^{ref}_{m} m_{wet}\cdot\delta T_{z,wet,m} \qquad \textbf{(5.18)} $$

where the subscripts m and r represent the master station index and the auxiliary station index, respectively. The superscript j and ref represents the visible satellite index and reference satellite index, respectively. Each double-differenced observation contains the two ZWD components for master station and

auxiliary station. Therefore, unlike PPP, which uses only one independent station, the system and observation equation for precise tropospheric estimation of each station should be established for multiple baselines. The system equation of geometry-based NL ambiguity resolution can be designed as follows.

$$
\begin{aligned}
&\dot{\bar{x}} = F\bar{x} + \Gamma\bar{w} \\
&\bar{x} = \begin{bmatrix} \bar{x}_N & \bar{x}_{tropo} \end{bmatrix}^T \qquad \bar{w} = \begin{bmatrix} \bar{w}_N & \bar{w}_{tropo} \end{bmatrix}^T \\
&F = \begin{bmatrix} F_N & O_{n\times m} \\ O_{m\times n} & F_{tropo} \end{bmatrix} \qquad \Gamma = \begin{bmatrix} I_{n\times n} & O_{n\times m} \\ O_{m\times n} & I_{m\times m} \end{bmatrix} \\
&F_N = O_{n\times n} \qquad F_{tropo} = O_{m\times m}
\end{aligned}
\tag{5.19}
$$

The observation equation can be designed as follows.

$$
\begin{aligned}
&\bar{z} = H\bar{x} + \bar{v} \qquad \bar{v} \sim W\left(0, R_{n\times n}\right) \\
&H = \begin{bmatrix} \lambda \cdot I_{n\times n} & H_{tropo} \end{bmatrix} \\
&H_{tropo} = \begin{bmatrix} \nabla_1\bar{m}_{wet} & 0 & 0 & 0 & -\nabla_m\bar{m}_{wet} \\ 0 & \nabla_2\bar{m}_{wet} & 0 & 0 & -\nabla_m\bar{m}_{wet} \\ 0 & 0 & \ddots & 0 & \vdots \\ 0 & 0 & 0 & \nabla_{m-1}\bar{m}_{wet} & -\nabla_m\bar{m}_{wet} \end{bmatrix}
\end{aligned}
\tag{5.20}
$$

The states of Kalman filter are consists of double-differenced integer ambiguity of all carrier-phase measurements, and the zenith wet delay of each WRS. n is the number of states for integer ambiguity that is the same number of carrier-phase observations. m is the number of states for zenith wet delay that is the same number of WRS.

After the integer ambiguity is correctly fixed, the precise ZWD value can be calculated. The estimation error of ZWD with fixed ambiguity were analyzed by simple simulation data. Figure 5.10 shows the results of single-baseline ZWD estimation, and Figure 5.11 represents the ZWD estimation error using multi-baseline's observations. As shown in the results, the precise ZWD for each WRS can be estimated when using multi-baseline observations all together. The convergence time will also be shortened.

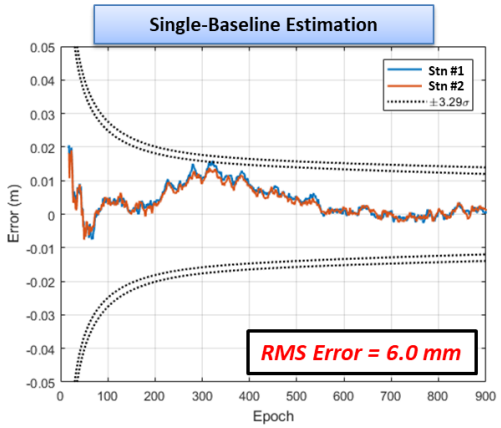

Figure 5.10 ZWD estimation by single-baseline (2 WRS)

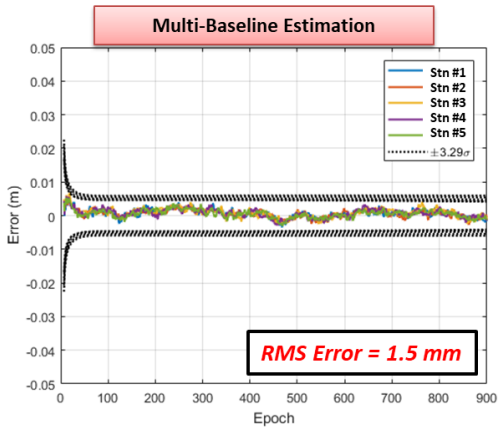

Figure 5.11 ZWD estimation by multi-baselines (5 WRS)

The precise ZTD value at each WRS location can be reconstructed using the estimated ZWD value and a priori ZHD value of SBAS empirical model. Finally, in order to obtain precise GNSS-derived ZWD measurements on mean-sea-level, the height adjustment should be processed as shown in Figure 5.12. One of the key considerations in tropospheric delay modeling is the correction for altitude. The tropospheric delay is characterized especially by height of reference stations. Generally, zenith tropospheric delay over height variation can be assume exponential function [125]. In this thesis, the inversion of equation (5.4), which is the SBAS empirical model, is adopted for adjusting ZWD measurements at station height H to mean-sea-level.

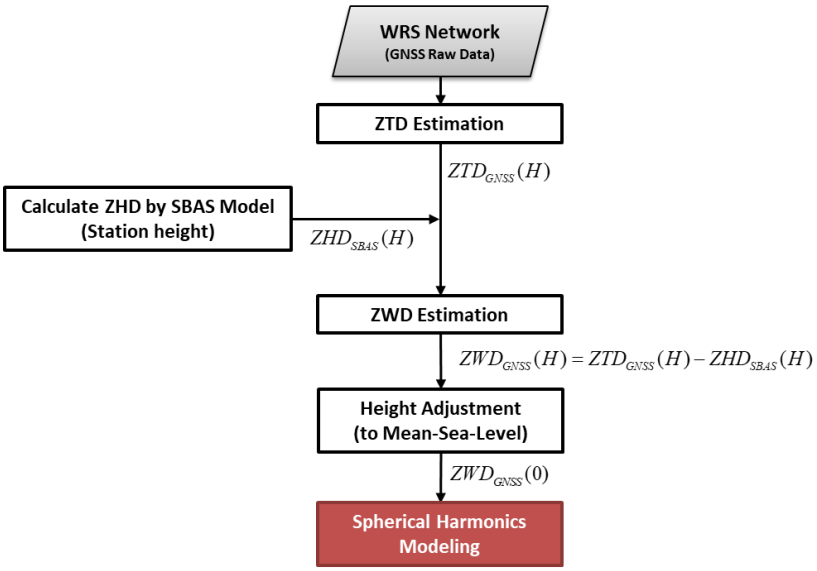

Figure 5.12 Data processing for GNSS-derived ZWD measurements

5.2.2 ZWD Measurements Using Weather Data

Figure 5.13 shows the data processing for obtaining weather data based ZWD measurements. It can be divided into three main stages: collecting meteorological data, data pre-processing including height adjustment, and calculating ZWD measurements. The detailed algorithm described as follows.

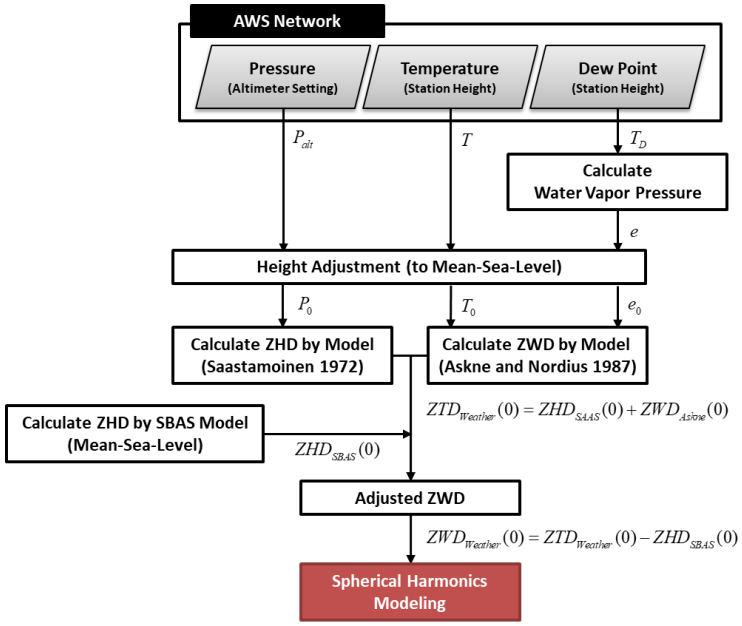

Figure 5.13 Data processing for weather data based ZWD measurements

1) Collecting Meteorological Data

Meteorological data needed to model tropospheric delay is the pressure, temperature, and dew point. The WPF of the compact WARTK system can collect these meteorological data from automatic weather station (AWS) densely distributed in nationwide such as automated surface weather observing system (ASOS) or automated weather observing system (AWOS).

The ASOS and AWOS, which are a joint effort of the National Weather Service (NWS), the Federal Aviation Administration (FAA), and the Department of Defense (DoD) in USA, are designed to support weather forecast activities, aviation operations, and meteorological and climatological research communities. The primary function of the ASOS and AWOS is to automatically collect temperature, dew point, pressure, wind direction and speed, and precipitation minute-by-minute. In addition, the system automatically provide the raw observing data as the basic Aviation Routine Weather Report (METAR) report [136]. Figure 5.14 shows an example of meteorological data by METAR report.

The ASOS is installed in area where manned observation is possible, while the AWOS is installed in such as mountain areas and, islands, etc. where it is difficult to manned observation. The AWOS serve as local weather observation system in area where ASOS is not installed. Figure 5.15 shows the weather sensors installed in commercial AWOS site. The ASOS contains additional weather sensors, including AWOS.

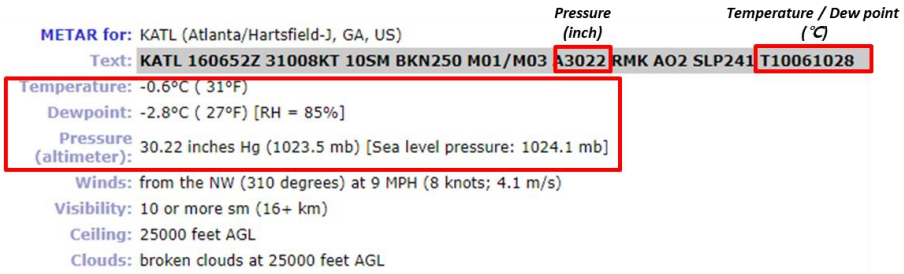

Figure 5.14 An example of meteorological data by METAR format

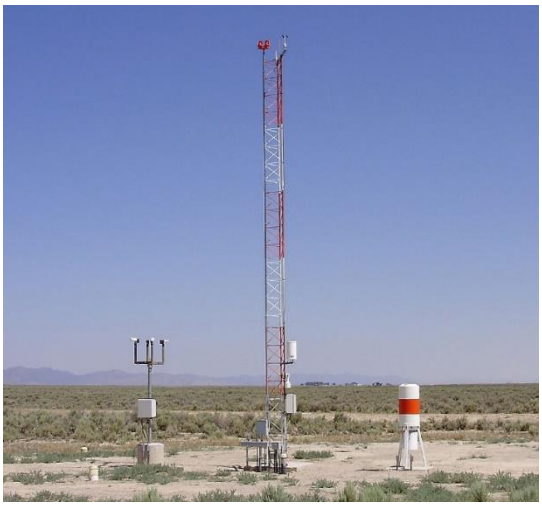

Figure 5.15 An example of AWOS site

2) Pre-Processing of Meteorological Data

The meteorological data of METAR format collected by ASOS and AWOS site is pre-processed to model the tropospheric delay at mean-sea-level. Especially, the height adjustment process to mean-sea-level for each weather data is essential since the raw observed data is the value at station height.

- Pressure

The ASOS and AWOS read the pressure in altimeter setting most commonly heard in radio and television broadcasts. It is not the true barometric pressure at a station. Instead, it is the pressure reduced to mean-sea-level using the temperature profile of the standard atmosphere. It is also slightly different from the mean-sea-level pressure, which uses observed conditions for pressure reducing rather than standard conditions [137].

The conversion method from the altimeter setting P_{alt} to the station pressure P is expressed as following equation. H is station orthometric height above the mean-sea-level in meter. The altimeter setting is measured in unit of inHg, and must be converted to unit of mbar (or hPa).

$$P = P_{alt} \times \left(1 - \frac{0.0065 \cdot H}{288}\right)^{5.2561} \quad \textbf{(5.21)}$$

- Temperature and dew point

The ASOS and AWOS measures the air temperature T and dew point T_D at station height H with unit of degrees Celsius (℃). These values must be converted to Kelvin (K). The temperature and dew point affect the wet part of tropospheric delay. The water (saturated) vapor pressure e (mbar) to calculate wet delay can be computed from dew point using the Berman's formula as follows [138], [139].

$$e = 6.108 \cdot \exp\left(\frac{17.1485T_D - 4684.1}{T_D - 38.45}\right) \quad \textbf{(5.22)}$$

- Data adjustment form station height to mean-sea-level

The pressure [P (mbar)], temperature [T (K)], and water vapor pressure [e (mbar)] at station height are adjust to mean-sea-level surface according to SBAS standard model based on ideal gas equation [63], [116]. H is station orthometric height above the mean-sea-level in meter.

$$T_0 = T + \beta H \tag{5.23}$$

$$P_0 = P\left(\frac{T_0}{T}\right)^{\frac{g}{R_d\beta}} = P\left(1+\frac{\beta H}{T}\right)^{\frac{g}{R_d\beta}} \tag{5.24}$$

$$e_0 = e\left(\frac{T_0}{T}\right)^{\frac{(\lambda+1)g}{R_d\beta}} = e\left(1+\frac{\beta H}{T}\right)^{\frac{(\lambda+1)g}{R_d\beta}} \tag{5.25}$$

where

R_d = 287.054 J/(kg · K)

g = 9.80665 m/s^2

The value of temperature lapse rate [β (K/m)] and water vapor lapse rate [λ (dimensionless)] can be obtained from the look-up table represented in Table 5.1 with interpolation algorithm according to the receiver's latitude and day-of-year.

3) Calculation of Zenith Tropospheric Delay Using Weather Data

A lot of tropospheric delay models based on gas equations have been studied over the past few decades. Generally, the hydrostatic component of tropospheric delay is mainly caused by atmosphere pressure, and the wet component is caused by temperature and water vapor pressure. In this study, the Saastamoinen model (1972) [115], which is revised by Davis et al. (1985) [140], is used to compute zenith hydrostatic delay, and the Askne and Nordius (1987) model [129], [141] is adopted to determine the zenith wet delay.

- Saastamoinen model (1972) for ZHD calculation:

$$ZHD = \frac{0.002277 \cdot P}{1 - 0.00266\cos 2\phi - 0.28 \cdot 10^{-6} \cdot h} \quad \textbf{(5.26)}$$

where

P : surface pressure (mbar)

ϕ : station latitude (rad)

h : station ellipsoidal height (m)

- Askne and Nordius model (1987) for ZWD calculation:

$$ZWD = 10^{-6} \cdot \left(k_3 / T_m + k_2^{'}\right) \cdot \frac{R_d \cdot e}{(\lambda + 1) g} \quad \textbf{(5.27)}$$

where

e : water vapor pressure (mbar)

λ : water vapor lapse rate (dimensionless)

T : temperature (K)

$T_m = 70.2 + 0.72 \cdot T$: weighted mean temperature (K)

$k_2^{'}$ = 16.522 K/mbar

k_3 = 377600 K^2/mbar

R_d = 287.054 J/(kg · K)

g = 9.80665 m/s^2

The refractivity constants $k_2^{'}$ and k_3 are empirically determined. The mean temperature weighted with water vapor pressure T_m is empirically modeled, and this study chose the appropriate model on mid-latitude area [134].

The ZHD components, which account for about 90% of the tropospheric delay, can be modeled very accurately within a few millimeters through a Saastamoinen model. On the other hand, the accuracy of ZWD model is typically 3~4 cm according to former research [2], [134], [135].

The accuracy of the Askne and Nordius model for ZWD was analyzed in the USA CONUS region using GPS-derived precise ZWD values and weather data provided by the UNAVCO COSMIC program on January 24th, 2019. Figure 5.16 shows the analysis results of ZWD model accuracy. The coefficient of linear correlation between the true precise ZWD and the modeled ZWD is 0.85, and the RMS error is about 4 cm. Consequently, the weather data based ZWD measurements whose accuracy is about 4 cm can be obtained from each AWS site.

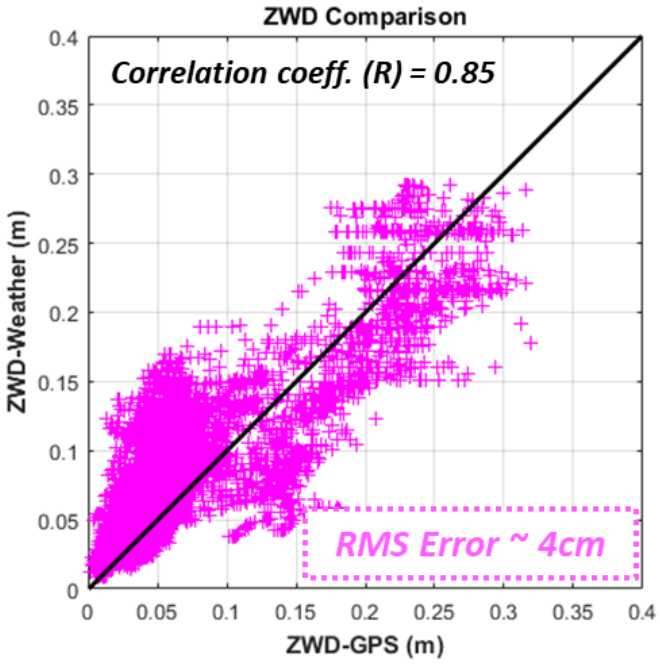

Figure 5.16 Accuracy of weather data based ZWD model

5.2.3 Correction Generation Using Spherical Harmonics

1) Spherical Harmonics Modeling

Spherical harmonics is a technique that models spatial data through a linear combination of basis functions that are orthogonal to each other [142]. Figure 5.17 shows the concept of spherical harmonics modeling. In the field of GPS, spherical harmonics modeling have been used to estimate satellite DCB [40] or ionospheric delay modeling [143]–[145]. It has also been used for the modeling of zenith tropospheric delay of the global world [146].

Spherical harmonics model is adopted in this study to generate precise tropospheric corrections. The spatial properties of zenith wet delay on mean-sea-level can be expressed as following spherical harmonics function.

$$\begin{aligned} ZWD_0(\phi,\lambda) &= \sum_{n=0}^{N}\sum_{m=0}^{n} P_{nm}(\sin(\phi))\cdot\{C_{nm}\cdot\cos(m\lambda)+S_{nm}\cdot\sin(m\lambda)\} \\ &\triangleq H_{SH}(\phi,\lambda)\cdot\bar{x}_{coeff} \end{aligned} \quad \textbf{(5.28)}$$

$$\bar{x}_{coeff} = \begin{bmatrix} C_{00} & \cdots & C_{NN} & S_{11} & \cdots & S_{NN} \end{bmatrix}^T \quad \textbf{(5.29)}$$

where

ZWD_0 : zenith wet delay on mean-sea-level (m)

ϕ : latitude (rad)

λ : longitude (rad)

P_{nm} : associated Legendre function

C_{nm}, S_{nm} : spherical harmonics coefficients

N : order and degree of spherical harmonics model

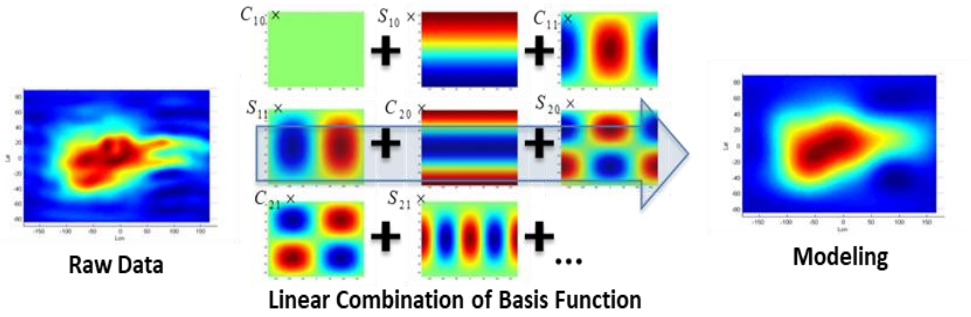

Figure 5.17 Concept of spherical harmonics modeling

Spherical harmonics differ in expressible resolution according to order and degree. The higher the degree, order, the more base functions can be used to model the data more accurately. However, the larger the degree and order, the higher the number of coefficients for base functions, the loss of message capacity. This study adopted 3rd order modeling, and 16 coefficients are estimating and broadcasting as the tropospheric corrections. The 1,000 km radius of the service target area in this study can be sufficiently modelled by 3rd order, although the order is also set to 10 or higher when modelled for the global world [146].

2) Observation Equation for Estimating Tropospheric Corrections

The WPF process generates high-precision zenith wet delay corrections in real-time combining the GNSS-derived ZWD measurements, the weather data-based ZWD measurements, and SBAS empirical model based ZWD measurements all together. The ZWD measurements adjusted on mean-sea-level obtained from each method can be expressed as spherical harmonics function as below.

- GNSS-derived ZWD measurements:

$$ZWD_{GNSS}(\phi,\lambda) = H_{SH}(\phi,\lambda)\cdot\overline{x}_{coeff} + v_G \quad \textbf{(5.30)}$$

- Weather data-based ZWD measurements:

$$ZWD_{Weather}(\phi,\lambda) = H_{SH}(\phi,\lambda)\cdot\overline{x}_{coeff} + \beta_W + v_W \quad \textbf{(5.31)}$$

- SBAS empirical model-based ZWD measurements

$$ZWD_{Empirical}(\phi,\lambda) = H_{SH}(\phi,\lambda)\cdot\overline{x}_{coeff} + \beta_E + v_E \quad \textbf{(5.32)}$$

The symbol v represents the Gaussian random noise of each measurements. As shown in Figure 5.18, the estimated ZWD from the carrier-phase observations of the WRS is very accurate with RMS 0.5 cm; however, the number of available data is as small as the number of WRS, which is distributed very sparsely in wide-area. On the other hand, the accuracy of weather data-based ZWD is as low as about RMS 4 cm, while a huge number of data obtained from the AWS site very densely installed in anywhere nationwide is available as shown in Figure 5.19. The SBAS empirical model with an accuracy of RMS 12 cm is used to prevent model divergence in areas outside the AWS network. The ZWD value of SBAS model is calculated for pre-defined grid points at 5 degrees intervals as shown in Figure 5.20. That is, these ZWD measurements are complementary to each other.

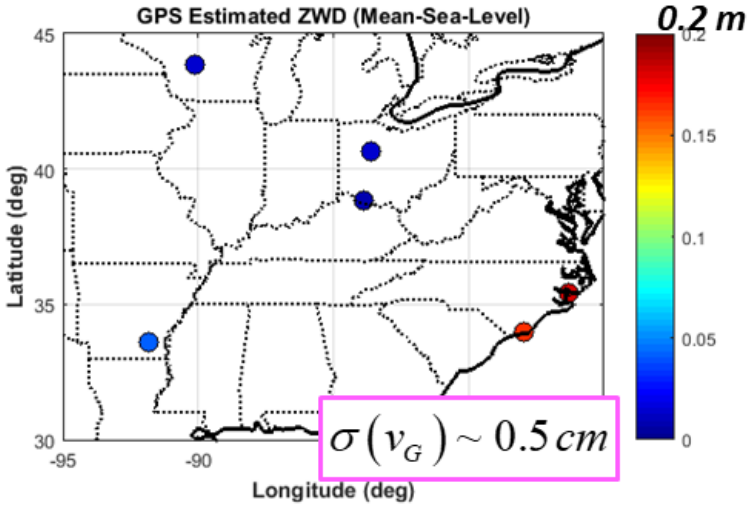

Figure 5.18 ZWD measurements of GPS-based estimation

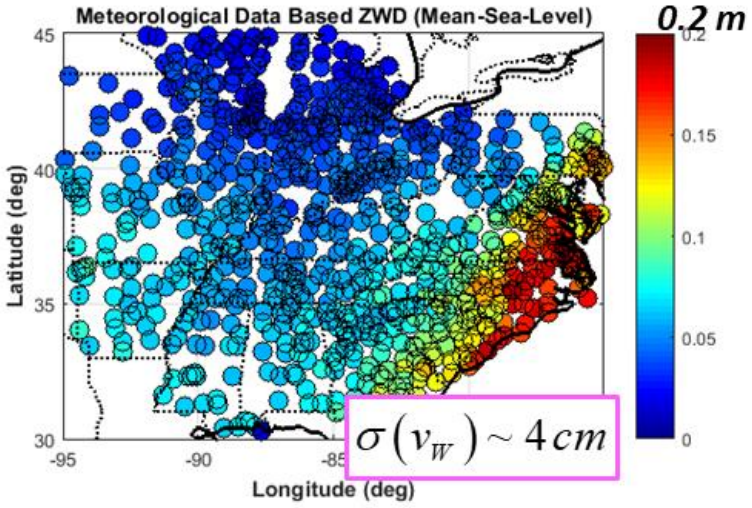

Figure 5.19 ZWD measurements based on weather data

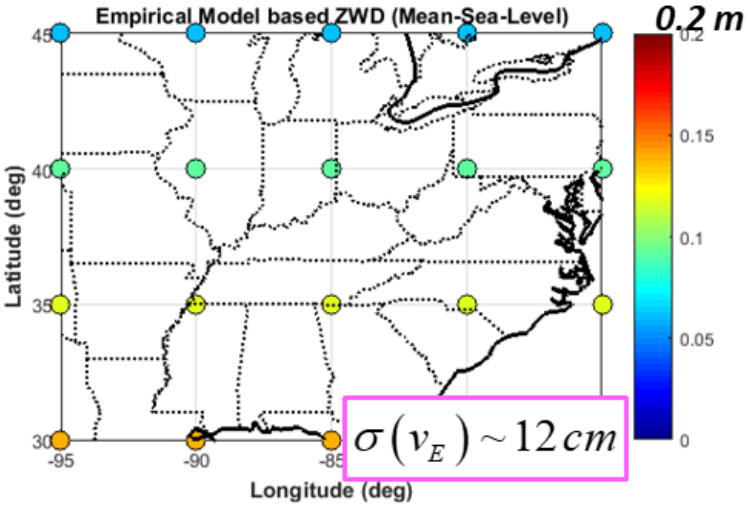

Figure 5.20 ZWD measurements of SBAS empirical model

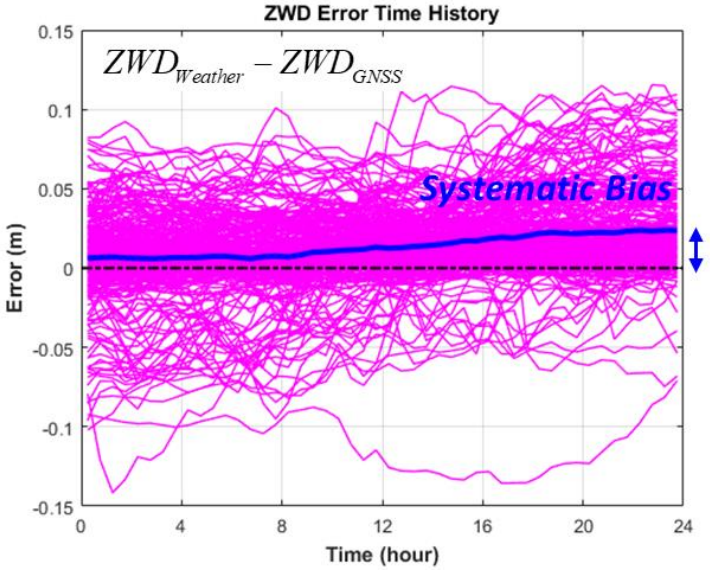

Figure 5.21 Systematic bias between GPS-based ZWD and weather data based ZWD

The weather data based model and SBAS empirical model have their own systematic bias β compare to GNSS-derived ZWD model [147]. We assume that there is no systematic bias between GNSS-based ZWD measurements and spherical harmonics model. In general, the systematic bias is larger when the troposphere delays are extremely unstable in rainfall events. Figure 5.21 shows the systematic bias over time and residual error of ZWD based on weather data for 24 hours on January 24th, 2019 in the USA CONUS. This systematic biases are also included in the estimation state to match the spatial characteristics of the precise GPS-based ZWD values with the weather data-based ZWD values and SBAS empirical model-based ZWD values. Finally, filter observation model can be expressed as follows. All of the ZWD measurements are independent.

$$\overline{x} = \begin{bmatrix} \overline{x}_{coeff}^{T} & \beta_{Weather} & \beta_{Empirical} \end{bmatrix}^{T} \tag{5.33}$$

$$\overline{z} = \begin{bmatrix} \overline{z}_{GNSS} \\ \overline{z}_{Weather} \\ \overline{z}_{Empirical} \end{bmatrix} = \begin{bmatrix} (H_{SH})_{A\times M} & 0_{A\times 1} & 0_{A\times 1} \\ (H_{SH})_{B\times M} & 1_{B\times 1} & 0_{B\times 1} \\ (H_{SH})_{C\times M} & 0_{C\times 1} & 1_{C\times 1} \end{bmatrix} \overline{x} + \begin{bmatrix} \overline{v}_{G} \\ \overline{v}_{W} \\ \overline{v}_{E} \end{bmatrix} \tag{5.34}$$

$$H = \begin{bmatrix} (H_{SH})_{A\times M} & 0_{A\times 1} & 0_{A\times 1} \\ (H_{SH})_{B\times M} & 1_{B\times 1} & 0_{B\times 1} \\ (H_{SH})_{C\times M} & 0_{C\times 1} & 1_{C\times 1} \end{bmatrix} \tag{5.35}$$

$$\overline{v} = \begin{bmatrix} \overline{v}_{G} \\ \overline{v}_{W} \\ \overline{v}_{E} \end{bmatrix} \tag{5.36}$$

$$W = \begin{bmatrix} W_G & 0 & 0 \\ 0 & W_W & 0 \\ 0 & 0 & W_E \end{bmatrix} \quad \textbf{(5.37)}$$

where the notation A is the number of WRS, B is the number of AWS, and C is the number of grid points. $M = (N+1)^2$ is the number of spherical harmonics coefficients considered as tropospheric corrections.

3) Estimation Method

A typical method for estimating above linear equation is the weighted least square. However, this technique does not impose limits on the size of the estimated values, which can lead to very large estimated state values. Because the compact WARTK needs to broadcast the estimated coefficients as message, the message capacity also increase as the large estimated value. To overcome this problem, a minimum variance estimation based on a priori information covariance Λ was proposed when estimating SBAS satellite correction [61], [148]. The performance index, estimated state and variance expressions for the minimum variance estimation technique are as follows.

$$\hat{x} = \left(\Lambda^{-1} + H^T W^{-1} H\right)^{-1} H^T W^{-1} \overline{z} \quad \textbf{(5.38)}$$

$$\hat{P} = \left(\Lambda^{-1} + H^T W^{-1} H\right)^{-1} \quad \textbf{(5.39)}$$

Minimum variance estimation techniques limit the size of intentionally estimated values, which can lead to an increase in error over the weighted last square. In this study, considering the capacity and precision of the message, a priori covariance set to 10-12. We estimates spherical harmonics coefficients and

systematic bias using minimum variance estimator. All of these states are varying slowly on time. The estimated spherical harmonics coefficients are broadcast as corrections to compact WARTK users. This study adopted 3rd order modeling with only 16 coefficients. Figure 5.22 shows the estimation results of 3rd order spherical harmonic coefficients on January 24th, 2019.

$$\hat{x}_{ZWD} = \{C_{00}, C_{10}, C_{20}, C_{30}, C_{11}, C_{21}, C_{31}, C_{22}, C_{32}, C_{33}, \cdots \\ S_{11}, S_{21}, S_{31}, S_{22}, S_{32}, S_{33}\} \quad \textbf{(5.40)}$$

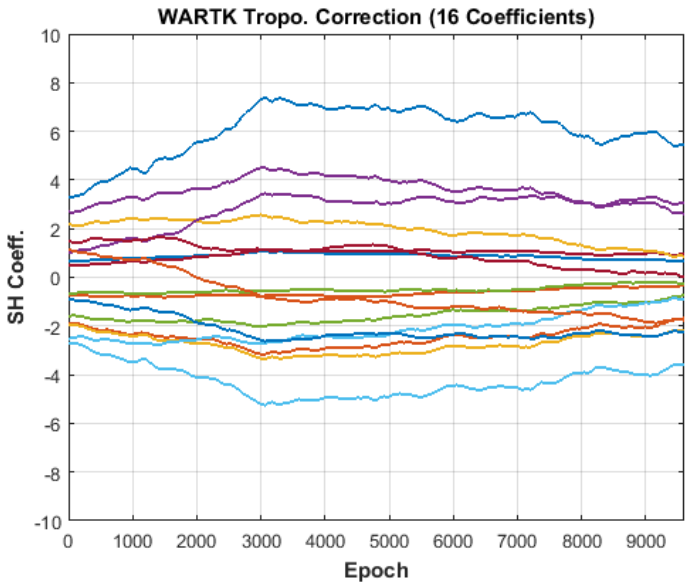

Figure 5.22 Estimation results of 3rd order spherical harmonic coefficients

5.2.4 Correction Applying Method for User

The compact WARTK users who receive the tropospheric correction can calculate their own zenith tropospheric delay at user location and height. Figure 5.23 represents the user process for applying the tropospheric corrections of compact WARTK. First of all, the mean-sea-level ZWD value at user location (ϕ_u, λ_u), anywhere in service area, can be reconstructed using the spherical harmonics coefficients of tropospheric corrections as shown in Figure 5.24.

$$ZWD_{user}(0) = H_{SH}(\phi_u, \lambda_u) \cdot \hat{x}_{ZWD} \quad \textbf{(5.41)}$$

After that, the ZWD value on mean-sea-level is adjust into user height H_u using equation (5.4), which is the height adjustment process by SBAS empirical model. The ZHD at user height is computed by SBAS model of equation (5.3). Finally, the corrections for slant tropospheric delay on user observations can be calculated as following equation. $m_{hyd}(El)$ and $m_{wet}(El)$ are the Niell mapping function of hydrostatic and wet components, respectively. The sign of corrections are set to eliminate the tropospheric delay error by adding correction to user measurements.

$$TC = -\left\{ ZHD_{user}(H_u) \cdot m_{hyd}(El) + ZWD_{user}(H_u) \cdot m_{wet}(El) \right\} \quad \textbf{(5.42)}$$

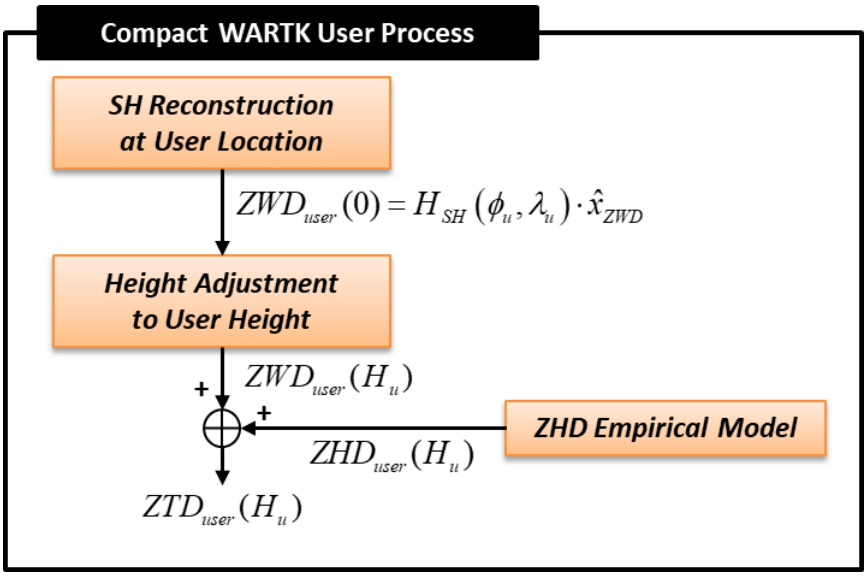

Figure 5.23 User process for applying the tropospheric corrections

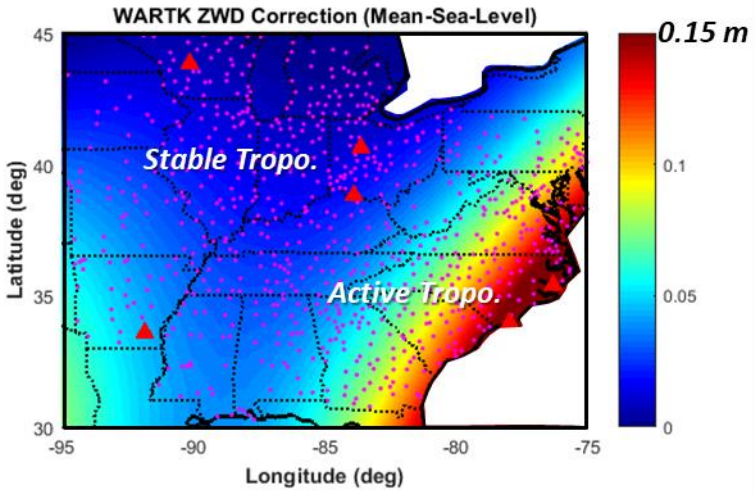

Figure 5.24 ZWD value on mean-sea-level by spherical harmonics corrections of compact WARTK

5.3 Correction Performance Analysis Results

5.3.1 Feasibility Test Environments

A feasibility test for verifying the accuracy of tropospheric corrections was conducted. The system configuration and environment are the same as in subsection 4.3.1. The six reference stations (GRTN, KNTN, NCSO, NCFF, ARMO, WINL), which is located on Midwest and south USA, are selected for WRS of compact WARTK system. The precise zenith tropospheric delay are estimated by using GPS carrier-phase measurements obtained from these 6 WRS with 1 second interval. The meteorological data are collected in METAR format every 5 minutes from the AWS sites that managed by the NWS, FAA, and DoD. Total 781 AWS sites are located in target service area of compact WARTK. Total 71 user sites managed by the NOAA are chosen for feasibility test. Six of them are WRS sites, and the remaining 65 sites are additionally selected reference stations. The true (or reference) value of the zenith tropospheric delay for accuracy analysis is obtained from the online CSRS-PPP service estimated by post-processing [149]. The locations of WRS (red triangle), AWS (magenta star), and user sites (blue triangle) are shown in Figure 5.25. The date for performance analysis is January 24th, 2019, when the southern USA was heavily rainy. It is more difficult to estimate zenith wet delays in rainy areas where the troposphere is unstable. Figure 5.26 shows the weather condition on test date. The figure on left shows the 24 hour precipitation, the figure on right represents the surface weather map. These daily weather maps are provided by weather prediction center of NOAA. Table 5.3 summarizes the feasibility test environments.

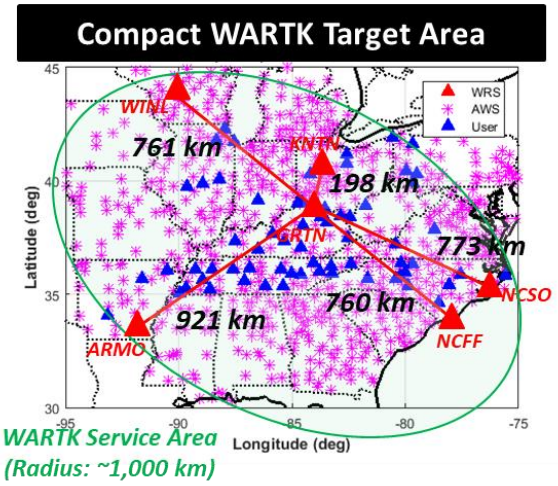

Figure 5.25 Locations of WRS, AWS, and user for preliminary test

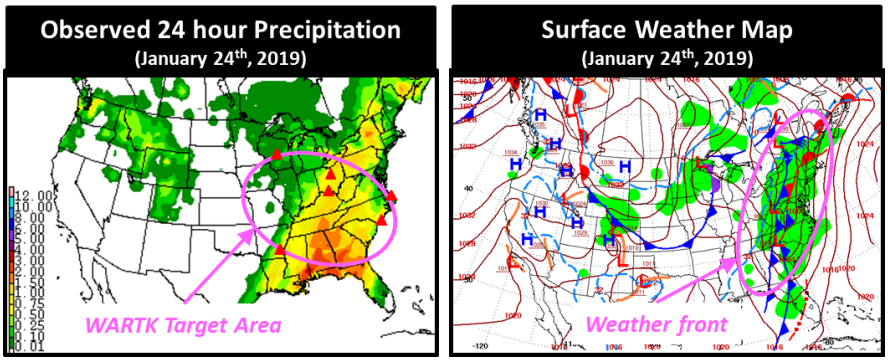

Figure 5.26 Weather condition on feasibility test date (2019.01.24.)

Table 5.3 Summary of feasibility test environments

Date of Test	January 24th, 2019 (Heavy rainy day)
Time	UTC 16:15:00 ~ 18:55:00 (9600 epochs)
Interval	1 sec
WRS Sites	6 WRSs (GRTN, KNTN, NCSO, NCFF, ARMO, WINL)
AWS Sites	781 Sites (data interval: 5 min)
User Sites	71 Sites (6 WRSs + 65 Users)
Constellation	GPS Only (L1/L2/L5 signals)
Reference ZTD	Online CSRS-PPP (Post-Processing)

5.3.2 Zenith Correction Domain Analysis

This subsection analyzes accuracy performance of tropospheric corrections. This study compares the performance of SBAS empirical model, grid-based PPP-RTK corrections, and coefficient-based compact WARTK corrections. The grid-based PPP-RTK tropospheric corrections are generated by Kriging estimation using only carrier-phase measurements collected from 6 WRS. A total of 336 predefined grid points with 1 degree intervals in latitude and longitude is required to cover the target service area. The coefficient-based compact WARTK tropospheric corrections are generated by proposed method based on 3rd order spherical harmonics model using precise carrier-phase measurements and weather data together. That is, 16 coefficients are estimated as tropospheric corrections.

First of all, the residual error of zenith tropospheric delay is calculated after applying the tropospheric corrections at the user locations. Figure 5.27 shows the snapshot analysis results of zenith tropospheric corrections at UTC time of 16:45:00. The top figure represents the true value of ZTD at user locations obtained from the online CSRS-PPP service. The two middle figures show the value of ZTD corrections interpolated at user locations. The left one is the grid-based PPP-RTK corrections, and the right one is the proposed compact WARTK corrections. The two bottom color map are the residual error of ZTD after compensation. Red means a higher residual error, blue means a smaller residual error.

As shown in the results, the compact WARTK corrections are more effective than grid-based PPP-RTK corrections, especially in areas where WRSs are not installed since weather data provides the additional tropospheric information.

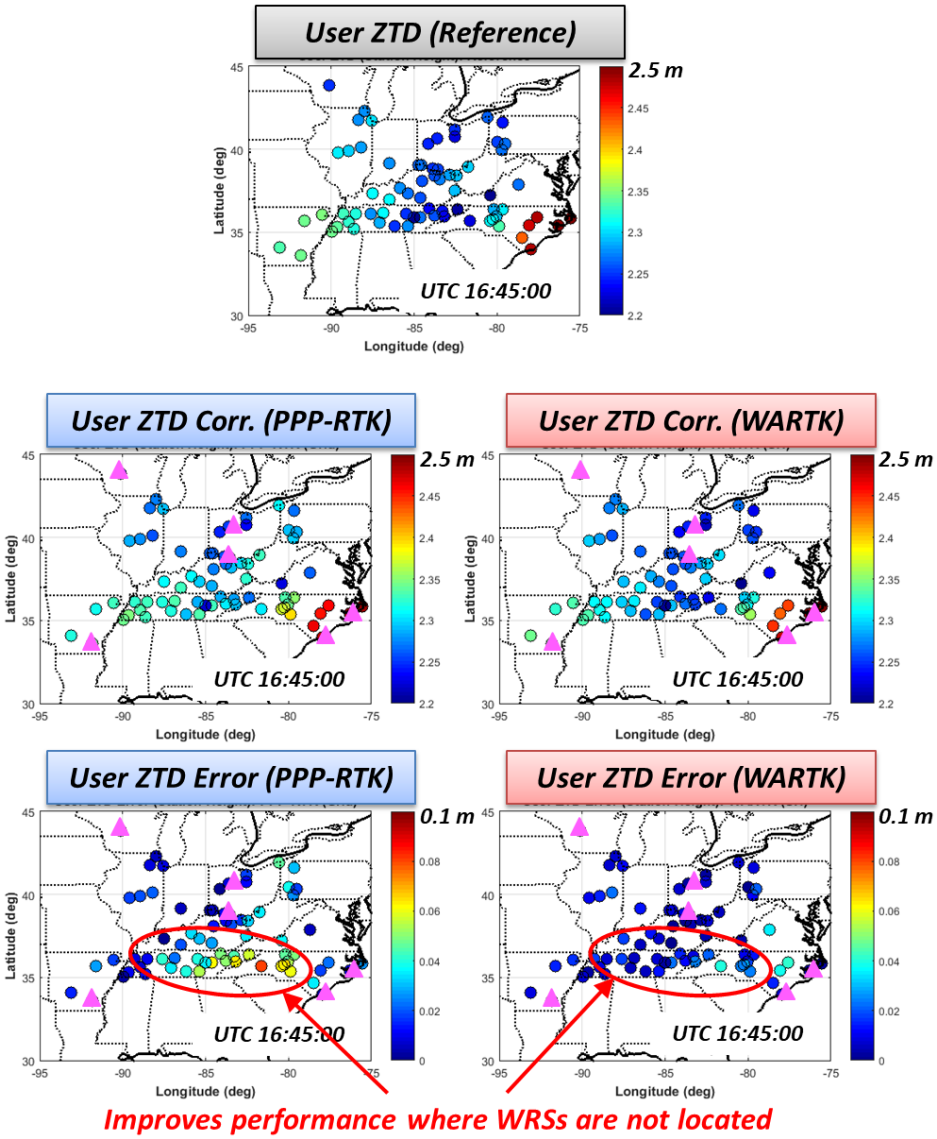

Figure 5.27 Results of ZTD residual error at user locations (UTC 16:45:00)

Error analysis was conducted for the entire analysis time and RMS error statistics were calculated for each user location for each ZTD corrections. Figure 5.28 represents the RMS error map of ZTD residual after compensate by SBAS empirical model. Figure 5.29 shows RMS error map by PPP-RTK corrections, and Figure 5.30 shows RMS error map by proposed compact WARTK corrections. Red means a higher RMS error, blue means a smaller RMS error. When comparing colors that indicate RMS errors, the proposed compact WARTK correction can be accurately compensated the ZTD at user locations to blue throughout the target service area. The PPP-RTK corrections are also more accurate than the SBAS model, but the performance of areas away from WRS is degraded.

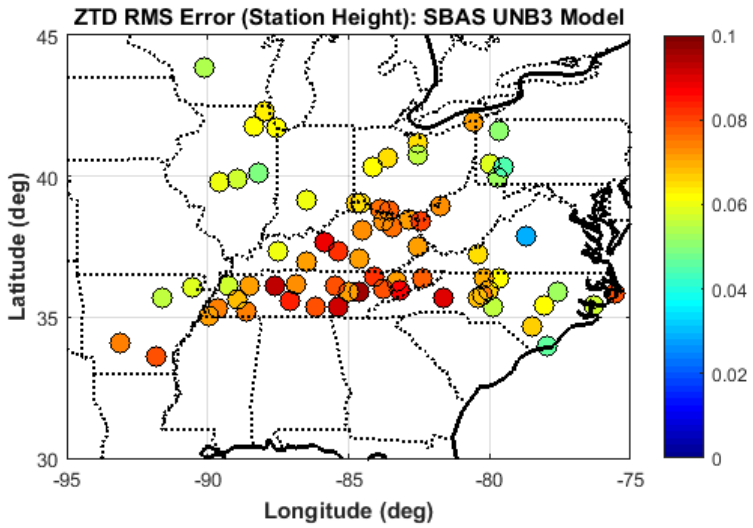

Figure 5.28 RMS error map of ZTD residual by SBAS empirical model

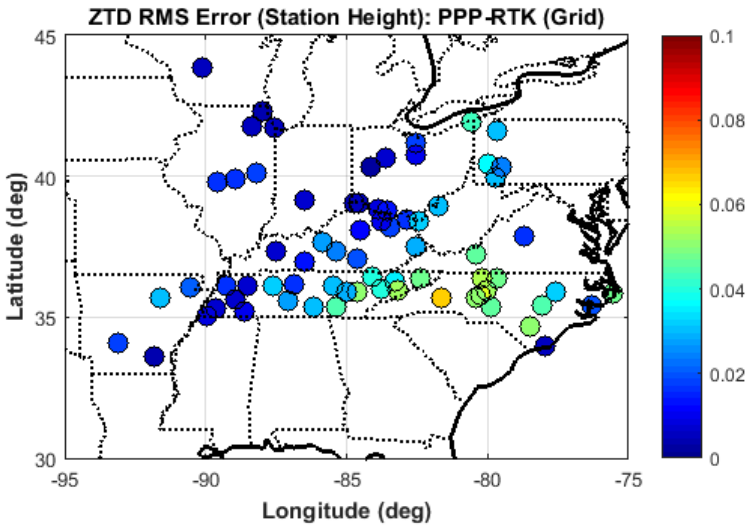

Figure 5.29 RMS error map of ZTD residual by PPP-RTK corrections

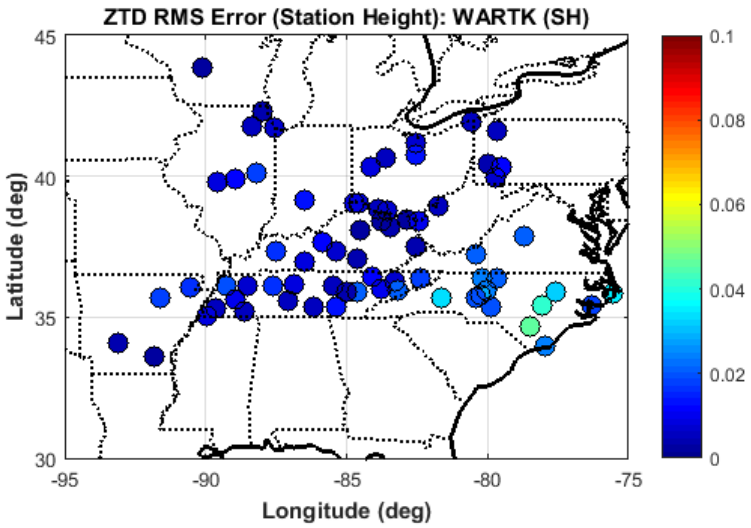

Figure 5.30 RMS error map of ZTD residual by compact WARTK corrections

Figure 5.31 is a graph to verify linearity between the true ZTD values (x-axis) and ZTD corrections (y-axis) for accuracy analysis. If the correlation coefficient R is closer to one, it means the more accurate solution. Figure 5.32 and Figure 5.33 represent the time history and histogram of ZTD residual error for all user locations, respectively. The green color means the SBAS model, the blue represents the PPP-RTK corrections, and the red shows the accuracy of compact WARTK corrections. Consequently, the red line which means the proposed compact WARTK tropospheric corrections shows the best accuracy performance. The linear correlation coefficient R is 0.97, and the histogram shows the highest peak and narrow width.

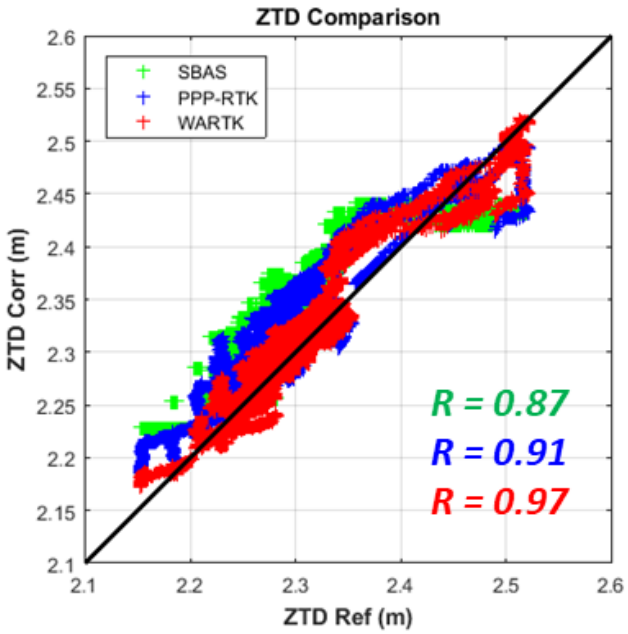

Figure 5.31 Comparison of ZTD at user locations

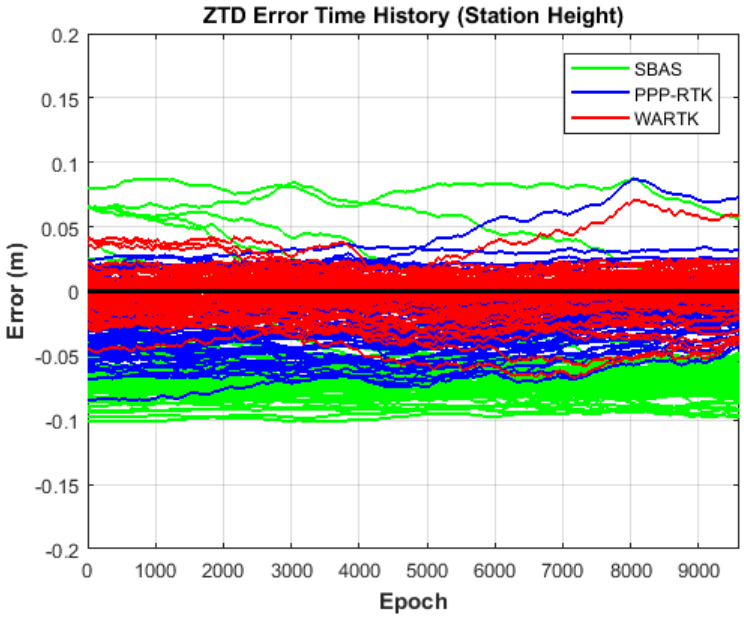

Figure 5.32 Time history of ZTD residual error at user locations

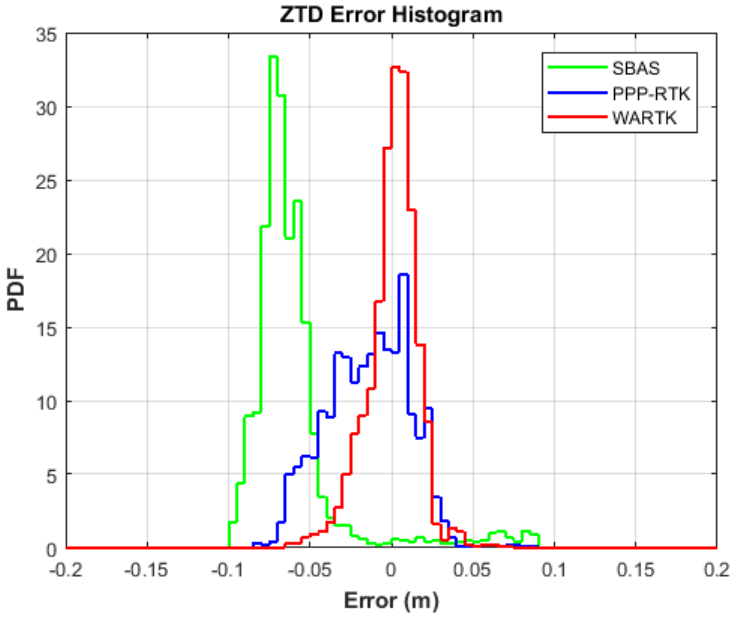

Figure 5.33 Histogram of ZTD residual error at user locations

Table 5.4 summarizes the accuracy statistics of zenith tropospheric corrections. The total number of data samples are 681671 for 71 user locations. As shown in Figure 5.32 and Figure 5.33, the compact WARTK corrections especially reduce the bias error almost 90% with compare to grid-based PPP-RTK corrections. The RMS error statistics of proposed corrections is under 2 cm, and the performance is improved about 47% than grid model. The maximum value is 5 cm, but it is within the allowable values for which the WARTK user can solve their integer ambiguity correctly. In conclusion, the tropospheric corrections of compact WARTK is more accurate than SBAS and PPP-RTK solutions. By utilizing the advantages of weather data, the compact WARTK can maximize the accuracy performance of tropospheric corrections with only a few number of WRSs. In other words, the proposed method requires a much smaller number of reference stations than the PPP-RTK to generate tropospheric corrections.

Table 5.4 Accuracy statistics of zenith tropospheric corrections

ZTD Error Statistics	Bias (cm)	STD (cm)	RMS (cm)	95% (cm)	99% (cm)
SBAS (Model)	6.2	3.1	6.9	9.1	9.7
PPP-RTK (Grid)	1.7	2.5	3.0	6.1	7.0
WARTK (Coeff.)	0.2	1.6	1.6	3.4	5.3
	88% ↓	36% ↓	47% ↓	44% ↓	24% ↓

5.3.3 Message Data Bandwidth Analysis

Message data bandwidth needed to broadcast the tropospheric corrections to the users was analyzed. According to message design of grid-based PPP-RTK tropospheric corrections by QZSS CLAS, the corrections considering only ZWD requires 8 bits of data field for each predefined grid points [30]. Therefore, the PPP-RTK requires 2688 bits for 336 grid points for covering target service area without scheduling. On the other hand, it is possible to design the messages for tropospheric corrections of compact WARTK as shown in the Table 3.13 considering the characteristics of spherical harmonics coefficients. Consequently, as summarized in Table 5.5, the message bandwidth can be dramatically reduced by 90% because the compact WARTK to cover same service region only requires 256 bits for only 16 coefficients with each 16 bits data field. These tropospheric correction message can be sufficiently broadcast with about 25.6 bps under 10 second scheduling according to message design of Table 3.13. In conclusion, it is possible to geosynchronous broadcasting with very low-speed data link.

Table 5.5 Message bandwidth for tropospheric corrections

Message Bandwidth *(without Scheduling)*	
PPP-RTK (Grid)	336 X (int 8)* = 2688 bit
WARTK (Coeff.)	16 x (int 16) = 256 bit

90% ↓

CHAPTER 6. COMPACT WIDE-AREA RTK USER TEST RESULTS

6.1 Compact Wide-Area RTK User Process

The users who can receive dual- or triple-frequency signals get benefit from the compact WARTK system. Figure 6.1 represents the block diagram for compact WARTK user process. First of all, the user collects its measurements for all satellites in field of view. After the pre-processing, the user immediately calculate its stand-alone position roughly by a weighted least-square estimation using pseudorange measurements.

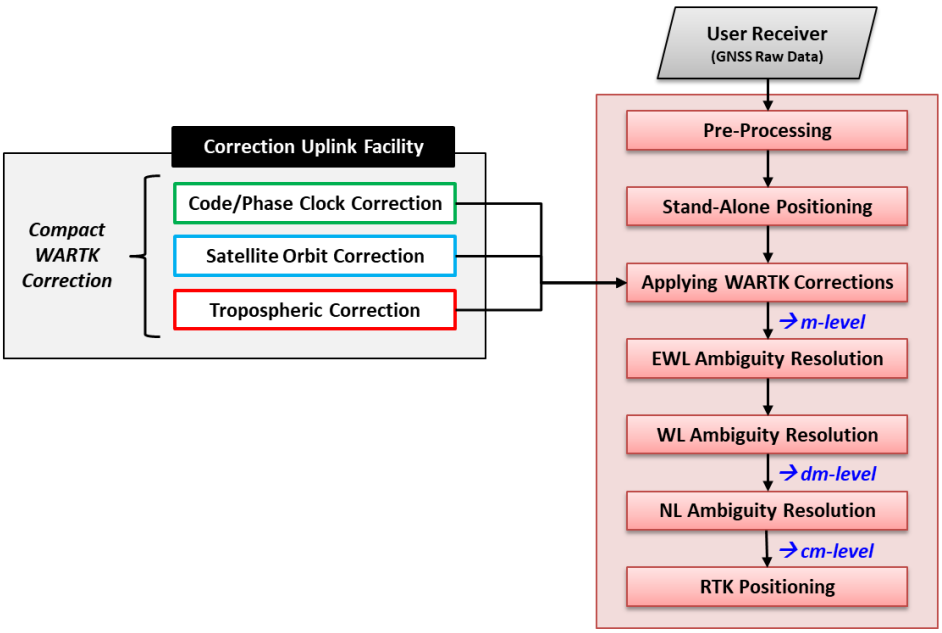

Figure 6.1 Block diagram for compact wide-area RTK user process

The vector-type compact WARTK corrections received from GEO satellite or other communication links is properly interpolated based on the meter-level approximate user position. The satellite orbit residual error of line-of-sight direction can be reduced using the satellite orbit corrections in equation (3.57). The radial, along-track, and cross-track components of orbit corrections are converted into ECEF coordinates [12].

$$\delta \bar{R} = T_{ECEF2RAC}^{-1} \cdot \delta \bar{O} \tag{6.1}$$

$$OC = -\delta \bar{R}^{j} \cdot \hat{e}_{u}^{j} \tag{6.2}$$

The satellite clock residual error can be eliminated by the satellite CPC corrections for each linear-combination in equation (3.58) to (3.63). The slant tropospheric delay error can be removed by using the tropospheric corrections in equation (5.42). Finally, the range corrections for six linear combinations in Table 3.3 are computed as following equations. The sign of corrections are set to eliminate the GNSS range error by adding correction to user measurements.

$$RC_{EWL} = CPC_{EWL} \tag{6.3}$$

$$RC_{WL1} = CPC_{WL1} \tag{6.4}$$

$$RC_{WL2} = OC + CPC_{WL2} + TC \tag{6.5}$$

$$RC_{NL1} = OC + CPC_{NL1} + TC \tag{6.6}$$

$$RC_{NL2} = OC + CPC_{NL2} + TC \tag{6.7}$$

$$RC_{PRIF} = OC + CPC_{PRIF} + TC \tag{6.8}$$

The process of applying these range corrections to user linear-combination measurements is the same as the effect of single-difference between the stations of the RTK technique. Finally, the user can obtain the double-differenced measurements with all GNSS errors eliminated through the single-difference between satellites.

Therefore, the double-differenced integer ambiguity included in user measurements can correctly and quickly resolves through the proposed TCAR method described in section 3.2. The navigation Kalman filter has the estimation states of position, velocity, and acceleration as a random walk process with the states of integer ambiguity. The system equation of geometry-based ambiguity resolution of user can be designed as following equations. n is the number of states for integer ambiguity that is the same number of visible satellites except the reference satellite.

$$\dot{\overline{x}} = F\overline{x} + \Gamma\overline{w}$$

$$\overline{x} = \begin{bmatrix} \overline{x}_N & \overline{x}_{pos} \end{bmatrix}^T \qquad \overline{w} = \begin{bmatrix} \overline{w}_N & \overline{w}_{acc} \end{bmatrix}^T$$

$$F = \begin{bmatrix} O_{n\times n} & O_{n\times 9} \\ O_{9\times n} & F_{pos} \end{bmatrix} \qquad \Gamma = \begin{bmatrix} I_{n\times n} & O_{n\times 3} \\ O_{9\times n} & \Gamma_{pos} \end{bmatrix} \qquad \textbf{(6.9)}$$

$$F_{pos} = \begin{bmatrix} O_{3\times 3} & I_{3\times 3} & O_{3\times 3} \\ O_{3\times 3} & O_{3\times 3} & I_{3\times 3} \\ O_{3\times 3} & O_{3\times 3} & O_{3\times 3} \end{bmatrix} \qquad \Gamma_{pos} = \begin{bmatrix} O_{3\times 3} \\ O_{3\times 3} \\ I_{3\times 3} \end{bmatrix}$$

The observation equation can be designed as follows.

$$\bar{z} = H\bar{x} + \bar{v}$$

$$\bar{x} = \begin{bmatrix} \bar{x}_N & \bar{x}_{pos} \end{bmatrix}^T \qquad \bar{v} \sim W\left(0, R_{n\times n}\right)$$

$$H = \begin{bmatrix} \lambda \cdot I_n & H_{pos} \end{bmatrix} \tag{6.10}$$

$$H_{pos} = \begin{bmatrix} {}^1\nabla^{ref}\hat{e} & O_{1\times 3} & O_{1\times 3} \\ \vdots & \vdots & \vdots \\ {}^n\nabla^{ref}\hat{e} & O_{1\times 3} & O_{1\times 3} \end{bmatrix}$$

The float ambiguity estimated from the navigation Kalman filter is mapped into integer domain by LAMBDA method. In addition, two ambiguity validation test are adopted to verify the integer ambiguity: F-ratio test based on observation residuals and fixed-rate ratio test based on ambiguity residuals. Finally, the high-accuracy position are calculated after correctly determined the integer ambiguity in each step. The decimeter-level position can obtain almost immediately after fixing WL ambiguity. The centimeter-level final solution can calculate after fixing NL ambiguity within a few minutes.

The triple-frequency users used all six linear-combinations for ambiguity resolution can compute their centimeter-level position very quickly. The dual-frequency users, or in case that some satellites provide only dual-frequency signals can also determine their centimeter-level position; however, convergence time is slightly longer than full-constellation triple-frequency GPS users. The satellite with only dual-frequency signals applied three linear-combinations, WL1, NL1, and PRIF for determining their integer ambiguity.

6.2 User Performance Test Results

6.2.1 Feasibility Test Environments

User performance analysis using GPS actual observations with 1 second intervals on January 24th, 2019 was conducted. The test environment is the same as the that of previous correction performance analysis. The compact WARTK system for feasibility test consists of six WRSs to cover the 1,000 km radius area. The detailed location and equipment of each WRS were summarized in Table 3.1 and Table 3.2. The six reference stations located in target service area are chosen as the compact WARTK users. Their locations and tropospheric delay conditions are shown in Figure 6.2. The red triangle represents the WRS, and the blue square means the user site. The color contour map means the zenith wet delay on mean-sea-level estimated by the spherical harmonics coefficients of tropospheric corrections. As shown in the figure, three of users (SIDN, ARGS, OHAS) are located in stable tropospheric condition, and the other three of users (NCMG, NCRE, NCTR) are located in active tropospheric condition that means heavy rainy area. The detailed location and equipment of each user were summarized in Table 6.1 and Table 6.2. All users observe 9 visible GPS satellites for which the compact WARTK corrections are applied. Figure 6.3 shows the satellite elevation angle of SIDN user sites, and its skyplot was represented on Figure 4.8. The position DOP value in test period is about 1.76. The satellites of PRN 1, 3, 10, 26, 25, 32 can collect triple-frequency signals, and the satellites of PRN 14, 22, 31 only observe dual-frequency signals. The PRN 32, the highest elevation angle with triple-frequency signals, is chosen as reference satellite.

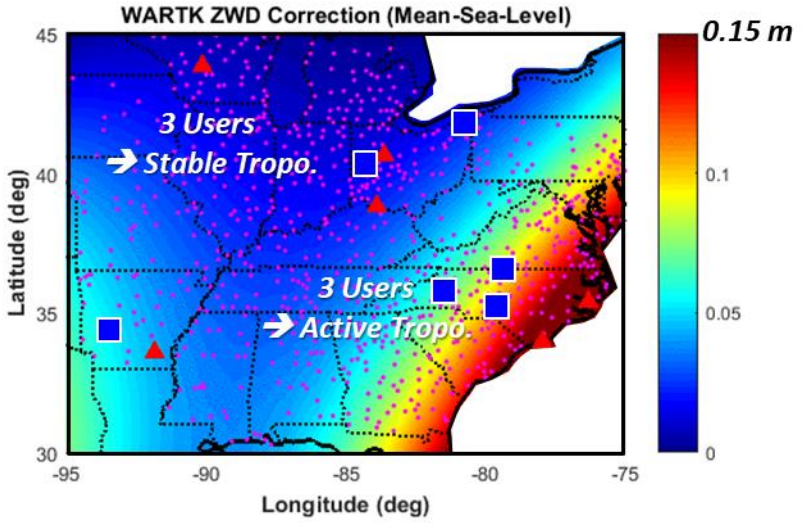

Figure 6.2 User locations for feasibility test and tropospheric delay conditions (zenith wet delay on mean-sea-level)

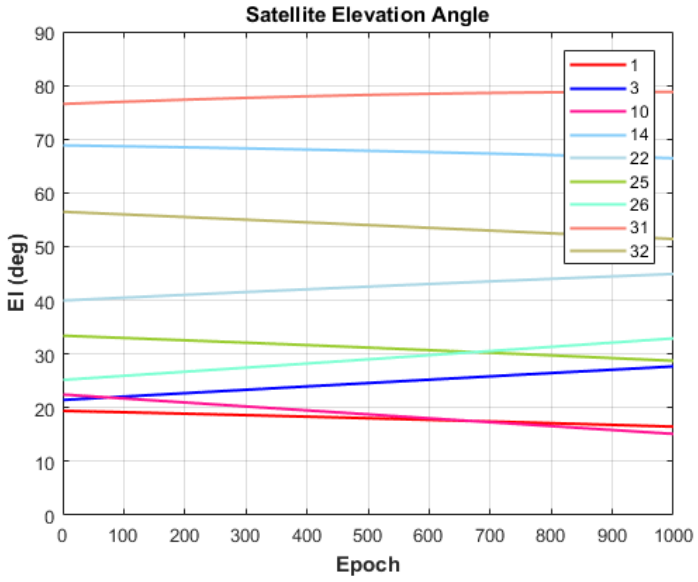

Figure 6.3 Satellite elevation angle on test period (9 visible GPS satellites)

Table 6.1 Location of antenna reference point of selected user in USA

No.	*Name*	*State*	*Latitude (deg)*	*Longitude (deg)*	*Height (m)*
1	SIDN	OH	40.31 N	84.17 W	292.0 m
2	ARGS	AR	34.07 N	93.12 W	69.4 m
3	OHAS	OH	41.93 N	80.55 W	180.5 m
4	NCMG	NC	35.71 N	81.66 W	343.5 m
5	NCRE	NC	36.36 N	79.67 W	233.5 m
6	NCTR	NC	35.37 N	79.87 W	142.7 m

**Coordinates: IGS08 (Epoch 2005.0)*

Table 6.2 Receiver and antenna type of selected user in USA

No.	*Name*	*State*	*Receiver Type*	*Antenna Type*
1	SIDN	OH	TRIMBLE NETR9 v5.22	TRM59900.00 SCIS
2	ARGS	AR	TRIMBLE NETR9 v5.33	TRM115000.00 NONE
3	OHAS	OH	TRIMBLE NETR9 v5.22	TRM115000.00 NONE
4	NCMG	NC	TRIMBLE NETR9 v5.37	TRM57971.00 NONE
5	NCRE	NC	TRIMBLE NETR9 v5.30	TRM57971.00 NONE
6	NCTR	NC	TRIMBLE NETR9 v5.37	TRM57971.00 NONE

**Reference date: 2019.01.24*

Table 6.3 Summary of feasibility test environments

Date of Test	January 24th, 2019 (Heavy rainy day)
Time	UTC 17:46:40 ~ 18:03:19 (1000 epochs)
Interval	1 sec
WRS Sites	6 WRSs (GRTN, KNTN, NCSO, NCFF, ARMO, WINL)
User Sites	6 Users (SIDN, ARGS, OHAS, NCMG, NCRE, NCTR)
Receiver Type	Trimble NetR9
Constellation	GPS Only (L1/L2/L5 signals) – 9 visible satellites

6.2.2 User Range Domain Analysis

First of all, the user range domain analysis was conducted. After applying the corrections, the residual error of double-differenced user range is calculated by eliminating true user distance and true integer ambiguity fixed by RTK post processing. Figure 6.4, Figure 6.5, and Figure 6.6 represent the residual error of the six linear-combinations for new TCAR algorithm. Each figure shows the results for SIDN site with a baseline distance of 163 km from GRTN master station, for NCTR site with 526 km baseline, and for ARGS site with 982 km baseline. The top subplot represents the combinations of EWL, WL1, and WL2 in order. The bottom subplot represent the combination of NL1, NL2, and PR-IF in order. The black bold line means the half of wavelength of each combination. The other color lines indicate residual error, and each color corresponds to the satellite illustrated in Figure 6.3.

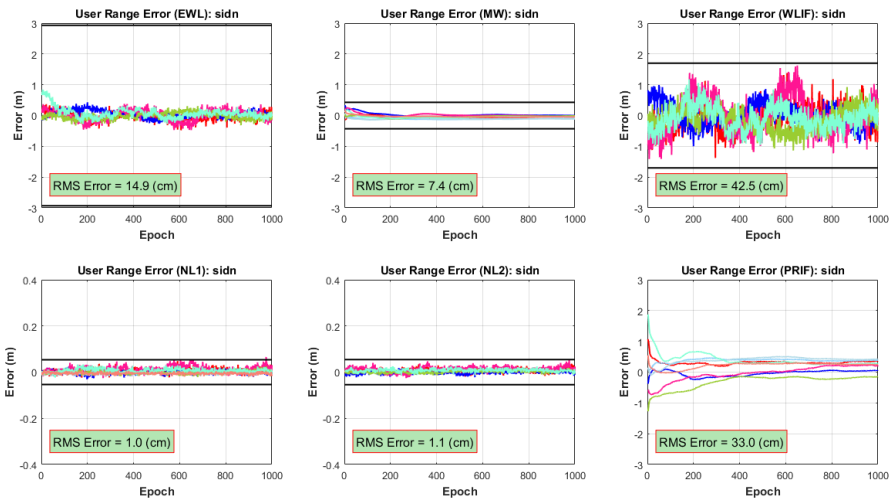

Figure 6.4 User range domain errors of six linear-combinations (SIDN, baseline: 163 km)

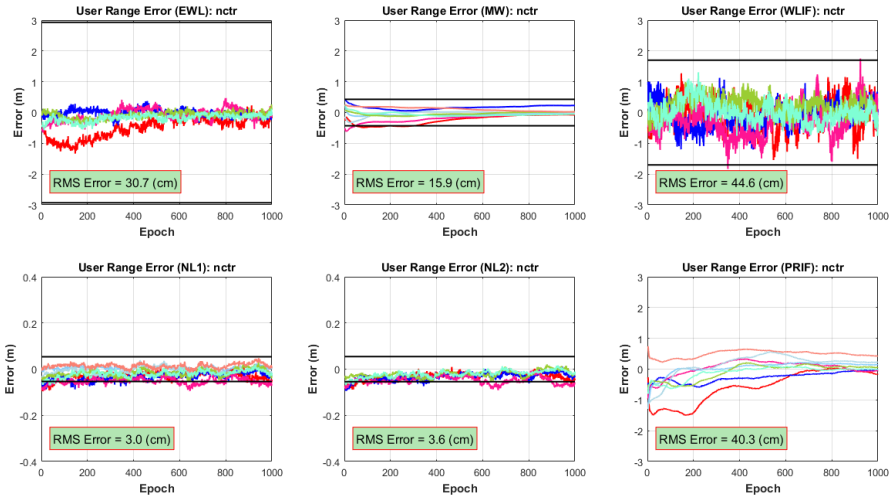

Figure 6.5 User range domain errors of six linear-combinations (NCTR, baseline: 526 km)

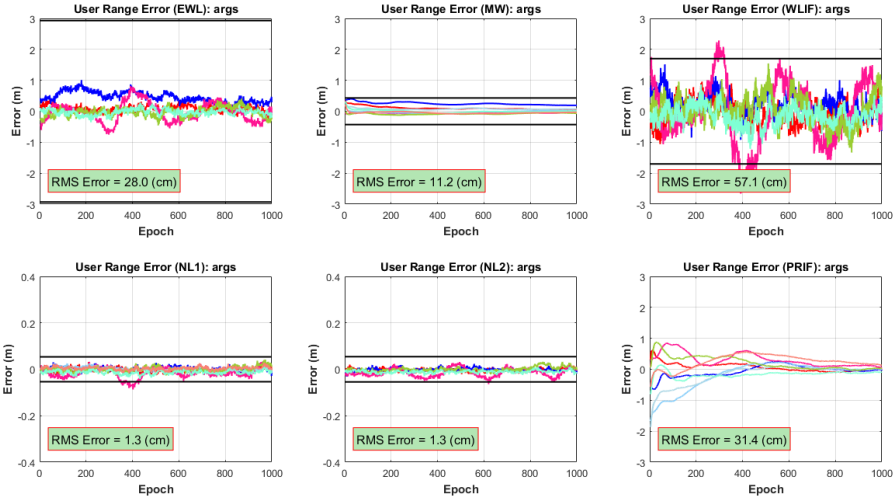

Figure 6.6 User range domain errors of six linear-combinations (ARGS, baseline: 982 km)

As shown in these results, only residual errors of less than half wavelength remain for six linear combinations of all user sites after the compact WARTK corrections are applied. That is, the compact WARTK user located in continental scale service area can sufficiently eliminate GPS error elements to allow ambiguity resolution.

The user range residual error of the existing network RTK and the proposed compact WARTK system was compared. Both systems generate their corrections using the same six reference stations in target service area of 1,000 km radius. Only the residual error of L1/L2 ionospheric-free combination corresponding to the NL1 combination was analyzed. Figure 6.7 shows the results of network RTK for three users (SIDN, NCRT, ARGS), and Figure 6.8 represents the results of compact WARTK of same user locations. Figure 6.9 summarizes the results of user range errors relative to the baseline distance from the GRTN master station. The range error of five auxiliary WRS was also illustrated with six users. Because the baseline distance between stations is very long, the network RTK which produces scalar-type corrections shows very large range residual errors. The range error increases as users move further away from the master station. That means, the network RTK cannot fix integer ambiguity correctly in wide-area. On the other hand, the compact WARTK which generates vector-type corrections shows very good performance regardless of baseline distance. The residual error is a centimeter-level that the integer ambiguity can be correctly determined for all target locations in wide-area. Consequently, the compact WARTK can dramatically expand the service coverage by using vector-type corrections for each error components unlike the scalar-type corrections of network RTK.

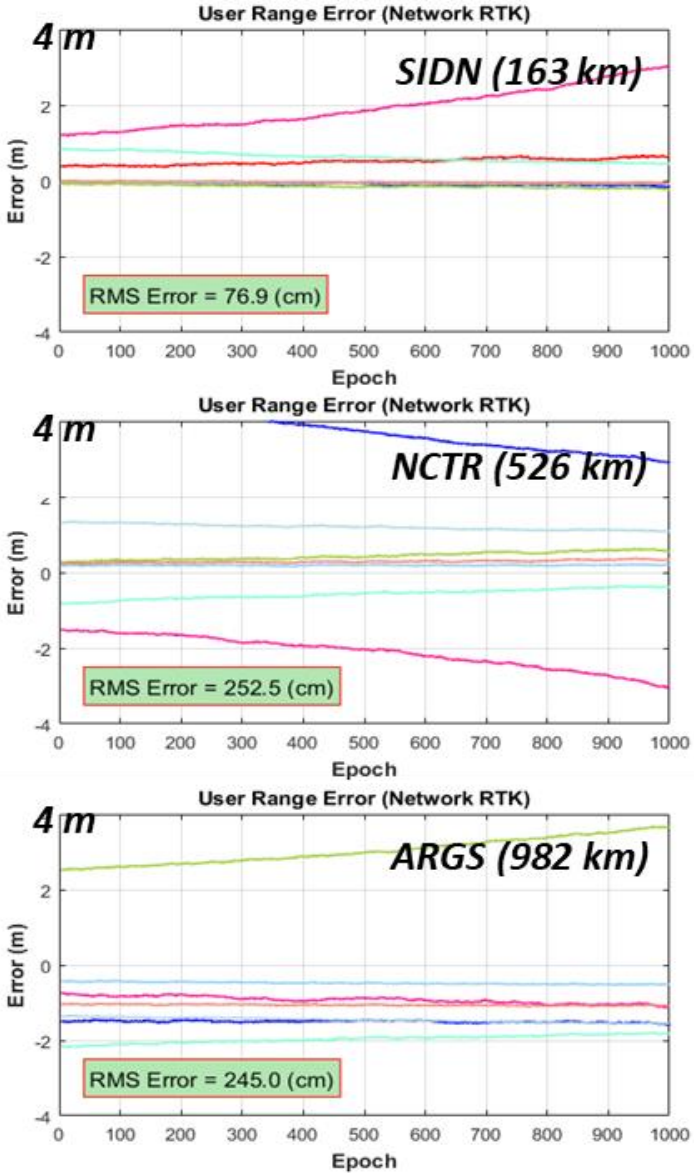

Figure 6.7 User range domain errors of L1/L2 iono-free combination (Network RTK, scalar-type corrections)

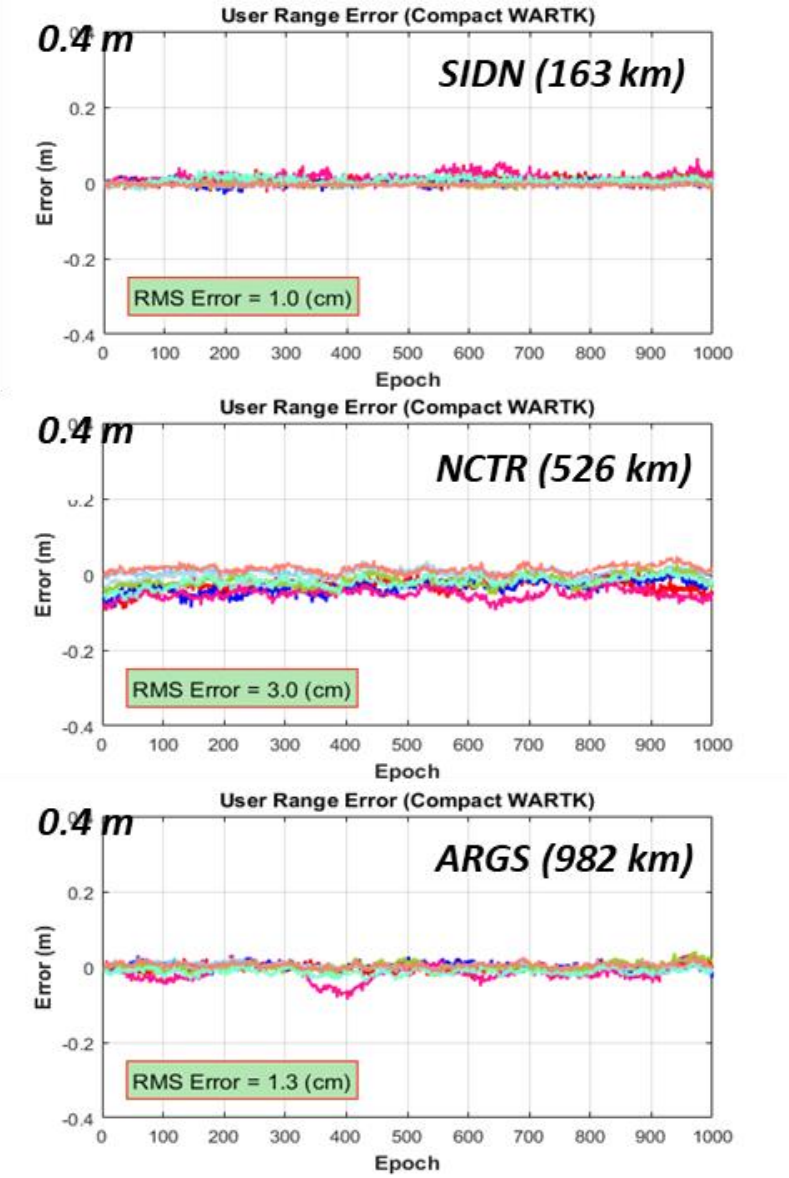

Figure 6.8 User range domain errors of L1/L2 iono-free combination (Compact WARTK, vector-type corrections)

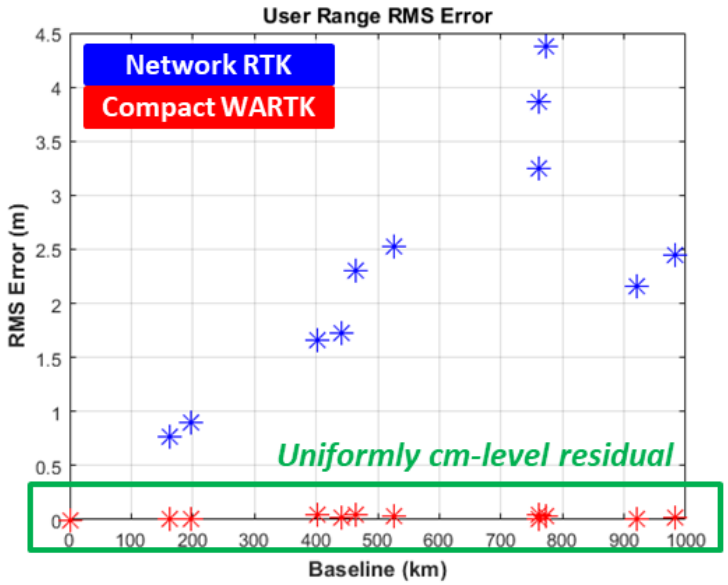

Figure 6.9 User double-differenced range errors relative to baseline distance from the master station

Table 6.4 RMS range errors of NL1 combinations of compact WARTK users

RMS Statistics	*Stable Tropo. Condition*			*Active Tropo. Condition*		
Site Name	**SIDN**	**ARGS**	**OHAS**	**NCMG**	**NCRE**	**NCTR**
ZTD Corr. Accuracy (cm)	1.0	1.3	0.5	3.2	2.4	1.5
User Range Error (cm)	1.0	1.3	1.5	4.5	4.0	3.0

Table 6.4 summarizes the ZTD correction accuracy at each user location, and the RMS residual errors of user NL1 combinations. The range residual errors of compact WARTK users are dependent on the accuracy of the tropospheric corrections. As shown by the results, the residual error is relatively larger for users located in areas with active tropospheric conditions. This results affect the performance of the ambiguity resolution to be discussed.

6.2.3 User Ambiguity Domain Analysis

The results of previous subsection shows the corrections generated through the proposed system can sufficiently reduce the satellite orbit and clock errors, ionospheric delay, and tropospheric delay to allow fixing the integer ambiguity. This subsection analyze the performance of ambiguity resolution of the compact WARTK users. As discussed in subsection 3.2.2, the success rate that indicates how accurate the fixed ambiguity is, and time-to-first-fix (TTFF), which means how quickly the integer ambiguity is determined, are analyzed as performance indicators.

The ambiguity resolution and validation for each user site was conducted 300 trials for statistical analysis of performance as shown in Figure 6.10. The TTFF is calculated as the difference between the start time of the user process trial and the time when ambiguity fixed. Figure 6.11 shows the possible outcomes from the trials of ambiguity resolution. The green areas are the regions of correct fix (success), and the red areas mean incorrect fix (failure). The light blue areas are undecided regions that is not fixed to integer. The true integer ambiguity for performance verification is determined by the RTK post-processing.

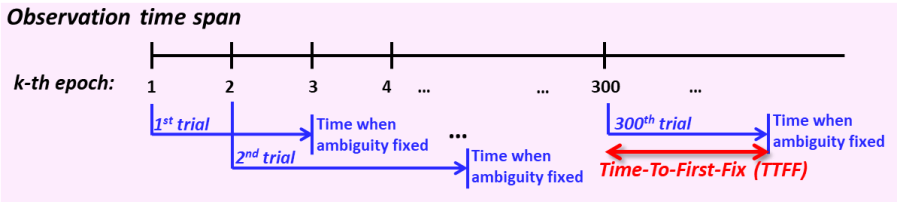

Figure 6.10 Trials of ambiguity resolution over observation time span

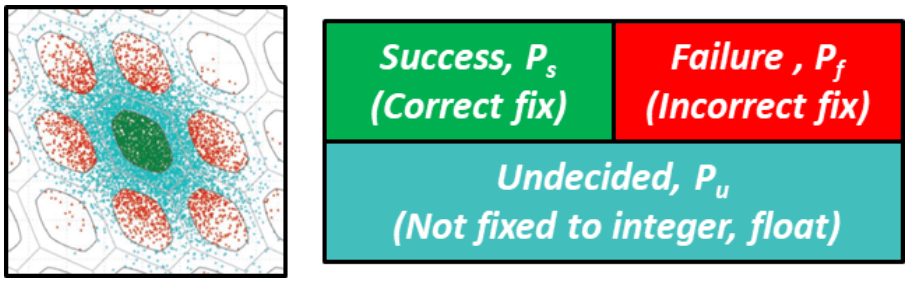

Figure 6.11 Possible outcomes from trials of the ambiguity resolution

Table 6.5 Ambiguity resolution performance of compact WARTK users.

RMS Statistics for 300 Trials	*Stable Tropo. Condition*			*Active Tropo. Condition*		
Site Name	**SIDN**	**ARGS**	**OHAS**	**NCMG**	**NCRE**	**NCTR**
Time-To-First-Fix (sec)	131 (~2 min)			208 (~3.5 min)		
Success Rate (%)	100 %			89 %		
Failure Rate (%)	0 %			11 %		
Success-Fix Rate (%)	100 %			89 %		

Table 6.5 summarizes the results of ambiguity resolution performance of compact WARTK users. The RMS statistics for 300 trials were calculated by distinguishing between users located in stable tropospheric conditions, and users located in active tropospheric conditions. As a result, the users located in stable tropospheric conditions determine their ambiguity within approximately 2 minutes with 100 % success-fix rate. On the other hand, the users fix their integer ambiguity within 3.5 minutes with 89 % success-fix probability when the tropospheric condition is active. In conclusions, because the users at stable tropospheric conditions have small residual errors, they can correctly fix ambiguity faster than the users located in active tropospheric conditions.

6.2.4 User Position Domain Analysis

In this subsection, the user position accuracy was analyzed after correctly fixing the NL integer ambiguity within a few minutes. Figure 6.12 shows the time history of horizontal position error (HPE) and vertical position error (VPE) of compact WARTK users located in stable tropospheric conditions. Figure 6.13 represents the HPE and VPE of users under active tropospheric conditions such as heavy rainfall. Table 6.6 summarizes the RMS statistics of position accuracy at each user site. As a result, the compact WARTK users can obtain the centimeter-level position anywhere in wide-area service area. In particular, the RMS HPE for all users is less than 2 cm regardless of the tropospheric environment. On the other hand, the user VPE is greatly influenced by the accuracy of zenith tropospheric corrections. the RMS VPE is larger for users located in heavy rainy areas. The SIDN site located in stable tropospheric condition have the RMS VPE less than 2 cm, while the NCTR site under the active tropospheric condition have the RMS VPE about 6 cm. That is, the position accuracy degradation occurs due to tropospheric residual error.

Table 6.6 Position accuracy performance for each user site

RMS Accuracy Statistics	*Stable Tropo. Condition*			*Active Tropo. Condition*		
Site Name	**SIDN**	**ARGS**	**OHAS**	**NCMG**	**NCRE**	**NCTR**
RMS HPE (cm)	0.7	1.1	0.7	1.0	0.9	1.6
RMS VPE (cm)	1.8	1.9	2.9	3.6	2.8	6.2

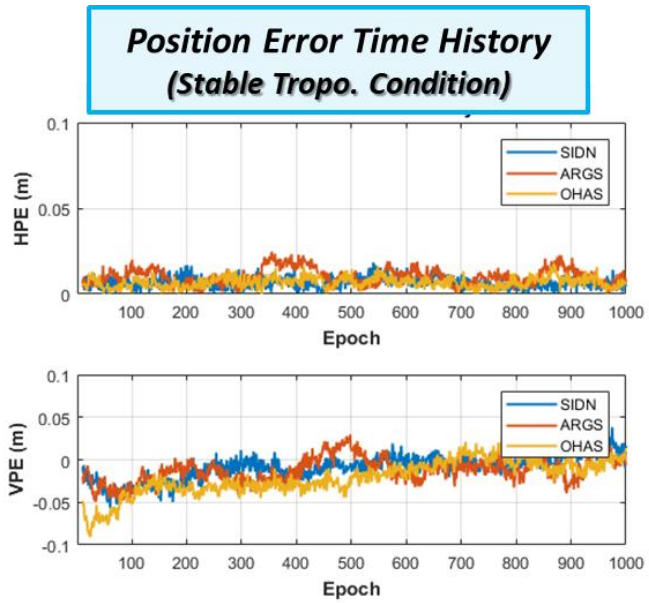

Figure 6.12 Time history of user position error (Stable tropospheric condition)

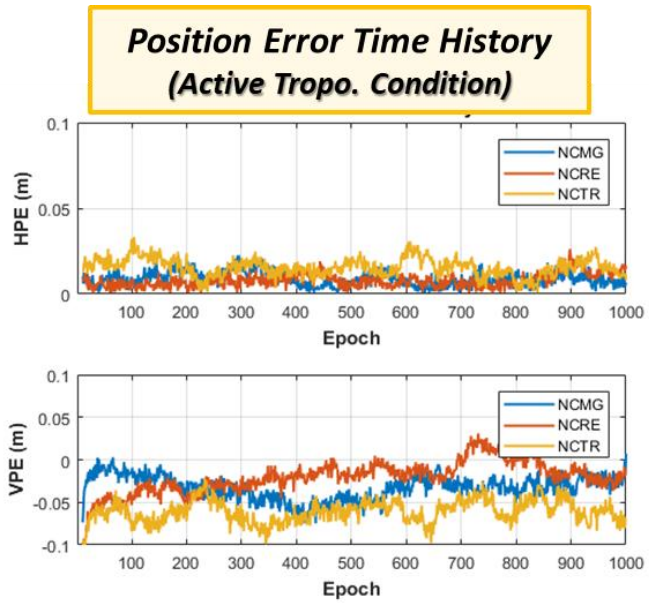

Figure 6.13 Time history of user position error (Active tropospheric condition)

Figure 6.14 shows the horizontal position error in east-north coordinates for all compact WARTK users. Figure 6.15 represents the histogram of HPE and VPE for all six users. Horizontal position errors statistically follow the Rayleigh probability distribution, and vertical errors follow the Gaussian normal distribution. Table 6.7 summarizes the accuracy statistics for all users. With RMS position accuracy, 95% and 99% cumulative position errors are statistically calculated. Generally, the 95% cumulative position error is considered as accuracy performance index for verification of navigation system. As a result, the 95% HPE and 95% VPE of compact WARTK users have 1.9 cm and 7.0 cm, respectively. The RMS HPE is 1.1 cm, and the RMS VPE is 3.5 cm. These statistics of user position accuracy satisfies the requirements of 95% HPE of 6 cm and 95% VPE of 12 cm, which are objective of the QZSS CLAS system in Japan. In conclusion, the compact WARTK system provide centimeter-level positioning service in wide-area coverage within a few minutes after correctly determining the integer ambiguity.

Table 6.7 Performance of user position accuracy

Accuracy Statistics	**RMS**	**95%**	**99%**
HPE (cm)	**1.1**	**1.9**	**2.4**
VPE (cm)	**3.5**	**7.0**	**8.3**

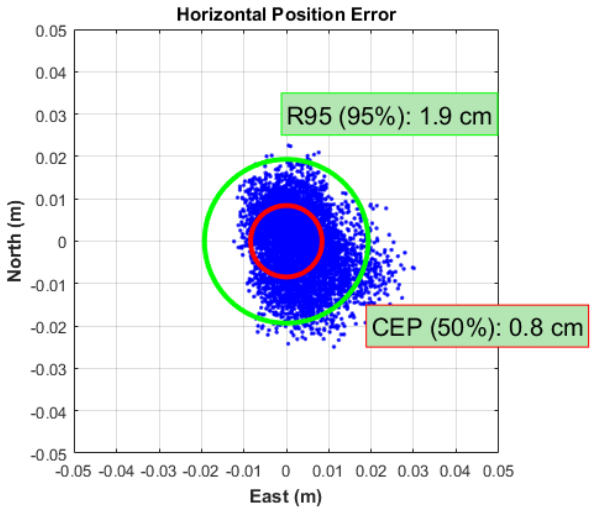

Figure 6.14 Horizontal position accuracy of all compact WARTK users

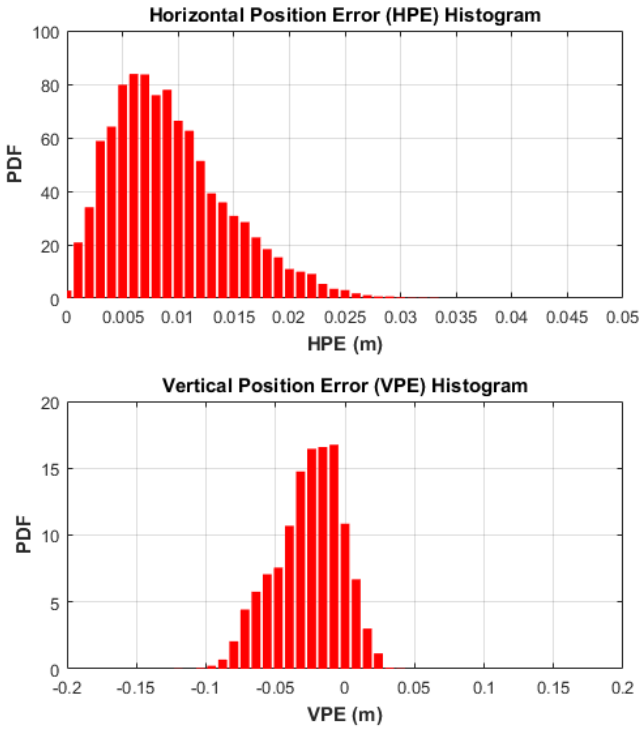

Figure 6.15 Histogram of user position error

Intentionally Blank Page

CHAPTER 7. CONCLUSIONS

This thesis proposed a new satellite augmentation system called “Compact Wide-Area RTK”. The compact wide-area RTK can provide centimeter-level positioning services in continental scale coverage using several reference stations hundreds of kilometers apart. The compact wide-area RTK corrections consist of a three-dimensional satellite orbit corrections for each satellite, satellite code/phase clock (CPC) corrections for each satellite, and corrections of the zenith tropospheric wet delay. Through the strategy of separating the scalar-type observation corrections of network RTK into vector forms of each error component, it is enable to expand network RTK coverage. Furthermore, this corrections are designed for broadcasting via a geostationary satellite with extremely low-speed data link of 250 bps likewise of legacy SBAS.

This thesis mainly discussed on the overall system architecture and core algorithms for generating carrier-phase-based corrections. Unlike the pseudorange, the carrier-phase observations contain integer ambiguity. This study proposed a new TCAR algorithm using multi-frequency signals to correctly solve the integer ambiguity in wide-area. Traditional TCAR algorithm which used geometry-free linear combinations is seriously limited to short-baseline distance due to spatial decorrelation error of ionospheric delay. On the other hand, the new method applied geometry-based ionosphere-free combinations can quickly and correctly fix the integer ambiguity without any ionospheric delay modeling or corrections. After determining the integer ambiguity between reference stations, the carrier-phase-

based precise corrections can be calculated. This study mainly proposed novel algorithms for the satellite CPC corrections and the tropospheric corrections. The algorithms for generating satellite orbit corrections are beyond the scope of this thesis. It can be produced from the process of precise orbit determination in real-time 5 cm accuracy typically.

The satellite CPC corrections of the compact wide-area RTK system are calculated based on multiple stations for superior and robust performance under communication delay and outage. The conventional RTCM RTK protocol produced by only one station is very vulnerable to latency because of the non-linearly time-varying characteristic. The proposed algorithm addressed these limitations through a wide-area network of multiple reference stations. The error sources changing non-linearly are eliminated through the compact RTK technique. The latency errors induced by ionospheric delay can be fully eliminated from ionosphere-free linear combinations. The tropospheric delay is eliminated by precisely estimation using carrier-phase observations of multiple stations. In addition, the measurements at each stations are applied in the averaging filter to improve the noise quality of the CPC corrections. As a result, the latency compensation error of CPC corrections is reduced 99% and 82% with compare to RTCM RTK (MT 1004) and compact RTK (MT 4081) protocol, respectively. Furthermore, the compact wide-area RTK can still continuously provide RTK service even in 60 seconds latency while the conventional RTK did not.

The tropospheric corrections of the compact wide-area RTK system are calculated using carrier-phase observations and weather data together. The former research for high-accuracy tropospheric correction require a lot of reference stations that are

located every 10~50 km apart. On the other hand, the proposed algorithm used only six reference stations and a few hundreds of automatic weather stations together to achieve high-accuracy within 1,000 km radius of service area. In addition, the proposed algorithm adopts the 3rd order spherical harmonics function to significantly reduce the message amounts, while accurately modeling the spatial characteristic of tropospheric delay. As a result, the accuracy of zenith tropospheric delay on user domain is about RMS 2 cm in heavy rainy day. The RMS accuracy is improved about 47% with compare to grid-based corrections of PPP-RTK using same number of GPS stations. Furthermore, the message bandwidth can be reduced by 90%. A number of grid points are generally required for continental scale area; however, the compact wide-area RTK requires only 16 coefficients as the corrections to serve the same coverage.

In order to evaluate the user domain performance of the compact wide-area RTK system, this study conducted a feasibility test on mid-west and south USA using actual GPS measurements. As a result, the 95% HPE is about 1.9 cm and the 95% VPE is 7.0 cm after the integer ambiguity is correctly fixed using GPS-only signals. The user resolves their ambiguity based on LAMBDA with fixed-failure rate test. The TTFF takes about 2 minutes, and success-fix rate is about 100 % when the tropospheric condition is stable. The performance is slightly degraded when active tropospheric condition. The TTFF is about 3.5 minutes and success-fix rate is 89%.

In conclusion, the Compact WARTK system can provide centimeter-level positioning service to wide-area coverage with extremely low-speed data link via GEO satellite. The proposed system can improve position accuracy to a few centimeter while maintaining the hardware infrastructure of the meter-level legacy

SBAS. This system also has the advantage of enabling high-accuracy positioning in wide-area, even with fewer reference stations and communication speeds than the Network RTK or PPP-RTK. We hope that this new system will consider as candidate solution for nationwide centimeter-level service such as satellite augmentation system of the Korea Positioning System (KPS).

BIBLIOGRAPHY

[1] E. D. Kaplan and C. J. Hegarty, *Understanding GPS Principles and Applications*, 2nd ed. Artech House, 2006.

[2] P. Misra and P. Enge, *Global Positioning System: Signals, Measurements, and Performance*, 2nd ed. Ganga-Jamuna Press, 2006.

[3] B. Park, "A Study on Reducing Temporal and Spatial Decorrelation Effect in GNSS Augmentation System: Consideration of the Correction Message Standardization," Ph.D. Dissertation, Seoul National University, Seoul, Korea, 2008.

[4] J. Song, "A Study on Improving Performance of Network RTK through Tropospheric Modeling for Land Vehicle Applications," Ph.D. Dissertation, Seoul National University, Seoul, Korea, 2016.

[5] J. Song, B. Park, and C. Kee, "A Study on GPS/GLONASS Compact Network RTK and Analysis on Temporal Variations of Carrier Phase Corrections for Reducing Broadcast Bandwidth," in *Proceedings of the ION 2017 Pacific PNT Meeting*, 2017, pp. 659–669.

[6] B. Park and C. Kee, "The Compact Network RTK Method: An Effective Solution to Reduce GNSS Temporal and Spatial Decorrelation Error," *Journal of Navigation*, vol. 63, no. 2, pp. 343–362, 2010.

[7] G. Wübbena, M. Schmitz, and A. Bagge, "PPP-RTK: Precise Point Positioning using State-Space Representation in RTK Networks," *Proceedings of the 18th International Technical Meeting of the Satellite Division of The Institute of Navigation, ION GNSS 2005*, vol. 2005, pp. 2584–2594, 2005.

[8] S. Han, "Carrier Phase-based Long-range GPS Kinematic Positioning," Ph.D. Dissertation, University of New South Wales, Sydney, Australia, 1997.

[9] H. J. Euler, C. R. Keenan, and B. E. Zebhause, "Study of a Simplified Approach in Utilizing Information from Permanent Reference Station Arrays," in *Proceedings of the 14th International Technical Meeting of the Satellite Division of The Institute of Navigation (ION GPS 2001)*, 2001.

[10] U. Vollath, A. Buecherl, H. Landau, C. Pagels, and B. Wagner, "Multi-Base RTK Positioning Using Virtual Reference Stations," in *Proceedings of the 13th International Technical Meeting of the Satellite Division of The Institute of Navigation (ION GPS 2000)*, 2000, pp. 123–131.

[11] G. Wübbena, A. Bagge, and M. Schmitz, "Network-Based Techniques for RTK Applications," in *Proceedings of the GPS Symposium, GPS JIN 2001*,

2001.

[12] RTCM Special Committee 104, “RTCM Standard 10403.3 Differential GNSS Services - Version 3,” 10403.3, 2016.

[13] C. Kee and J. Kim, “Efficient Transmission Technique of Compact RTK Correction Messages for Low-rate RTK Data-link,” in *Proceedings of the 15th International Technical Meeting of the Satellite Division of The Institute of Navigation (ION GPS 2002)*, 2002, pp. 1361–1371.

[14] J. Kim and C. Kee, “RTK-GPS Correction Generation Technique for Low-Rate Data-Link,” *Journal of Navigation*, vol. 57, no. 3, pp. 465–477, 2004.

[15] J. Song, “A New Approach of Latency Error Compensation Using Compact RTK for GPS/GLONASS Signals,” in *57th Meeting of the Civil GPS Service Interface Committee At the Institute of Navigation GNSS+ 2017 Conference*, 2017.

[16] M. Hernández-Pajares, J. M. J. Zornoza, J. S. Subirana, and O. L. Colombo, “Feasibility of wide-area subdecimeter navigation with GALILEO and modernized GPS,” *IEEE Transactions on Geoscience and Remote Sensing*, vol. 41, no. 9 PART II, pp. 2128–2131, 2003.

[17] M. Hernandez-Pajares *et al.*, “Wide-Area RTK: High Precision Positioning on a Continental Scale,” *Inside GNSS March/April 2010*, pp. 35–46, 2010.

[18] D. Odijk *et al.*, “LAMBDA-Based Ambiguity Resolution for Next-Generation GNSS Wide-Area RTK,” in *Proceedings of the 2010 International Technical Meeting of The Institute of Navigation*, 2010, pp. 566–576.

[19] B. Forssell, M. Martin-Neira, and R. A. Harrisz, “Carrier Phase Ambiguity Resolution in GNSS-2,” in *Proceedings of the 10th International Technical Meeting of the Satellite Division of The Institute of Navigation (ION GPS 1997)*, 1997, pp. 1727–1736.

[20] J. M. Juan *et al.*, “Wide Area RTK: A satellite navigation system based on precise real-time ionospheric modelling,” *Radio Science*, vol. 47, no. 2, Apr. 2012.

[21] M. Hernández-Pajares, J. M. Juan, J. Sanz, R. Orús, A. García-Rodríguez, and O. L. Colombo, “Wide area real time kinematics with Galileo and GPS signals,” in *Proceedings of the 17th International Technical Meeting of the Satellite Division of The Institute of Navigation (ION GNSS 2004)*, 2004, pp. 2541–2554.

[22] J. F. Zumberge, M. B. Heflin, D. C. Jefferson, M. M. Watkins, and F. H. Webb, “Precise point positioning for the efficient and robust analysis of GPS data from large networks,” *Journal of Geophysical Research: Solid Earth*, vol. 102, no. B3, pp. 5005–5017, Mar. 1997.

[23] S. Bisnath and Y. Gao, “Current State of Precise Point Positioning and Future Prospects and Limitations,” in *Observing our Changing Earth*, Berlin, Heidelberg: Springer Berlin Heidelberg, 2009, pp. 615–623.

[24] P. J. G. Teunissen and A. Khodabandeh, “Review and principles of PPP-RTK methods,” *Journal of Geodesy*, vol. 89, no. 3, pp. 217–240, Mar. 2015.

[25] M. Miya, Y. Sato, S. Fujita, N. Motooka, M. Saito, and J. Takiguchi, “Centimeter Level Augmentation Service (CLAS) in Japanese Quasi-Zenith Satellite System, its User Interface, Detailed Design, and Plan,” in *Proceedings of the 27th International Technical Meeting of the Satellite Division of The Institute of Navigation (ION GNSS+ 2014)*, 2014, pp. 645–652.

[26] M. Miya *et al.*, “Centimeter Level Augmentation Service (CLAS) in Japanese Quasi-Zenith Satellite System, Design for Satellite Based RTK-PPP Services,” in *Proceedings of the 28th International Technical Meeting of the Satellite Division of The Institute of Navigation (ION GNSS+ 2015)*, 2015, pp. 1958–1962.

[27] M. Miya, S. Fujita, Y. Sato, K. Ota, R. Hirokawa, and J. Takiguchi, “Centimeter Level Augmentation Service (CLAS) in Japanese Quasi-Zenith Satellite System, its User Interface, Detailed Design, and Plan,” in *Proceedings of the 29th International Technical Meeting of the Satellite Division of The Institute of Navigation (ION GNSS+ 2016)*, 2016, pp. 2864–2869.

[28] R. Hirokawa, Y. Sato, J. Takiguchi, and R. Yasumitsu, “Compact SSR Messages for Satellite Based Nation-Wide PPP-RTK,” in *International Symposium on GNSS 2015*, 2015, pp. 483–486.

[29] R. Hirokawa, Y. Sato, S. Fujita, and M. Miya, “Compact SSR Messages with Integrity Information for Satellite Based PPP-RTK Service,” in *Proceedings of the 29th International Technical Meeting of the Satellite Division of The Institute of Navigation (ION GNSS+ 2016)*, 2016, pp. 3372–3376.

[30] Cabinet Office, “Quasi-Zenith Satellite System Interface Specification Centimeter Level Augmentation Service,” IS-QZSS-L6-001, 2017.

[31] D. Kim, M. Park, and C. Kee, “Preliminary Test Results of Compact Wide-Area RTK: A New Satellite-Based Augmentation System for Centimeter-Level Service,” in *Proceedings of the 32nd International Technical Meeting of the Satellite Division of The Institute of Navigation (ION GNSS+ 2019)*, 2019, pp. 3708–3716.

[32] D. Kim, B. Kim, S. Yu, D. Han, J. Song, and C. Kee, “A Real-Time High-Accuracy Tropospheric Correction Generation Method for Compact Wide-Area RTK,” in *Proceedings of IInternational Symposium on GNSS (ISGNSS)*

2019 in conjunction with Institute of Positioning, Navigation and Timing (IPNT) Conference, 2019, pp. 301–307.

[33] D. Kim and C. Kee, "Compact Wide-Area RTK: A New Centimeter-Level Satellite-Based Augmentation System Using Carrier-Phase Observations," in *Proceedings of IInternational Symposium on GNSS (ISGNSS) 2019 in conjunction with Institute of Positioning, Navigation and Timing (IPNT) Conference*, 2019, pp. 363–366.

[34] "Official U.S. Government Information about the Global Positioning System (GPS)." [Online]. Available: https://www.gps.gov/systems/gps/.

[35] C. Kee, "Wide Area Differential GPS (WADGPS)," Ph.D. Dissertation, Stanford University, Stanford, CA, 1994.

[36] C. Kee, T. Walter, P. Enge, and B. Parkinson, "Quality Control Algorithms on WAAS Wide Area Reference Stations," *Navigation, Journal of the Institute of Navigation*, vol. 44, no. 1, pp. 53–62, 1997.

[37] B. Li, L. Lou, and Y. Shen, "GNSS Elevation-Dependent Stochastic Modeling and Its Impacts on the Statistic Testing," *Journal of Surveying Engineering*, vol. 142, no. 2, p. 04015012, May 2016.

[38] B. DeCleene, "Defining Pseudorange Integrity - Overbounding," in *Proceedings of the 13th International Technical Meeting of the Satellite Division of The Institute of Navigation (ION GPS 2000)*, 2000, no. September, pp. 1916–1924.

[39] R. Dach, S. Lutz, P. Walser, and P. Fridez, *Bernese GNSS Software Version 5.2*. Astronomical Institute, University of Bern, 2015.

[40] D. Han, D. Kim, and C. Kee, "Improving performance of GPS satellite DCB estimation for regional GPS networks using long-term stability," *GPS Solutions*, vol. 22, no. 1, p. 13, Jan. 2018.

[41] A. Hauschild and O. Montenbruck, "The Effect of Correlator and Front-End Design on GNSS Pseudorange Biases for Geodetic Receivers," *Navigation, Journal of the Institute of Navigation*, vol. 63, no. 4, pp. 443–453, Dec. 2016.

[42] NAVSTAR GPS, "Navstar GPS Space Segment/Navigation User Interfaces," IS-GPS-200D, Revision D, 2004.

[43] NAVSTAR GPS, "Navstar GPS Space Segment/User Segment L5 Interface," IS-GPS-705D, 2013.

[44] G. Okerson, J. Ross, A. Tetewsky, A. Soltz, J. Anszperger, and Stephen R. Smith JR., "Inter-Signal Correction Sensitivity Analysis: Aperture-Dependent Delays Induced by Antenna Anisotropy in Modernized," *Inside GNSS May/June 2016*, 2016.

[45] A. El-Mowafy, M. Deo, and C. Rizos, “On biases in precise point positioning with multi-constellation and multi-frequency GNSS data,” *Measurement Science and Technology*, vol. 27, no. 3, p. 035102, Mar. 2016.

[46] M. Håkansson, A. B. O. Jensen, M. Horemuz, and G. Hedling, “Review of code and phase biases in multi-GNSS positioning,” *GPS Solutions*, vol. 21, no. 3, pp. 849–860, Jul. 2017.

[47] M. Håkansson, “Satellite dependency of GNSS phase biases between receivers and between signals,” *Journal of Geodetic Science*, vol. 7, no. 1, pp. 130–140, Nov. 2017.

[48] S. Banville, R. Santerre, M. Cocard, and R. B. Langley, “Satellite and Receiver Phase Bias Calibration for Undifferenced Ambiguity Resolution,” in *Proceedings of the 2008 National Technical Meeting of The Institute of Navigation*, 2008, pp. 711–719.

[49] C. Cai, “Precise point positioning using dual-frequency GPS and GLONASS measurements,” Master Thesis, University of Calary, Calgary, Canada, 2009.

[50] J. Kouba, “A Guide to Using International GNSS Service (IGS) Products,” Geodetic Survey Division, Natural Resources Canada, 2009.

[51] R. Schmid, P. Steigenberger, G. Gendt, M. Ge, and M. Rothacher, “Generation of a consistent absolute phase-center correction model for GPS receiver and satellite antennas,” *Journal of Geodesy*, vol. 81, no. 12, pp. 781–798, Nov. 2007.

[52] P. Zeimetz and H. Kuhlmann, “On the Accuracy of Absolute GNSS Antenna Calibration and the Conception of a New Anechoic Chamber,” in *Proceedings of the FIG Working Week 2008*, 2008.

[53] G. Beyerle, “Carrier Phase Wind-up in GPS Reflectometry,” *GPS Solutions*, vol. 13, no. 3, pp. 191–198, Jul. 2009.

[54] G. Petit and B. Luzum, “IERS Conventions (2010),” IERS Technical Note No. 36, 2010.

[55] G. Xu, *GPS: Theory, Algorithms and Applications*. Springer Berlin Heidelberg, 2007.

[56] H. Spicakova, “VIE_MOD stations corrections,” in *VieVS User Workshop*, 2011.

[57] N. Ashby, “Relativity in the Global Positioning System,” *Living Reviews in Relativity*, vol. 6, no. 1, p. 1, Dec. 2003.

[58] Ž. Hećimović, “Relativistic Effects on Satellite Navigation,” *Tehnicki Vjesnik*, vol. 20, no. 1, pp. 195–203, 2013.

[59] J. Kim *et al.*, “Accuracy Improvement of DGPS for Low-Cost Single-

Frequency Receiver Using Modified Flächen Korrektur Parameter Correction," *ISPRS International Journal of Geo-Information*, vol. 6, no. 7, p. 222, Jul. 2017.

[60] C. Kee, B. W. Parkinson, and P. Axelrad, "Wide Area Differential GPS," *Navigation*, vol. 38, no. 2, pp. 123–145, Jun. 1991.

[61] D. Kim, "A Study on Correction Generation Algorithms for Wide Area Differential GNSS," Ph.D. Dissertation, Seoul National University, Seoul, Korea, 2007.

[62] D. Han, "A Study on Improving the Accuracy of SBAS Ionosphere Correction by Applying Double-Difference Carrier Phase Measurements," Ph.D. Dissertation, Seoul National University, Seoul, Korea, 2018.

[63] RTCA Special Committee 159, "Minimum Operational Performance Standards for Global Positioning System/Wide Area Augementation System Airborne Equipment," Washington, DC, RTCA/DO-229D, 2006.

[64] D. Kim *et al.*, "A Study of SBAS Position Domain Analysis Method: WAAS and EGNOS Performance Evaluation," *Journal of Positioning, Navigation, and Timing*, vol. 5, no. 4, pp. 203–211, Dec. 2016.

[65] D. Kim *et al.*, "Modified Kriging Based Double-Difference Tropospheric Correction Interpolation Method for Network RTK User," in *Proceedings of the 30th International Technical Meeting of the Satellite Division of The Institute of Navigation (ION GNSS+ 2017)*, 2017, vol. 6, pp. 4090–4102.

[66] F. Takac and O. Zelzer, "The Relationship Between Network RTK Solutions MAC, VRS, PRS, FKP and i-MAX," in *Proceedings of the 21st International Technical Meeting of the Satellite Division of The Institute of Navigation (ION GNSS 2008)*, 2008, pp. 348–355.

[67] National Geodetic Survey, "Guidelines for New and Existing Continuously Operating Reference Stations (CORS)," 2018.

[68] NASA, "Introduction to JPL's GPS Time Series," 2016.

[69] G. Xie *et al.*, "Integrity Design and Updated Test Results for the Stanford LAAS Integrity Monitor Testbed," in *Proceedings of the 57th Annual Meeting of The Institute of Navigation (2001)*, 2001, pp. 681–693.

[70] H. Yun, "A Study on GNSS User Integrity Monitoring Algorithm for Simultaneous Multiple Satellite Failures," Ph.D. Dissertation, Seoul National University, Seoul, Korea, 2013.

[71] R. E. Phelts and D. M. Akos, "Effects of Signal Deformations on Modernized GNSS Signals," *Journal of Global Positioning Systems*, vol. 5, no. 1&2, pp. 2–10, 2006.

[72] S. B. Bisnath, D. Kim, and R. B. Langley, “A New Approach to an Old Problem: Carrier-Phase Cycle Slips,” *GPS World*, vol. 13, no. 4, pp. 42–49, 2001.

[73] X. Luo, Z. Liu, Y. Lou, S. Gu, and B. Chen, “A Study of Multi-GNSS Ionospheric Scintillation and Cycle-Slip over Hong Kong Region for Moderate Solar Flux Conditions,” *Advances in Space Research*, vol. 60, no. 5, pp. 1039–1053, 2017.

[74] Y. Gao and Z. Li, “Cycle Slip Detection and Ambiguity Resolution Algorithms for Dual-Frequency GPS Data Processing,” *Marine Geodesy*, vol. 22, no. 3, pp. 169–181, 1999.

[75] C. Cai, Z. Liu, P. Xia, and W. Dai, “Cycle Slip Detection and Repair for Undifferenced GPS Observations Under High Ionospheric Activity,” *GPS Solutions*, vol. 17, no. 2, pp. 247–260, 2013.

[76] T. Zeng *et al.*, “Real-Time Triple-Frequency Cycle Slip Detection and Repair Method Under Ionospheric Disturbance Validated with BDS Data,” *GPS Solutions*, vol. 22, no. 3, pp. 1–13, 2018.

[77] D. Kim and R. B. Langley, “Instantaneous Real-time Cycle-slip Correction of Dual-frequency GPS Data,” in *Proceedings of the International Symposium on Kinematic Systems in Geodesy, Geomatics and Navigation*, 2001, pp. 255–264.

[78] D. Kim, J. Song, S. Yu, C. Kee, and M. Heo, “A New Algorithm for High-Integrity Detection and Compensation of Dual-Frequency Cycle Slip under Severe Ionospheric Storm Conditions,” *Sensors*, vol. 18, no. 11, p. 3654, 2018.

[79] K. Shallberg, P. Shloss, E. Altshuler, and L. Tahmazyan, “WAAS Measurement Processing, Reducing the Effects of Multipath,” in *Proceedings of the 14th International Technical Meeting of the Satellite Division of The Institute of Navigation (ION GPS 2001)*, 2001, pp. 2334–2340.

[80] K. Shallberg and Fang Sheng, “WAAS Measurement Processing; Current Design and Potential Improvements,” in *2008 IEEE/ION Position, Location and Navigation Symposium*, 2008, pp. 253–262.

[81] P. Y. Hwang, G. A. McGraw, and J. R. Bader, “Enhanced Differential GPS Carrier-Smoothed Code Processing Using Dual-Frequency Measurements,” *Navigation, Journal of the Institute of Navigation*, vol. 46, no. 2, pp. 127–137, Jun. 1999.

[82] G. A. McGraw and R. S. Y. Young, “Dual frequency smoothing DGPS performance evaluation studies,” in *Proceedings of the 2005 National Technical Meeting of The Institute of Navigation*, 2005, pp. 170–181.

[83] B. Park, C. Lim, Y. Yun, E. Kim, and C. Kee, “Optimal Divergence-Free

Hatch Filter for GNSS Single-Frequency Measurement," *Sensors*, vol. 17, no. 3, p. 448, Feb. 2017.

[84] S. Yu, D. Kim, J. Song, and C. Kee, "Covariance Analysis of Real-Time Precise GPS Orbit Estimated from Double-Differenced Carrier Phase Observations," *Remote Sensing*, vol. 11, no. 19, p. 2271, Sep. 2019.

[85] P. J. G. Teunissen, "GNSS Integer Ambiguity Validation : Overview of Theory and Methods," in *Proceedings of the ION 2013 Pacific PNT Meeting*, 2013, pp. 673–684.

[86] P. J. G. Teunissen, P. J. De Jonge, and C. C. J. M. Tiberius, "Performance of the LAMBDA Method for Fast GPS Ambiguity Resolution," *Navigation, Journal of the Institute of Navigation*, vol. 44, no. 3, pp. 373–383, Sep. 1997.

[87] P. J. G. Teunissen, P. Joosten, and C. Tiberius, "A Comparison of TCAR, CIR and LAMBDA GNSS Ambiguity Resolution," in *Proceedings of the 15th International Technical Meeting of the Satellite Division of The Institute of Navigation (ION GPS 2002)*, 2002, pp. 2799–2808.

[88] X. W. Chang, X. Yang, and T. Zhou, "MLAMBDA: a modified LAMBDA method for integer least-squares estimation," *Journal of Geodesy*, vol. 79, no. 9, pp. 552–565, Dec. 2005.

[89] S. Verhagen and P. J. G. Teunissen, "The ratio test for future GNSS ambiguity resolution," *GPS Solutions*, vol. 17, no. 4, pp. 535–548, 2013.

[90] Y. Hou, S. Verhagen, and J. Wu, "An Efficient Implementation of Fixed Failure-Rate Ratio Test for GNSS Ambiguity Resolution," *Sensors*, vol. 16, no. 7, p. 945, Jun. 2016.

[91] S. Han, "Quality-control issues relating to instantaneous ambiguity resolution for real-time GPS kinematic positioning," *Journal of Geodesy*, vol. 71, no. 6, pp. 351–361, May 1997.

[92] S. Verhagen, "Integer ambiguity validation: an open problem?," *GPS Solutions*, vol. 8, no. 1, pp. 36–43, Apr. 2004.

[93] S. Feng, W. Ochieng, T. Moore, C. Hill, and C. Hide, "Carrier phase-based integrity monitoring for high-accuracy positioning," *GPS Solutions*, vol. 13, no. 1, pp. 13–22, 2009.

[94] S. Feng *et al.*, "Integrity Monitoring for Carrier Phase Ambiguities," *Journal of Navigation*, vol. 65, no. 1, pp. 41–58, Jan. 2012.

[95] P. J. G. Teunissen and D. Odijk, "Ambiguity Dilution of Precision: Definition, Properties and Application," in *Proceedings of the 10th International Technical Meeting of the Satellite Division of The Institute of Navigation (ION GPS 1997)*, 1997, pp. 891–899.

[96] P. J. G. Teunissen, “Success Probability of Integer GPS Ambiguity Rounding and Bootstrapping,” *Journal of Geodesy*, vol. 72, no. 10, pp. 606–612, Oct. 1998.

[97] S. Han and C. Rizos, “The Impact of Two Additional Civilian GPS Frequencies on Ambiguity Resolution Strategies,” in *Proceedings of the 55th Annual Meeting of The Institute of Navigation (1999)*, 1999, pp. 315–321.

[98] Y. Feng and B. Li, “A benefit of multiple carrier gnss signals: Regional scale network-based RTK with doubled inter-station distances,” *Journal of Spatial Science*, vol. 53, no. 2, pp. 135–147, 2008.

[99] B. Li, “Review of triple-frequency GNSS: ambiguity resolution, benefits and challenges,” *The Journal of Global Positioning Systems*, vol. 16, no. 1, p. 1, Dec. 2018.

[100] B. Li, Y. Feng, W. Gao, and Z. Li, “Real-time kinematic positioning over long baselines using triple-frequency BeiDou signals,” *IEEE Transactions on Aerospace and Electronic Systems*, vol. 51, no. 4, pp. 3254–3269, 2015.

[101] W. Tang, M. Shen, C. Deng, J. Cui, and J. Yang, “Network-based triple-frequency carrier phase ambiguity resolution between reference stations using BDS data for long baselines,” *GPS Solutions*, vol. 22, no. 3, p. 73, Jul. 2018.

[102] C. Jia, L. Zhao, L. Li, H. Li, J. Cheng, and Z. Li, “Improving the triple-carrier ambiguity resolution with a new ionosphere-free and variance- restricted method,” *Remote Sensing*, vol. 9, no. 11, 2017.

[103] M. Cocard, S. Bourgon, O. Kamali, and P. Collins, “A systematic investigation of optimal carrier-phase combinations for modernized triple-frequency GPS,” *Journal of Geodesy*, vol. 82, no. 9, pp. 555–564, 2008.

[104] T. Geng, P. Zhang, W. Wang, and X. Xie, “Comparison of Ultra-Rapid Orbit Prediction Strategies for GPS, GLONASS, Galileo and BeiDou,” *Sensors*, vol. 18, no. 2, p. 477, Feb. 2018.

[105] International Standards and Recommended Practices, “Aeronautical Telecommunications, Volume 1, Radio Navigation Aids,” Annex 10, Sixth Edition, 2006.

[106] J. Kim, “A Study on GPS-RTK Corrections Suitable for Low-rate Data-link,” Ph.D. Dissertation, Seoul National University, Seoul, Korea, 2005.

[107] C. Kee, J. Kim, S. Kim, J. Kim, and Sanghyeon Lee, “Test Results of RTK-GPS using Low-rate Data-link,” in *Proceedings of the 2004 National Technical Meeting of The Institute of Navigation*, 2004, pp. 462–468.

[108] J. Kim and C. Kee, “A Proposal of New Correction Data Format for Real-time Kinematic GPS Positioning,” in *Proceedings of the 2002 National Technical Meeting of The Institute of Navigation*, 2002, pp. 854–862.

[109] J. Kim, B. Park, C. Kee, A. Cleveland, M. Parsons, and D. Wolfe, "Budget Analysis and Realization of Precise RTK-GPS Via Compact Correction Messages Applied to Commercial GPS Receivers," in *Proceedings of the 17th International Technical Meeting of the Satellite Division of The Institute of Navigation (ION GNSS 2004)*, 2004, pp. 1460–1467.

[110] B. Park, J. Kim, and C. Kee, "RRC Unnecessary for DGPS Messages," *IEEE Transactions on Aerospace and Electronic Systems*, vol. 42, no. 3, pp. 1149–1160, 2006.

[111] M. Olynik, "Temporal Characteristics of GPS Error Sources and Their Impact on Relative Positioning," M.S. Thesis, The University of Calgary, Calgary, Canada, 2002.

[112] M. Olynik, M. Petovello, M. Cannon, and G. Lachapelle, "Temporal Impact of Selected GPS Errors on Point Positioning," *GPS Solutions*, vol. 6, no. 1–2, pp. 47–57, 2002.

[113] D. Han, H. Yun, and C. Kee, "Modeling of GPS measurement noise for estimating smoothed pseudorange and ionospheric delay," *The Journal of Korea Navigation Institute*, vol. 16, no. 4, pp. 602–610, Aug. 2012.

[114] J. B. Neumann, A. Manz, T. J. Ford, and O. Mulyk, "Test results from a new 2 cm real time kinematic GPS positioning system," in *Proceedings of the 9th International Technical Meeting of the Satellite Division of The Institute of Navigation (ION GPS 1996)*, 1996, vol. 1, pp. 873–882.

[115] J. Saastamoinen, "Atmospheric Correction for the Troposphere and Stratosphere in Radio Ranging Satellites," *The Use of Artificial Satellites for Geodesy, Geophysics Monograph Series*, vol. 15, pp. 247–251, Mar. 1972.

[116] P. Collins, R. Langley, and J. LaMance, "Limiting factors in tropospheric propagation delay error modelling for GPS airborne navigation," in *Proceedings of the 52nd Annual Meeting of The Institute of Navigation (1996)*, 1996, pp. 519–528.

[117] Y. Gao, Z. Li, and J. F. McLellan, "Carrier Phase Based Regional Area Differential GPS for Decimeter-Level Positioning and Navigation," in *Proceedings of the 10th International Technical Meeting of the Satellite Division of The Institute of Navigation (ION GPS 1997)*, 1997, pp. 1305–1313.

[118] L. Wanninger, "Improved Ambiguity Resolution by Regional Differential Modelling of the Ionosphere," in *Proceedings of the 8th International Technical Meeting of the Satellite Division of The Institute of Navigation (ION GPS 1995)*, 1995, pp. 55–62.

[119] S. Han and C. Rizos, "GPS network design and error mitigation for real-time continuous array monitoring systems," in *Proceedings of the 9th International Technical Meeting of the Satellite Division of The Institute of Navigation (ION*

GPS 1996), 1996, pp. 1827–1836.

[120] S. Han and C. Rizos, "An Instantaneous Ambiguity Resolution Technique for Medium-Range GPS Kinematic Positioning," *Navigation, Journal of the Institute of Navigation*, vol. 47, no. 1, pp. 17–31, Mar. 2000.

[121] G. Fotopoulos and M. E. Cannon, "An Overview of Multi-Reference Station Methods for cm-Level Positioning," *GPS Solutions*, vol. 4, no. 3, pp. 1–10, Jan. 2001.

[122] L. Dai, S. Han, J. Wang, and C. Rizos, "Comparison of interpolation algorithms in network-based GPS techniques," *Navigation, Journal of the Institute of Navigation*, vol. 50, no. 4, pp. 277–293, 2003.

[123] A. M. Al-shaery, S. Lim, and C. Rizos, "Functional Models of Ordinary Kriging for Medium Range Real-time Kinematic Positioning Based on the Virtual Reference Station Technique," in *Proceedings of the 23rd International Technical Meeting of the Satellite Division of The Institute of Navigation (ION GNSS 2010)*, 2010, pp. 2513–2521.

[124] A. Al-Shaery, S. Lim, and C. Rizos, "Investigation of Different Interpolation Models Used in Network-RTK for the Virtual Reference Station Technique," *Journal of Global Positioning Systems*, vol. 10, no. 2, pp. 136–148, Dec. 2011.

[125] J. Song, B. Park, and C. Kee, "Comparative Analysis of Height-Related Multiple Correction Interpolation Methods with Constraints for Network RTK in Mountainous Areas," *Journal of Navigation*, vol. 69, no. 5, pp. 991–1010, 2016.

[126] J. Mendez Astudillo, L. Lau, Y.-T. Tang, and T. Moore, "Analysing the Zenith Tropospheric Delay Estimates in On-line Precise Point Positioning (PPP) Services and PPP Software Packages," *Sensors*, vol. 18, no. 2, p. 580, Feb. 2018.

[127] A. E. Niell, "Global mapping functions for the atmosphere delay at radio wavelengths," *Journal of Geophysical Research: Solid Earth*, vol. 101, no. B2, pp. 3227–3246, Feb. 1996.

[128] J. Boehm, A. Niell, P. Tregoning, and H. Schuh, "Global Mapping Function (GMF): A new empirical mapping function based on numerical weather model data," *Geophysical Research Letters*, vol. 33, no. 7, pp. 3–6, 2006.

[129] D. Landskron and J. Böhm, "VMF3/GPT3: refined discrete and empirical troposphere mapping functions," *Journal of Geodesy*, vol. 92, no. 4, pp. 349–360, Apr. 2018.

[130] M. Elsobeiey and M. El-Diasty, "Impact of Tropospheric Delay Gradients on Total Tropospheric Delay and Precise Point Positioning," *International Journal of Geosciences*, vol. 07, no. 05, pp. 645–654, 2016.

[131] N. Takeichi, T. Sakai, S. Fukushima, and K. Ito, “Tropospheric Delay Correction with Dense GPS Network in L1-SAIF Augmentation,” *GPS Solutions*, vol. 14, no. 2, pp. 185–192, Mar. 2010.

[132] H. Zhang, Y. Yuan, W. Li, B. Zhang, and J. Ou, “A grid-based tropospheric product for China using a GNSS network,” *Journal of Geodesy*, vol. 92, no. 7, pp. 765–777, Jul. 2018.

[133] Y. Zheng, Y. Feng, and Z. Bai, “Grid Residual Tropospheric Corrections for Improved Differential GPS Positioning Over the Victoria GPS Network (GPSnet),” *Journal of Global Positioning Systems*, vol. 4, no. 1&2, pp. 284–290, 2005.

[134] T. Yanxin, L. Lilong, and Y. Chaolong, “Empirical model for mean temperature and assessment of precipitable water vapor derived from GPS,” *Geodesy and Geodynamics*, vol. 4, no. 4, pp. 51–56, 2013.

[135] H. W. Janes, R. B. Langley, and S. P. Newby, “Analysis of tropospheric delay prediction models: comparisons with ray-tracing and implications for GPS relative positioning,” *Bulletin Géodésique*, vol. 65, no. 3, pp. 151–161, Sep. 1991.

[136] NOAA, DoD, FAA, and US Navy, “Automated Surface Observing System (ASOS) User’s Guide,” 1998.

[137] “National Weather Service: Pressure Definitions.” [Online]. Available: https://www.weather.gov/bou/pressure_definitions.

[138] A. L. Berman, “The Prediction of Zenith Range Refraction from Surface Measurments of Meteorological Parameters,” JPL TR-32-1602 California Intitute of Technology, 1976.

[139] S. A.-M. Younes, “Modeling investigation of wet tropospheric delay error and precipitable water vapor content in Egypt,” *The Egyptian Journal of Remote Sensing and Space Science*, vol. 19, no. 2, pp. 333–342, Dec. 2016.

[140] J. L. Davis, T. A. Herring, I. I. Shapiro, A. E. E. Rogers, and G. Elgered, “Geodesy by radio interferometry: Effects of atmospheric modeling errors on estimates of baseline length,” *Radio Science*, vol. 20, no. 6, pp. 1593–1607, Nov. 1985.

[141] J. Askne and H. Nordius, “Estimation of tropospheric delay for microwaves from surface weather data,” *Radio Science*, vol. 22, no. 3, pp. 379–386, May 1987.

[142] S. M. Robeson, “Spherical Methods for Spatial Interpolation: Review and Evaluation,” *Cartography and Geographic Information Science*, vol. 24, no. 1, pp. 3–20, 1997.

[143] Y. Gao and Z. Z. Liu, “Precise Ionosphere Modeling Using Regional GPS

Network Data," *Journal of Global Positioning Systems*, vol. 1, no. 1, pp. 18–24, Jun. 2002.

[144] D. Han, D. Kim, J. Song, and C. Kee, "Improving the Accuracy of Regional Ionospheric Mapping with Double-Difference Carrier Phase Measurement," *Remote Sensing*, vol. 11, no. 16, p. 1849, Aug. 2019.

[145] S. Schaer, G. Beutler, L. Mervart, M. Rothacher, and U. Wild, "Global and regional ionosphere models using the GPS double difference phase observable," in *Proceeding of the 1995 IGS Workshop*, 1995, pp. 77–92.

[146] Y. Yao, Y. Hu, C. Yu, B. Zhang, and J. Guo, "An improved global zenith tropospheric delay model GZTD2 considering diurnal variations," *Nonlinear Processes in Geophysics*, vol. 23, no. 3, pp. 127–136, May 2016.

[147] Y. Yao, X. Xu, C. Xu, W. Peng, and Y. Wan, "Establishment of a Real-Time Local Tropospheric Fusion Model," *Remote Sensing*, vol. 11, no. 11, p. 1321, Jun. 2019.

[148] Y.-J. Tsai, "Wide Area Differential Operation of the Global Positioning System: Ephemeris and Clock Algorithms," Ph.D. Dissertation, Stanford University, Stanford, CA, 1999.

[149] "NRCan: CSRS-PPP Service." [Online]. Available:

https://webapp.geod.nrcan.gc.ca/geod/tools-outils/ppp.php?locale=en.

Intentionally Blank Page

초 록

센티미터 급 광역 보강항법 시스템의 반송파 위상 기반 보정정보 생성 알고리즘에 관한 연구

김 동 욱
서울대학교 대학원
기계항공공학부

최근 자율주행자동차, 무인 드론 배송, 충돌 회피, 무인트랙터를 이용한 스마트 무인 경작 등 위성항법시스템(GNSS, Global Navigation Satellite System)을 사용하는 다양한 응용분야에서 수 cm 수준의 정밀 위치 정보에 대한 요구가 급격히 증가하고 있다. 본 학위논문에서는 1 m 급의 정확하고 신뢰성 높은 위치 서비스를 제공하는 기존의 정지궤도위성 기반 광역 보강항법 시스템(SBAS, Satellite-Based Augmentation System)의 기준국 인프라를 유지하면서 항법 성능을 수 cm 수준으로 향상시키기 위해 반송파 위상 기반의 초정밀 보정정보 생성 알고리즘에 관한 연구를 수행하였다.

실시간 정밀 측위(RTK, Real-Time Kinematic)는 반송파 위상 측정치에 포함된 미지정수를 정확하게 결정하여 수 cm 수준의 정밀 항법 서비스를 가능하게 하는 대표적인 기법이다. 그 중에서도 약 50~70 km 간격으로 분포된 다수의 기준국 정보를 활용하는 Network RTK 기법은 동적 사용자의 빠르고 정확한 위치 결정이 가능한 인프라로서 주목받고 있다. 하지만 스칼라 형태로 구성된 Network RTK 보정정보는 각 기준국 별로 관측된 위성 수에 따라 생성이 되기 때문에 보정 데이터 량이 상당히 방대하다. 메시지 전송에 필요한 데이터 량이 많을수록 고속의 통신 환경을 필요로 하며, 메시지 시간 지연이나 통신 단절에 매우 취약한 문제를 가지고 있다. 또한 스칼라 형태의 보정정보는 사용자와 기준국 간의 거리가 멀어질수록 보정 오차가 크게 발생하기 때문에 대륙 혹은 나라 규모의 광역에서 서비스하기 위해서는 수십~수백 개 이상의 기준국 인프라 구축이 필수적이다. 예를 들어, SBAS가 한반도 지역 서비스를 위해 5~7개의 기준국이 필요한 반면 Network RTK는 90~100개의 기준국이 필요하다. 즉 Network RTK는 시스템 구축 및 유지 비용이 SBAS 대비 약 15배 정도 많이 들게 된다.

본 논문에서는 기존 Network RTK의 문제점을 해결하기 위한 방법으로 대륙 급 광범위한 영역에서 실시간으로 cm급 초정밀 위치결정 서비스 제공이 가능한 Compact Wide-Area RTK 라는 새로운 개념의 광역보강항법 시스템 아키텍처를 제안하였다. Compact Wide-Area RTK는 약 200~1,000 km 간격으로 넓게 분포된 기준국 네트워크를 활용하여 반송파 위상 기반의 정밀한 위성 궤도 보정정보, 위성 Code/Phase 시계 보정정보, 대류

층 보정정보를 생성하는 시스템이다. 기존 스칼라 형태의 Network RTK 보정정보 대신 오차 요소 별 벡터 형태의 정밀 보정정보를 생성함으로써 데이터 량을 획기적으로 절감하고 서비스 영역을 확장할 수 있다. 최종적으로 SBAS와 마찬가지로 250 bps의 저속 통신 링크를 가진 정지궤도 위성을 통해 광역으로 보정정보 방송이 가능하다.

본 논문에서는 3가지 보정정보 중 위성 Code/Phase 시계 보정정보와 대류층 보정정보 생성을 위한 핵심 알고리즘에 대해 중점적으로 연구하였다. 반송파 위상 기반의 정밀 보정정보 생성을 위해서는 먼저 미지정수를 정확하게 결정해야 한다. 본 논문에서는 삼중 주파수 반송파 위상 측정치의 무-전리층 조합을 활용하여 전리층 보정정보 없이도 정확하게 미지정수 결정 가능한 새로운 방법을 제안하였다.

위성 Code/Phase 시계 보정정보는 통신 지연 및 고장 시 우수하고 강건한 성능을 위해 다중 기준국의 모든 측정치를 활용하여 추정된다. 이때 각 기준국 별 서로 다른 미지정수 때문에 발생하는 문제는 앞서 정확하게 결정된 기준국 간 이중차분 된 미지정수를 활용하여 수준을 조정하는 과정을 통해 해결이 가능하다. 그 결과 생성된 위성 Code/Phase 보정정보 메시지의 크기, 변화율, 잡음 수준이 크게 개선되었고, 통신 지연 시 오차 보상 성능이 기존 RTK 프로토콜 보다 99% 향상 됨을 확인하였다.

대류층 보정정보는 적은 수의 기준국 만을 활용하여 정확하게 대류층을 모델링하기 위해 자동 기상관측시스템으로부터 수집한 기상 정보를 추가로 활용하여 생성된다. 본 논문에서는 GNSS 기준국 네트워크로부터 정밀하게 추정된 반송파 위상 기반 수직 대류층 지연과 기상정보 기반으로 모델링 된 수직 대류층 지연을 함께 활용할 수 있는 새로운 알고리즘을 제안하였다. 구면조화함수를 사용하여 Network RTK 및 PPP-RTK 보다 필요한 메시지 양과 기준국 수를 크게 감소시키면서도 RMS 2 cm 수준으로 정확한 보정정보 생성이 가능함을 확인하였다.

본 논문에서 제안한 Compact Wide-Area RTK 시스템의 항법 성능을 검증하기 위해 미국 동부 지역 6개 기준국의 실측 GPS 데이터를 활용하여 테스트를 수행하였다. 그 결과 제안한 시스템은 미지정수 결정 이후 사용자의 95% 수평 위치 오차 1.9 cm, 95% 수직 위치 오차 7.0 cm 로 위치를 정확하게 결정하였다. 사용자 미지정수 결정 성능은 대류층 안정 상태에서 약 2분 내로 100% 의 성공률을 가진다. 본 논문에서 제안한 시스템이 향후 한국형 위성항법 시스템(KPS, Korean Positioning System)의 전국 단위 센티미터 급 서비스를 위한 알고리즘으로 활용되기를 기대한다.

주요어 : SBAS, compact RTK, network RTK, wide-area RTK, PPP-RTK, Carrier-phase based correction, centimeter-level positioning

학 번 : 2013-23056